Survival of the brightest: pIRIR dating of volcanic sediments in Sulawesi, Indonesia, using micro-aliquots of K-rich feldspar

Mariana Sontag-González[a,b*], Bo Li[b,c], Kieran O'Gorman[b], Basran Burhan[d], Budianto Hakim[e,f], Adam Brumm[d,g], Richard G. Roberts[b,c]

[a] *Institute of Geography, Justus Liebig University of Giessen, Giessen 35390, Germany*

[b] *Centre for Archaeological Science, School of Earth, Atmospheric and Life Sciences, University of Wollongong, Wollongong, NSW 2522, Australia*

[c] *Australian Research Council (ARC) Centre of Excellence for Australian Biodiversity and Heritage, University of Wollongong, Wollongong, NSW 2522, Australia*

[d] *Australian Research Centre for Human Evolution, Griffith University, Brisbane, QLD 4111, Australia*

[e] *Pusat Riset Arkeologi Prasejarah dan Sejarah (Badan Riset dan Inovasi Nasional [BRIN]), Makassar, Indonesia*

[f] *Pusat Kolaborasi Riset Arkeologi Sulawesi (BRIN), Jakarta, Indonesia*

[g] *School of Environment and Science, Griffith University, Brisbane, QLD 4111, Australia*

Abstract

Volcanic sediments are challenging to date with luminescence-based methods. Both main minerals used for dating—quartz and K-rich feldspar—commonly have suboptimal luminescence properties when of volcanic origins, primarily a low signal intensity and, for K-rich feldspars, high rates of anomalous fading. The present work provides a case study of the Leang Bulu Bettue (LBB) archaeological site in Indonesia, a key site in our understanding of the early human occupation of the island of Sulawesi, showing that currently available state-of-the-art methods can provide robust chronologies for volcanic sediments. Through various reliability tests, we establish the suitability of a post-IR IR stimulated luminescence (pIRIR) standardised growth curve (SGC) procedure for D_e estimation of 'micro-aliquots' containing 5–10 grains of K-rich feldspar and apply these methods together with dose rate estimates to determine 10 new reliable finite ages for the sedimentary deposits at LBB. Further, by applying the L_nT_n method to circumvent truncation of the D_e distribution caused by the non-linearity of the dose response curve in the higher dose range, we could extend the site's chronology to span ~20–210 ka. The new chronology is in keeping with previous radiocarbon and U-series ages for the site's upper layers. We show that the low fading rate of micro-aliquots relative to using large aliquots composed of hundreds of grains lies in a brightness-based selection. By targeting bright grains with low fading rates, the need for fading corrections is greatly reduced and they can be made with a smaller uncertainty

propagated through into the final age estimate, resulting in optical ages of improved accuracy and precision for volcanic sediments.

1   Introduction

Luminescence-based dating techniques have been commonly used to date the burial time of Quaternary sediments (e.g., Preusser et al., 2008). Mineral grains found in sediments in volcanic regions, however, usually possess different luminescence characteristics to those of plutonic minerals due to different crystallisation processes. The optically stimulated luminescence (OSL) signal from volcanic quartz is typically dim and sometimes lacks a fast-decaying signal (e.g., Bonde et al., 2001), while the light-sensitive red thermoluminescence (TL) emission is less easily bleached than the OSL signal, resulting in maximum ages for sediment deposition (Westaway and Roberts, 2006). Infrared stimulated luminescence (IRSL) from volcanic K-rich feldspar is also generally dim in addition to suffering from variable and commonly high rates of anomalous fading (Tsukamoto and Duller, 2008). Methods accessing IR-sensitive traps that fade much less, or not at all, have been developed, generally enabling the low- to non-fading signal components to be isolated from the composite IRSL signal. Post-infrared IRSL (pIRIR) measurement procedures, for example, utilise one or more low-temperature IR stimulations to preferentially deplete the fading components, so that subsequent IR stimulations at higher temperatures access traps that are less affected by fading (Thomsen et al., 2008; Buylaert et al., 2009; Li and Li, 2011; Thiel et al., 2011).

However, some samples emit pIRIR signals that fade at atypically high rates, such as those from the archaeological site of Leang Bulu Bettue (LBB) in southwest Sulawesi, Indonesia (Figure 1A). A wide range of g-values, 0–12% per 'decade' (a factor of 10 in time since irradiation), was reported for individual aliquots composed of hundreds of K-rich feldspar grains (dominated by sanidines) measured using a two-step pIRIR procedure consisting of an initial IR stimulation at 100°C followed by a high-temperature IR stimulation at 290°C, denoted as $pIR_{100}IR_{290}$ (Li et al., 2016b). To deal with this issue, an isochron method was proposed. Using the variation of fading rates observed for different aliquots, Li et al. (2016b) correlated the fading rates to the measured ages and extrapolated this relationship to a fading rate of 0 (i.e., non-fading). Although this procedure yielded ages in agreement with those obtained from independent dating methods, it is time-consuming to determine g-values for every dated aliquot and the resulting estimates have large uncertainties. Additionally, if the scatter in D_e values is not due solely to fading, but also to partial bleaching, post-depositional mixing or dose-rate heterogeneity, then the extrapolation can give rise to an inaccurate and/or imprecise estimate of sample D_e and, hence, age.

The highly variable fading rates observed by Li et al. (2016b) suggest that samples from this site would also benefit greatly from application of a single-grain dating approach to avoid 'signal

averaging' of low- and high-fading grains and, thus, yield more reliable age estimates. The use of a single-grain procedure also provides a means to examine D_e distributions for evidence of partial bleaching or post-depositional disturbance. On average, however, less than 10% of grains from LBB samples emit a pIRIR signal, making single-grain measurements time-consuming using the conventional single-aliquot regenerative-dose (SAR) procedure (Galbraith et al., 1999; Murray and Wintle, 2000). Standardised growth curves (SGCs) for K-rich feldspar allow measurement times to be reduced by up to 80%, thereby facilitating analyses at single-grain resolution for dim samples (Li et al., 2015, 2018). This approach is especially valuable for samples with high D_e values, such as those from LBB, as fewer high-dose measurement cycles are needed. Additionally, the use of 'micro-aliquots', in which 5–10 individual grains occupy each hole on a 100-hole disc, can be used to increase the yield of luminescent grains.

Here we (i) present a combined pIRIR and SGC procedure to obtain D_e values for sanidine grains from LBB in a time-efficient manner, using micro-aliquots to effectively retain single-grain resolution, and with only a small correction for fading; (ii) explore the differences between the results obtained using this procedure and that of Li et al. (2016b), to show that the observed reduced rate of fading is due to the selection of bright, low-fading grains; and (iii) present 14 new pIRIR ages for the upper layers of LBB as well as for deeper sedimentary deposits. The development of a protocol to reliably date the sediments at LBB will have important ramifications for our understanding of the occupation of Sulawesi by early hominins.

2 Study site and samples

The island of Sulawesi is geographically a key area for the study of hominin migration, being the largest island of Wallacea and inhabited by at least one unknown hominin species prior to 100 ka (van den Bergh et al., 2016). The Maros-Pangkep karst region in South Sulawesi contains dozens of archaeological sites, including some of the oldest known examples of modern human cave art in the world (Aubert et al., 2019; Brumm et al., 2021; Oktaviana et al., 2024).

The cave and rock-shelter site of LBB is situated in the karst region near the town of Maros in South Sulawesi, where a number of archaeological sites containing dated rock art have been reported (e.g., Bulbeck et al., 2004; Aubert et al., 2014; Brumm et al., 2017; Aubert et al., 2019; Brumm et al., 2021; Oktaviana et al., 2024). Excavated findings at LBB suggest insight into the symbolic material culture of early anatomically modern humans (AMH) in the form of personal ornaments (beads and pendants), ochre-stained tools and stone artefacts with linear incisions (Brumm et al., 2017). A small number of stone artefacts and other cultural remains in stratigraphically deeper layers also point to a previous occupation of the site by an unknown hominin group, as described in Burhan et al. (in preparation).

At the time of sample collection reported in this paper, the archaeological excavation at LBB consisted of a 6 m long trench along the rock-shelter wall and a 2 x 3 m trench extending towards the adjacent cave chamber (Figure 1A–C). Previous work on the site's chronology has described the sedimentary deposits associated with AMH presence spanning from ~40 ka to the Neolithic. In addition to the two luminescence dates obtained by isochron pIRIR, the chronology is supported by various techniques, including accelerator mass spectrometry (AMS) radiocarbon (^{14}C) dating of charcoal and freshwater gastropod (*Tylomelania perfecta*) shells, solution multi-collector inductively coupled plasma mass spectrometry (MC-ICP-MS) U-series dating of *in situ* speleothems, as well as laser ablation (LA) U-series dating of faunal remains. A summary is given in section S1 in the supplement; more detailed information on the dates and procedures can be found in Li et al. (2016b).

In this study, 14 samples were selected for dating using a pIRIR procedure, including the two samples from the previous luminescence dating study (LBB-I and -II; Li et al., 2016b) to directly compare the micro-aliquot SGC and the single-aliquot isochron pIRIR procedures.
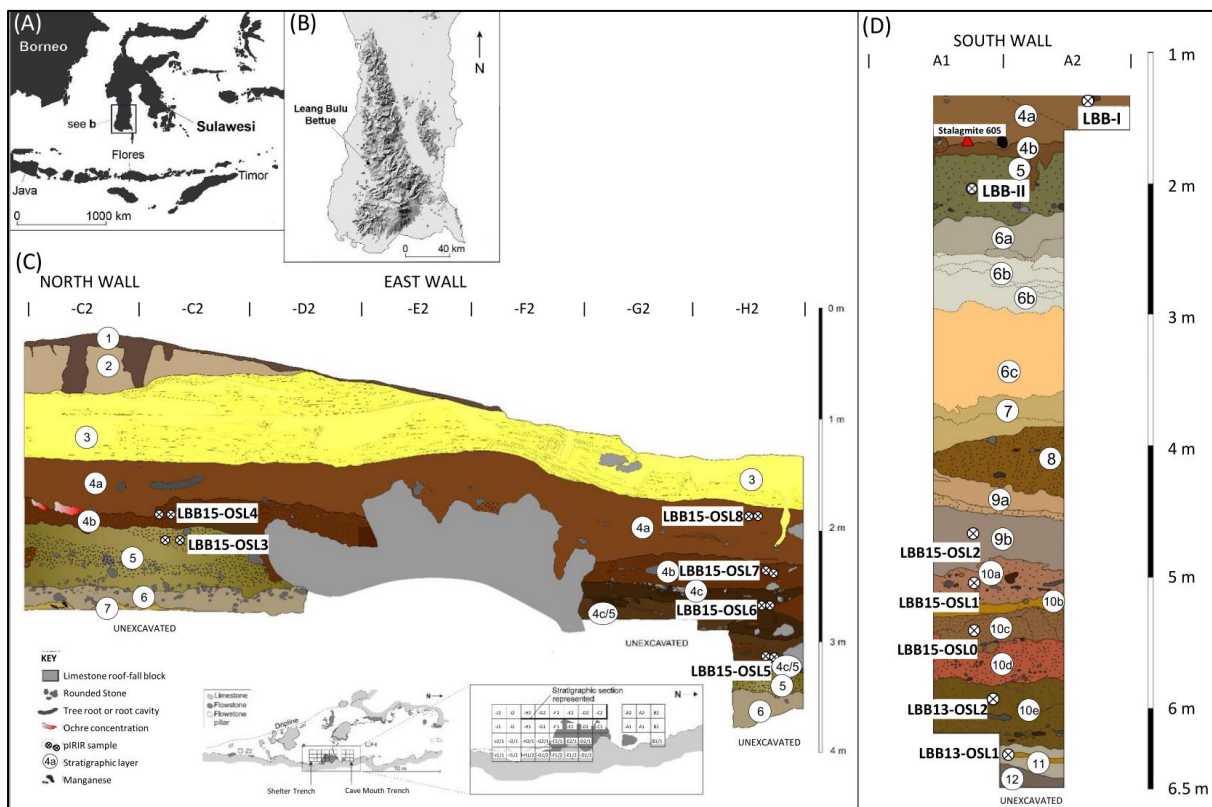

Figure 1: *Leang Bulu Bettue site details. (A) Location of Sulawesi in Indonesia. (B) Map of South Sulawesi. (C) Stratigraphy of top layers as exposed during the 2015 excavation season: sampling locations on the east walls of the excavation trenches are shown. (D) Stratigraphy of lower layers as exposed during the 2013 excavation season: sampling locations are projected onto the south wall of the excavation trench.*

3   Methods of equivalent dose determination

3.1   Sample collection and laboratory pretreatments

Samples were collected by hammering light-safe PVC tubes into profile walls of excavation trenches or by digging at night using subdued red-light torches and sealed into opaque black bags. The locations of the six samples from the east wall of the shelter trench (LBB15-OSL3 to -OSL8) are shown in Figure 1C. The locations of the seven samples from south wall of the cave mouth trench (LBB-I, LBB-II, LBB15-OSL0 to -OSL2, LBB13-OSL1 and LBB13-OSL2) are shown in Figure 1D. An additional sample (LBB18-OSL5) was taken in the north wall of the cave mouth trench from layer 2/3 (mixed in this location). In general, the samples from LBB are mostly clayey/silty, but many also contain larger-sized components, such as cobbles/pebbles (LBB15-OSL3 and -OSL6–8) and shells (LBB15-OSL7). When the sample tube of LBB13-OSL1 was opened in the laboratory, it was evident that it had cross-cut two layers (i.e., a sandy insert in layer 11, see Figure 1D), one light and the other dark in colour. Results will be shown for the combined sample, but possible mixing of differently old layers will be considered in section 7.

All samples were shipped to and later opened at the Luminescence Dating Laboratory at the University of Wollongong under subdued red light following standard procedures (Wintle, 1997). Samples were first wet-sieved to separate the 90–300 µm or 63–300 µm fraction, which was then treated with HCl acid (10%, overnight) to remove carbonates and a solution of H_2O_2 (10%, 24 h) to remove organic matter, and then wet-sieved again to obtain the desired grain-size fractions (90–125 µm, 90–180 µm or 180–212 µm in diameter). Grains were density separated using a solution of sodium polytungstate (2.58 g/cm^3) to isolate K-rich feldspars and the separated grains were etched in HF acid (10%, 10 min) to remove the alpha-irradiated outer layer while minimizing grain disintegration (Porat et al., 2015). Finally, the HF-etched grains were rinsed in 10% HCl acid to remove any precipitated fluorides, dried, and sieved again.

3.2   Analytical equipment and measurement procedure

All measurements were run on automated Risø TL/OSL-DA-20 readers (Bøtter-Jensen et al., 2003) equipped with IR light-emitting diodes (LEDs, 850 nm) and an IR laser (830 nm). IRSL was detected with a photomultiplier tube fitted with a blue filter pack (Schott BG-39 and BG-3), which allows the transmission of blue-violet emissions (~400 nm; e.g., Lomax et al., 2015). Discs were irradiated with $^{90}Sr/^{90}Y$ beta sources mounted on the readers and the received dose rates were calibrated for individual grain positions on a single-grain disc using gamma-ray-irradiated standard quartz provided by Risø. We

considered reader-specific counting statistics as sources of error and used an instrumental irreproducibility value specifically obtained for each reader, as described by Li et al. (2018). Grains used for dose recovery and residual dose tests were bleached in a Dr Hönle solar simulator (model: UVACUBE 400).

We loaded grains onto aluminium discs drilled with 100 holes, each 300 µm in depth and diameter. The instrumental setup and data-analysis procedure is identical to that typically used for single-grain measurements, but we refer to this as a 'micro-aliquot' approach since several grains— e.g., up to 10 grains of 90–125 µm diameter or five grains of 90–180 µm diameter—occupy each hole. While we cannot exclude that more than one grain is emitting signal when using grains of <180 µm diameter, a comparison with true single grains suggests that the total signal emitted from each hole is dominated by one grain (see section S3). Hence, we refer to this method as having 'single-grain' resolution. For clarity, however, we use the term 'micro-aliquot' to refer to the unit of measurement.

IRSL signals were measured using a two-step (100°C, 275°C) regenerative-dose pIRIR procedure, abbreviated as $pIR_{100}R_{275}$ (Thomsen et al., 2008; Blegen et al., 2015). Following a preheat at 320°C for 60 s, an initial IR step stimulated grains in all 100 holes simultaneously using IR LEDs for 200 s to deplete high-fading signal components. The second step used an IR laser to stimulate the grains in each hole individually for 1.5 s and generate the targeted signal used for dating. Each SAR cycle contained measurement of a test dose signal to correct for sensitivity changes, and a final IR stimulation at an elevated temperature (325°C) for 100 s to fully bleach the residual signals, before repeating the sequence using different sizes of regenerative dose (Table 1). Stimulation power was set at 90% for the LEDs and laser.

The natural- and regenerative-dose signals (L_n and L_x, respectively) and the corresponding test dose signals (T_n and Tx) were determined from the counts in the first 10 measurement channels (0.0– 0.1 s), with the counts in the last 10 channels (1.4–1.5 s) subtracted as background.

3.3   Luminescence measurement procedures

It has been suggested that a high initial IR temperature should be used to minimise fading of the signal measured subsequently in the two-step pIRIR procedure (Li and Li, 2012). Use of high temperatures in the first IR step, however, decreases signal brightness in the second step. For example, increasing the temperature of the first IR step from 50°C to 100°C or 150°C reduces the signal intensity by 30% and 60%, respectively (Figure 2), resulting in a significant decrease of the number of micro-aliquots with sufficient signal for D_e estimation. Consequently, we conducted the initial IR stimulation at 100°C. Using this $pIR_{100}IR_{275}$ procedure, the pIRIR signal decays rapidly, falling to one-third of the initial intensity over the course of the chosen integration period (0.0–0.1 s).

Table 1: pIRIR measurement procedures. Sequences are repeated for different regenerative doses (step 1). Single-aliquot measurements (pIR$_{100}$IR$_{290}$) were conducted to investigate luminescence properties; differences to the micro-aliquot procedure (pIR$_{100}$IR$_{275}$) are shown in bold type.

Step	Treatment (micro-aliquots)	Treatment (single aliquots)
1	Dose[a]	Dose
2	Preheat (320°C, 60 s)	Preheat (320°C, 60 s)
3	IR diodes stimulation (100°C, 200 s)	IR diodes stimulation (100°C, 200 s)
4	IR laser stimulation (275°C, 1.5 s)	IR **diodes** stimulation (**290°C, 200 s**)
5	Test dose (20 Gy)	Test dose (20 Gy)
6	Preheat (320°C, 60 s)	Preheat (320°C, 60 s)
7	IR diodes stimulation (100°C, 200 s)	IR diodes stimulation (100°C, 200 s)
8	IR laser stimulation (275°C, 1.5 s)	IR **diodes** stimulation (**290°C, 200 s**)
9	IR bleach (325°C, 100 s)	IR bleach (325°C, 100 s)

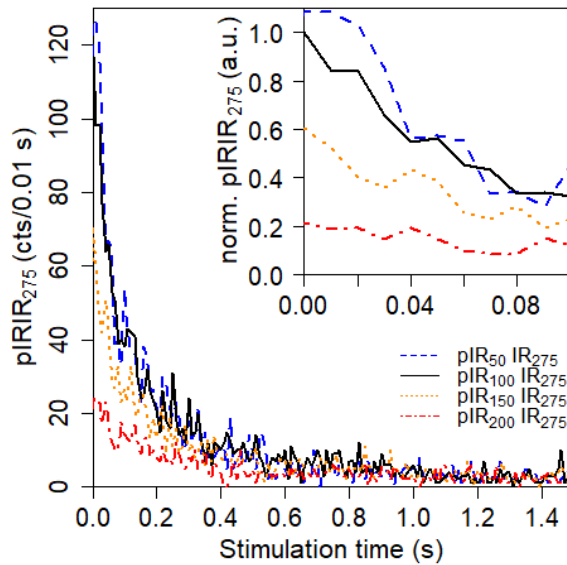[a] For natural samples, the given dose is 0 Gy.

Figure 2: Intensity of pIRIR$_{275}$ signals observed for a micro-aliquot sequentially stimulated at different initial temperatures (50°C, 100°C, 150°C or 200°C) after receiving doses of 50 Gy. Inset shows the period of signal integration, with signals normalised to the initial pIR$_{100}$IR$_{275}$ value.

Dose response curves (DRCs) were constructed using two approaches: Approach A (the conventional SAR procedure) used multiple (4–9) regenerative-dose cycles, including a zero-dose cycle and a repeat-dose cycle, whereas Approach B used only 2–4 regenerative-dose cycles, without zero- or repeat-dose cycles. The L_x and T_x data obtained from both approaches were used to construct the SGC,

following the protocol described by Sontag-González et al. (2021). After constructing the SGC, micro-aliquot D_e values were estimated using a third approach (Approach C) that requires, for each micro-aliquot, measurement of only the L_n, T_n, L_{R1} and T_{R1} signals, where the latter pair correspond to the L_x and T_x signals measured in the first regenerative-dose (R1) cycle.

To select only reliable micro-aliquots with reproducible luminescence characteristics, the following rejection criteria were applied: (1) Insufficient brightness: T_n <3σ of the background or relative standard error (rse) on T_n >25%; (2) High recuperation: ratio between L_x/T_x values measured in the zero- and highest regenerative-dose cycles is >5%; (3) Poor recycling: ratio between L_x/T_x values measured in the repeat-dose cycles lies outside the range 0.9–1.1; (4) Poor DRC: figure-of-merit value >10% or reduced-chi-square value >5 (Li et al., 2018); (5) Abnormal signal decay shape: a small proportion of micro-aliquots (<1%) exhibit abnormal decay shapes, such as the delayed onset of signal decay (Figure 3A,B). To identify these micro-aliquots, the ratio of T_n counts in the first half of the signal integration period (0.00–0.05 s) to the T_n counts in the second half (0.05–0.10) was calculated after subtracting the mean background count in the 1.4–1.5 s interval, and micro-aliquots with ratios <1 at 2σ were rejected (Figure 3C); (6) Imprecise L_x/T_x values: highest regenerative-dose has rse on L_x/T_x ratio >50%; (7) Negative L_n/T_n values: such values were rejected to enable logged age models to be applied. None of the dated samples had a significant proportion of negative values (at most 2.5% in LBB13-OSL1); these are expected to represent minor bioturbation events. This criterion was not applied in the residual-dose tests, so as not to reject micro-aliquots with L_n/T_n ratios consistent with zero.

Not all of these rejection criteria are applicable to all three approaches. For example, criterion 7 does not apply to the regenerative-dose measurements used for SGC construction, but criteria 1 and 5 were applied to the T_n data obtained in the natural-dose cycle of Approaches A and B. Criteria 1–6 were, therefore, used with Approach A, criteria 1 and 4–6 with Approach B, and criteria 1 and 5–7 with Approach C. Table S2 and Table S3 list the number of micro-aliquots rejected under each of these criteria for each of the samples.
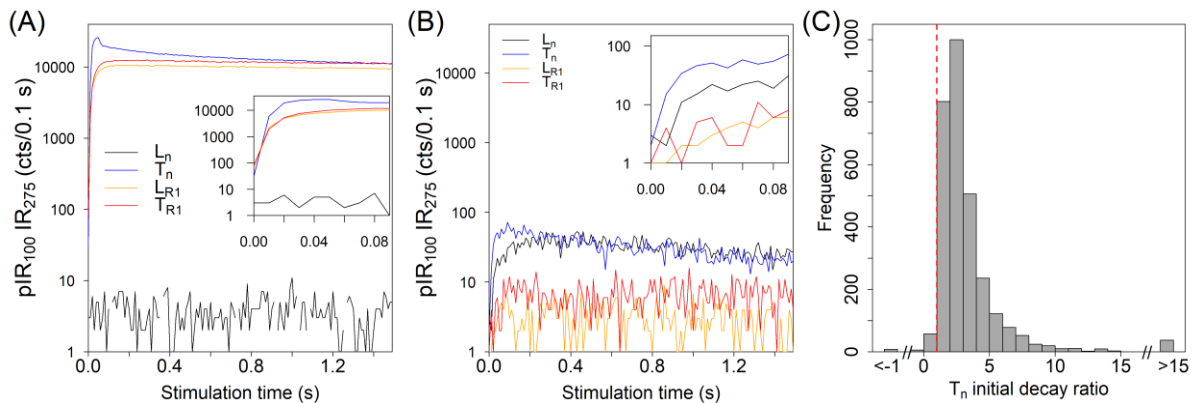

Figure 3: *(A, B) Examples of abnormal signal decay for one micro-aliquot each of samples (A) LBB15-OSL6 and (B) LBB15-OSL7. Insets show the signal integration intervals. (C) Histogram of ratios of*

background-corrected T_n counts for the 0–0.05 s interval divided by those in the 0.05–0.10 s interval for all micro-aliquots that passed the other rejection criteria; micro-aliquots of all samples used for D_e estimation are included. The red dashed line denotes a ratio of unity: micro-aliquots with ratios <1 (at 2σ) were rejected on the basis of abnormal signal decay.

3.4   SGC analysis

Data analysis was performed in an R programming environment (Peng et al., 2013; R Core Team, 2016; Peng and Li, 2018; Kreutzer et al., 2019). The SGC was built using the least-squares (LS) normalisation procedure of Li et al. (2016a) implemented in the lsNORM() function in the R package 'numOSL' using a Levenberg-Marquardt algorithm (More, 1978). This procedure was applied to SAR-derived L_x/T_x ratios measured over 2–9 regenerative-dose cycles. In an iterative process, the entire dataset is (i) fitted with a general-order kinetic (GOK) function of the type: $f(x) = a(1-(1 + bcx)^{(-1/c)}) + d$, where *a, b, c* and *d* are constants. In step (ii) the L_x/T_x ratios pertaining to individual grains are re-scaled with the purpose of minimising the sum of squared residuals between individual DRCs and the SGC of the whole dataset. The two steps are then repeated until the change in relative standard deviation is smaller than 10^{-6}. The final SGC is shown and examples of curve fit are shown in Figure S1. The lsNORM() function output includes the curve parameters, the different scaling factors for individual grains and the resulting LS-normalised L_n/T_n and L_x/T_x ratios (hereafter termed 're-normalised'). The reliability of the SGC is tested by checking the ratio between the measured L_x/T_x and the SGC, as well as comparing the D_e values obtained from full SAR and SGC analyses (section S2.2).

For D_e estimations, re-normalisation of the data occurred using only the first two measurement cycles (natural and a regenerative dose) by scaling the natural signal (L_n/T_n) and the regenerative signal (L_{R1}/T_{R1}), so that L_{R1}/T_{R1} lies on the SGC using the function scaleSGCN() of the 'numOSL' package. Outliers in the re-normalised (scaled) L_n/T_n or D_e distributions were rejected using the normalised median absolute deviation (nMAD) of $\log(L_n/T_n)$ or $\log(D_e)$, with 1.4826 as the correction factor for a normal distribution (Powell et al., 2002; Rousseeuw et al., 2006), using a cutoff value of 1.5 or 2.0 (i.e., any data point with a nMAD value larger than the cutoff is considered an outlier). The re-normalised L_n/T_n ratios or the D_e values were then analysed using either the CAM, 3-parameter-MAM or FMM (in the latter case without prior outlier rejection) (Galbraith et al., 1999; Roberts et al., 2000). Analysis of the re-normalised L_n/T_n values followed the L_nT_n method (Li et al., 2017; Jacobs et al., 2019; Li et al., 2020), which produces a single final estimate of L_n/T_n for each sample and determines the D_e value by projecting this estimate onto the SGC.

4   Luminescence properties

4.1   pIRIR signal intensity

Of the 50,700 micro-aliquots measured from the 15 samples using Approach C, 0.8–18.4% in each sample passed the rejection criteria (Table S3), resulting in a total of 2467 accepted data points for grain sizes of 90–125 µm or 90–180 µm. The $pIR_{100}IR_{275}$ signal following a 20 Gy test dose is similarly dim for all samples, with 68% of accepted micro-aliquots having T_n signals below 200 counts per 0.1 s (Figure S3A). Even for the brightest sample (LBB15-OSL6), 75% of the cumulative signal originates from just 3% of the micro-aliquots; for the dimmest sample (LBB13-OSL2), 75% of the signal is emitted by 0.1% of the micro-aliquots (Figure S3B).

4.2   Residual-dose tests

Residual doses were measured for the $pIR_{100}IR_{275}$ signals of six samples, following a laboratory bleach of either 4 h or 8 h, using the SGC procedure. The distribution of residual signals (re-normalised L_n/T_n ratios) among individual micro-aliquots is similar for these samples and also for the two bleach durations (Figure 4). Most samples display a broad distribution of residual signals, with overdispersion values of between 36 ± 9 % (LBB15-OSL1; 4 h bleach) and $71 \pm 9\%$ (LBB18-OSL5; 8 h bleach); the estimate of zero overdispersion for LBB15-OSL3 following an 8 h bleach is based on just three micro-aliquots. Weighted mean residual signals were calculated for each sample using the unlogged CAM (Arnold et al., 2009) to account for the small proportion (~5%) of micro-aliquots that yielded zero or 'negative' estimates of re-normalised residual L_n/T_n; the latter are consistent with zero at 2σ. The extent of bleaching varies for individual samples (Table S4). For example, the weighted mean residual dose of LBB15-OSL1 decreases by ~40% when the bleach length is increased from 4 h to 8 h, whereas the corresponding doses for LBB15-OSL6 are indistinguishable at 1σ. For all six LBB samples, an 8 h bleach resulted in weighted mean residual doses of <15 Gy, with LBB15-OSL6 bleached to a dose of just ~7 Gy within 4 h.
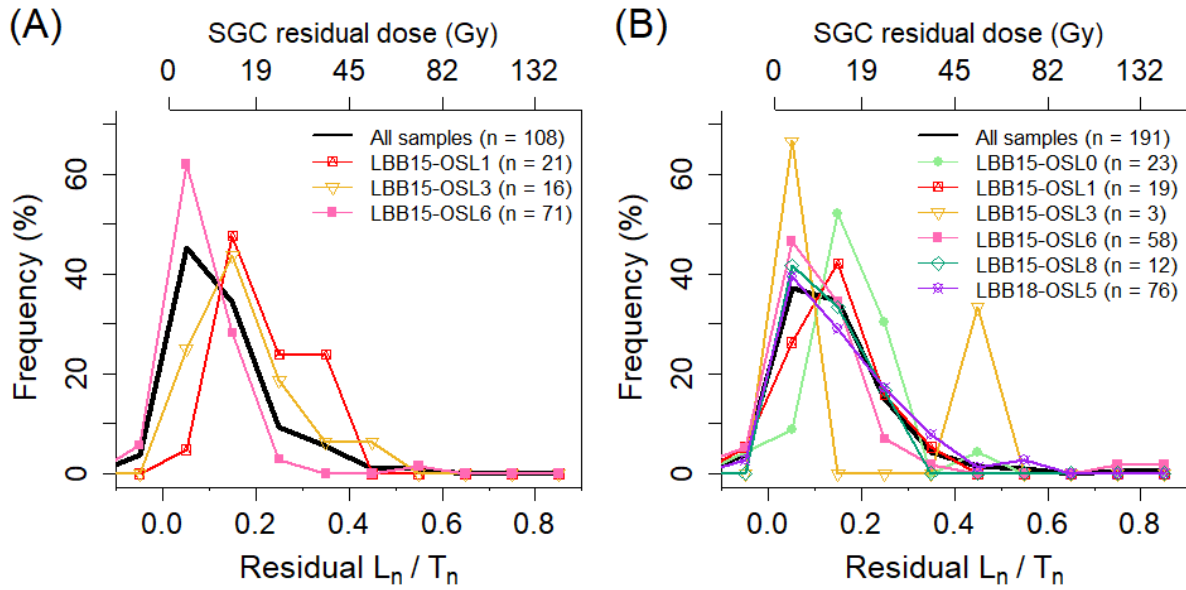
Figure 4: *Results of residual-dose tests. Frequency polygons (bin width: 0.1) of residual re-normalised L_n/T_n ratio (bottom x-axis) and corresponding residual dose (top x-axis) of micro-aliquots after (A) 4 h bleach of three samples, and (B) 8 h bleach of six samples. The number of accepted micro-aliquots of each sample (n) is given in the legend, and the combined results for all micro-aliquots in each panel are shown as thick black lines. Note that the SGC is not defined for residual doses <0 Gy. For clarity, three values with residual re-normalised L_n/T_n ratios less than –0.1 are omitted from panel (B).*

Any dependence of the size of the residual dose on the size of the sample D_e was also investigated. Figure 5 shows the residual re-normalised L_n/T_n ratios and corresponding residual doses for individual micro-aliquots of six samples following an 8 h bleach plotted as a function of the weighted mean sample D_e. The weighted mean residual doses range from 5.0 ± 1.7 to 17.7 ± 2.1 Gy, or 1.0–12.2% (~4% on average) of the weighted mean D_e values (Table S4). The sample with the lowest D_e, LBB15-OSL8 (CAM D_e of 86.6 ± 6.7 Gy), has a weighted mean residual dose of 10.6 ± 2.5 Gy, which is indistinguishable at 1σ from the residual dose of 10.0 ± 1.7 Gy for the sample with the highest D_e, LBB15-OSL1 (CAM D_e of 1007.2 ± 128.4 Gy). There is, therefore, no apparent correlation between residual dose and D_e, which suggests the presence of an unbleachable component, equivalent to a dose of ~10 Gy, common to all of the LBB samples.

To estimate a mean residual dose applicable to all samples from LBB, we calculated the weighted mean L_n/T_n ratio for all samples combined after an 8 h bleach (n = 191 micro-aliquots) and projected this ratio onto the SGC to estimate the corresponding residual dose (10.4 ± 0.7 Gy). This dose is within 1σ of the residual doses obtained for single aliquots of samples LBB-I and -II measured using a $pIR_{100}IR_{290}$ procedure: 11.5 ± 1.1 Gy and 12.6 ± 1.8 Gy, respectively (Li et al., 2016b). A residual dose of 10.4 Gy can represent up to ~12% of the weighted mean D_e of the youngest sample, so it should be subtracted from each of the sample D_e values for purposes of age determination.
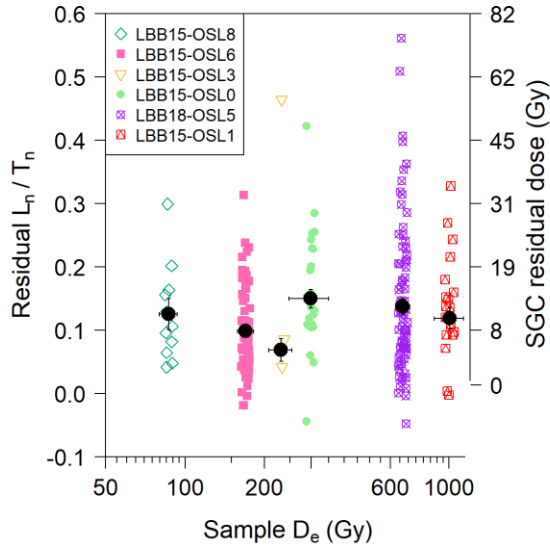
Figure 5: *Residual re-normalised L_n/T_n ratios (left-hand axis) and corresponding residual doses (right-hand axis) for 191 micro-aliquots of six samples measured after an 8 h bleach, plotted as a function of sample weighted mean (CAM) D_e. Black filled circles denote weighted mean residual re-normalised L_n/T_n ratios and residual doses. Note that the SGC is not defined for doses <0 Gy. For clarity, five values with residual re-normalised L_n/T_n ratios of 0.9 (160 Gy), 0.7 (107 Gy), -0.15, -0.38 and -0.47 are omitted from this plot.*

4.3   Signal recovery tests

Signal recovery tests based on the dose recovery test (Galbraith et al., 1999) were conducted on sample LBB15-OSL6. Following 8 h of laboratory bleaching to reduce this sample to a low residual dose, discs were given surrogate natural doses of 59, 230, 270, 545 or 813 Gy and then measured using $pIR_{100}IR_{275}$ and SGC procedures. Following the L_nT_n method, the conventionally used dose recovery ratio (i.e., measured dose divided by given dose) was replaced with a signal recovery ratio (e.g., a signal recovery ratio of unity is equivalent to a successful dose recovery). For each micro-aliquot, the signal recovery ratio was determined by dividing the ratio of the measured $L_{n'}$ and $T_{n'}$ signals (i.e., $L_{n'}/T_{n'}$, where the prime notation is used to distinguish them from the true L_n and T_n signals obtained from the natural samples) by the corresponding L_x/T_x ratio derived from the SGC at a dose equal to the sum of the given dose and the weighted mean residual dose for this sample and bleaching length (7.9 ± 0.9 Gy). The distributions of signal recovery ratios (Figure 6A) are similar at all given doses, and most of the ratios (66%) are consistent with unity at 2σ. The ratios also exhibit no systematic deviation with given dose (Figure 6B and Table S5). The weighted mean signal recovery ratio for all micro-aliquots combined (n = 416) is 0.97 ± 0.02, indicating the suitability of the $pIR_{100}IR_{275}$ and SGC procedures to recover doses up to at least ~800 Gy.
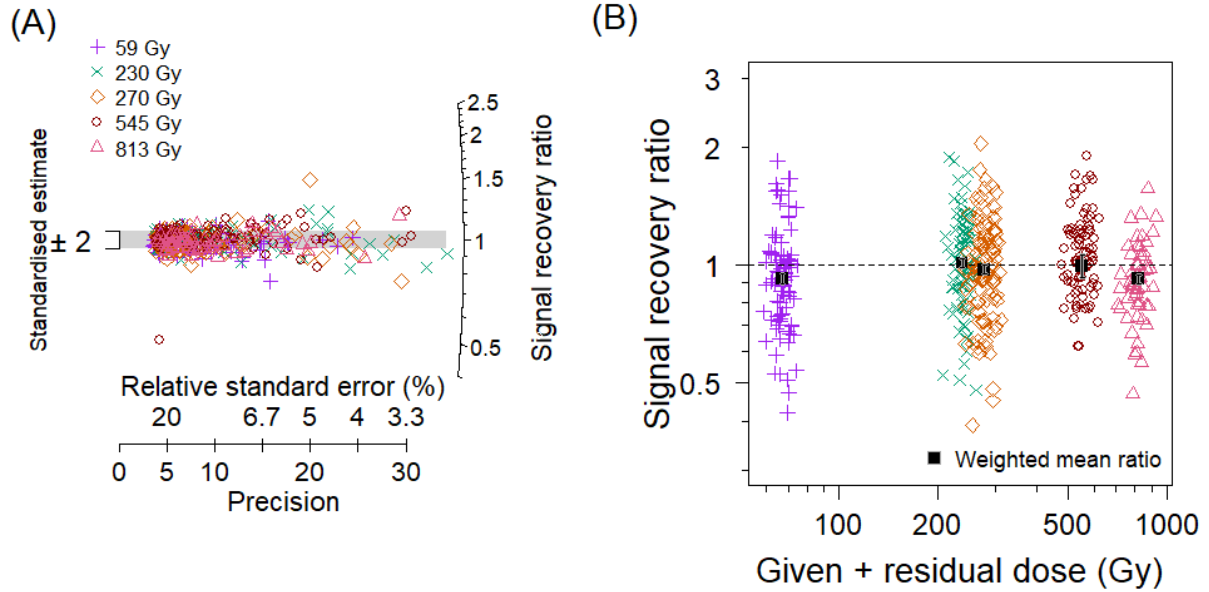
Figure 6: *Results of signal recovery tests. (A) Bleached micro-aliquots of sample LBB15-OSL6 were given surrogate natural doses of 59, 230, 270, 545 or 813 Gy and the dose recovery ratios calculated by dividing the measured $L_n/T_{n'}$ ratios by the corresponding L_x/T_x ratios derived from the SGC at the given dose (plus a residual dose of 7.9 Gy). (B) Same data as in panel (A) plotted as a function of the corresponding dose plus a residual dose of 7.9 Gy. One data point is omitted from this plot (dose recovery ratio <0.1 in the 545 Gy dataset). The weighted mean ratios were calculated using the CAM.*

4.4   Anomalous fading tests

The extent of anomalous fading was investigated using samples LBB15-OSL4 and -OSL6. The fading test consists of three measurement cycles in which identical doses of 50 Gy are given to micro-aliquots that had been measured previously. The first and third cycles are identical—both being prompt measurements of the $pIR_{100}IR_{275}$ signal after laboratory irradiation—and serve to test for sensitivity changes between measurement cycles. The second cycle includes a wait time of ~3 days between steps 2 and 3 in Table 1, during which period the micro-aliquots were stored in the dark at room temperature. This wait time corresponds to a delay of ~2.6 decades compared to the two prompt measurements. In addition to the rejection criteria used for Approach C, micro-aliquots were only accepted if the recycling ratio for the two prompt measurements was consistent with unity at 2σ. This resulted in the acceptance only of micro-aliquots that did not suffer from significant changes in sensitivity.

Figure 7A shows the distribution of fading ratios (i.e., ratio of the delayed signal to the first prompt signal) obtained for all accepted micro-aliquots of each sample. The weighted mean (CAM) ratios are 1.043 ± 0.045 (LBB15-OSL4) and 0.954 ± 0.016 (LBB15-OSL6), and the weighted mean ratio for all micro-aliquots of both samples combined is 0.965 ± 0.015. This corresponds to a *g*-value of 1.46 ± 0.61% per decade since time of irradiation t_c (normalised to a delay time of 2 days following

Huntley and Lamothe, 2001), calculated using the function of Kreutzer and Burow (2020). At 2σ, this *g*-value is not consistent with a fading rate of zero.

It has been suggested that, for K-rich feldspar, signal brightness is correlated to the extent of fading (Trauerstein et al., 2012; Brown et al., 2015; Guo et al., 2020), so we checked whether selecting only the brighter micro-aliquots influences the mean fading ratio. Figure 7B shows the results from micro-aliquots with $T_n > 100$ counts per 0.1 s, which includes about half of the micro-aliquots in Figure 7A. The weighted mean ratios are indistinguishable from those obtained for the complete dataset, which suggests that brightness is not correlated to fading rate, at least for these micro-aliquots.

The $pIR_{100}IR_{275}$ signal of these LBB samples appears, therefore, to fade only slightly: 0–3% at 2σ. But to avoid age underestimation, the measured ages of the LBB samples should be corrected for fading (using a *g*-value of 1.46 ± 0.61% per decade), with the uncertainty on the fading correction propagated through into the uncertainty on the final age estimate.
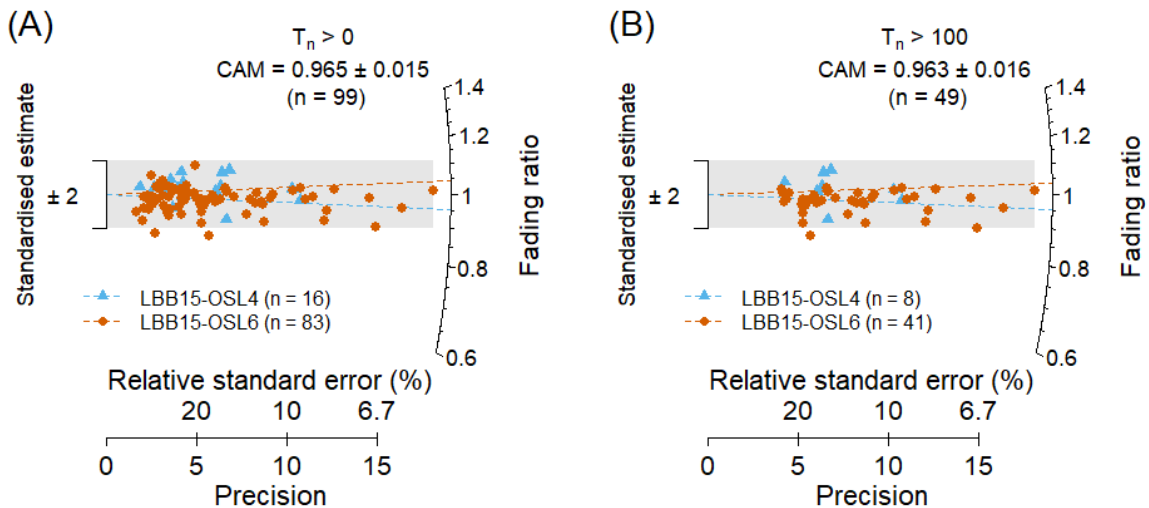

Figure 7: *Fading ratios for individual micro-aliquots of samples LBB15-OSL4 (blue) and LBB15-OSL6 (orange). Only micro-aliquots with T_n intensities (A) >0 counts/0.1 s or (B) >100 counts/0.1 s were accepted. The dashed lines represent the weighted mean (CAM) ratios for the accepted micro-aliquots of each sample, and the grey bands are centred on a ratio of unity; 95% and 94% of the data points are consistent with unity at 2σ in panels (A) and (B), respectively.*

4.5 Dependence of luminescence properties on signal brightness

The low mean fading rates of samples LBB15-OSL4 and -OSL6 (section 4.4) contrast with the variable, but mostly high (up to ~12% per decade), *g*-values observed for single aliquots of two other samples from LBB (Li et al., 2016b). The main difference between these studies is that the aliquots measured by Li et al. (2016b) were composed of hundreds of grains, delivering an average signal for all grains,

weighted by their relative brightness (i.e., individually, bright grains contribute more to the total signal than do dim grains). A similar pIRIR protocol was used in that study, but a higher second-step stimulation temperature was employed (290°C instead of 275°C) and the latter signals were stimulated using infrared LEDs instead of an IR laser. These non-identical measurement conditions could potentially account for some of the observed difference in fading rate between the micro-aliquot and single-aliquot measurements, but the much higher fading rates reported by Li et al. (2016b) may also or instead be related to the pIRIR contribution of dim grains in the single aliquots—grains that are too dim to pass the micro-aliquot T_n intensity rejection criterion (i.e., criterion 1 in section 3.3). To test this proposition, we measured 36 single-grain discs of sample LBB13-OSL2 using the 'micro-aliquot' procedure in Table 1, ensuring that each hole was occupied by only one grain (180–212 µm in diameter). Grains that passed or failed criterion 1 were then individually hand-picked from those discs and mounted on single-aliquot discs, creating two cohorts: aliquots composed of ~12 'bright' grains that passed criterion 1 (Cohort A, n = 3) and aliquots composed of ~550 'dim' grains that failed this criterion (Cohort B, n = 5) (Figure 8).
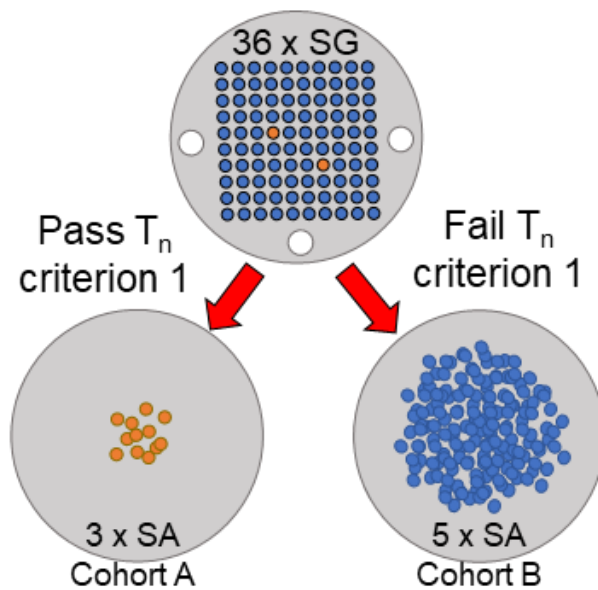

Figure 8: *Schematic of workflow: grains previously measured as single grains (SG) were separated into two cohorts according to their brightness (T_n intensity), comprising single aliquots (SA) of ~12 'bright' grains (Cohort A, n = 3) or ~550 'dim' grains (Cohort B, n = 5).*

Both cohorts were then measured using the single-aliquot procedure in Table 1. For both sets of grains, the $pIR_{100}IR_{290}$ decay curves are similar in shape (Figure 9A), decreasing to ~20% of initial L_x signal brightness (100 Gy given dose) within the first 10 s of illumination (Figure 9B). Based on the number of grains in each cohort and their corresponding L_x intensities, 60% of the signal emitted by a large single aliquot containing both dim and bright grains (e.g., Li et al., 2016b) would originate from

Cohort B. The luminescence behaviour of dim grains must, therefore, have contributed in large part to the single-aliquot pIRIR characteristics observed by Li et al. (2016b).

We then estimated the fading rates for the two cohorts of single aliquots using a SAR procedure (Auclair et al., 2003) that is similar to our micro-aliquot fading test, but with given doses of ~100 Gy and including five delay times per aliquot of up to 4 days in addition to the prompt measurements (Figure 9C). The *g*-values were calculated following Huntley and Lamothe (2001), with the prompt measurement time (t_c) normalised to 2 days. The weighted mean *g*-values of 2.8 ± 0.3% per decade (Cohort A) and 9.0 ± 0.9% per decade (Cohort B) are both within the range reported by Li et al. (2016b) for single aliquots of samples LBB-I and LBB-II (0–22% per decade). The *g*-value of the 'bright' aliquots (Cohort A) is also consistent at 2σ with the micro-aliquot fading rate of samples LBB15-OSL4 and -OSL6 (1.46 ± 0.61% per decade). Comparison of the ranges of *g*-values obtained for individual aliquots of Cohort A (0.4 ± 1.6% to 2.8 ± 2.9%) and Cohort B (0.8 ± 1.9% to 10.3 ± 3.7%) indicates that not all dim grains have high fading rates, but that all high-fading grains are dim. This finding supports the selection of bright grains and rejection of dim grains for D_e and age determination.

Since thermal stability can also give rise to differences in D_e, we also examined the thermal stability of Cohorts A and B by applying a pulse-anneal test to one aliquot of each cohort. The test consisted of repeatedly measuring the L_x and T_x signals from a regenerative dose of 50 Gy, after a cut-heat anneal (inserted between steps 1 and 2 of the single-aliquot procedure in Table 1) at 20°C increments between 320°C and 500°C (heating rate of 5°C/s). L_x and T_x values were calculated from the counts in the first 10 s of stimulation, with the counts in the last 10 s subtracted as background. For both aliquots, a 320°C cut-heat was repeated in a final measurement cycle; the resulting L_x/T_x ratios are consistent (at 1σ) with those obtained in the initial 320°C cut-heat cycle. The pulse-anneal curve shapes are similar for both aliquots, remaining stable to ~360°C and then decaying to ~15% of initial L_x/T_x intensity after heating to 500°C (Figure 9D), indicating that the pIRIR signals for both the dim and bright grains are thermally stable, and equally so.
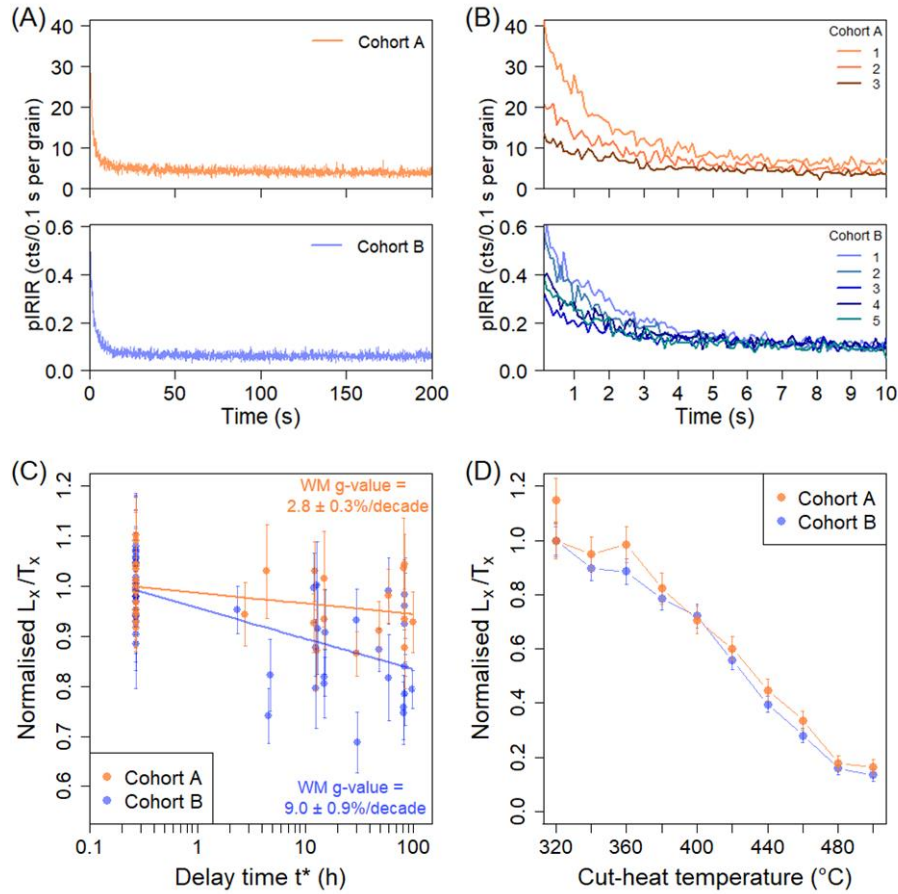
Figure 9: Comparison of $pIR_{100}IR_{290}$ signal decay curves, fading rates and thermal stabilities for bright (orange) and dim (blue) grains. (A) Representative examples of L_x signal decay for Cohort A and B aliquots. (B) Signal integration period (0–10 s) of L_x signal decay for all aliquots of Cohort A and B. In panels (A) and (B), signals are normalised by dividing the number of counts by the number of grains on each aliquot. (C) Fading test results for all aliquots of Cohorts A and B. L_x/T_x ratios are normalised by the average prompt L_x/T_x of each aliquot and plotted as a function of delay time (t^*). The linear fits made to the normalised L_x/T_x ratios as a function of $log(t^*)$ for Cohorts A and B serve only to demonstrate the general trend; their weighted mean (WM) g-values were calculated from the g-values for individual aliquots. (D) Pulse-anneal curves for Cohorts A and B (one aliquot of each), with L_x/T_x ratios normalised to the initial L_x/T_x intensity.

5   Dose rate determination

5.1   External dose rate

Beta dose rates were determined directly from dried and powdered subsamples measured on a Risø GM-25-5 multicounter system. Gamma dose rates were measured directly by *in situ* gamma spectrometry with a NaI(Tl) detector (2-inch in diameter). We were not able to determine the gamma

17

dose rate *in situ* for the 4 samples collected in 2013 (LBB-I, LBB-II, LBB13-OSL2 and LBB13-OSL1) as these were collected by the excavation team. The gamma dose rates of these samples were estimated by determining radionuclide concentrations of bulk material collected in dosimetry bags at every sampling location (dried and powdered) using thick-source alpha-counting for concentrations of U and Th and beta-counting for K concentrations. Cosmic ray dose rates were estimated following Prescott and Hutton (1994). Dose rate and sampling information is summarised in Table 2.

The external dose rates of four samples differ from the others in their relationship between gamma and beta dose rates (Figure 10). Samples LBB15-OSL0, LBB13-OSL1 and LBB18-OSL5 have relatively high external beta dose rates in comparison to their gamma dose rates. In contrast, sample LBB15-OSL1 has a very low beta dose rate of 1.21 ± 0.06 Gy/ka, which stands out in comparison to the others (1.81 ± 0.09 to 2.77 ± 0.21 Gy/ka).

It is interesting to compare the radionuclide concentrations of samples LBB13-OSL1, which has a high beta-to-gamma dose rate ratio, and LBB-I. Both samples have similar total dose rates (5.60 ± 0.22 and 5.81 ± 0.27, respectively). However, the bulk concentrations of U and Th of LBB13-OSL1 are roughly half those of LBB-I. The total dose rate is balanced by the K concentration, which is twice as high for LBB13-OSL1 as for LBB-I. The amount of potassium in soil can be related to the presence of clays (e.g., Barré et al., 2007; Raheb and Heidari, 2012) and can be expected to differ between stratigraphic layers.

It is possible that these samples represent the natural spread in environmental dose rates, given the overall heterogeneity of the sedimentary sequence, with the presence of cobbles, shells, calcite layers, etc. Indeed, the range of total dose rates for this site is relatively large, with values of 3.87–5.81 Gy/ka obtained for the same stratigraphic layer 4 (though we note that it is composed of sublayers). However, we also cannot rule out that some of these samples suffer from radionuclide disequilibrium. Overall, care should be taken when using the total dose rates for age estimation of the four samples with outlying beta-to-gamma-ratios, as (i) the estimated beta dose rates might represent a 'local' phenomenon and not that to which most of the grains in the ~20 cm-long OSL tube were exposed to, or, even, (ii) that the measured dose rates might not have prevailed throughout the burial time (in the case of disequilibrium).
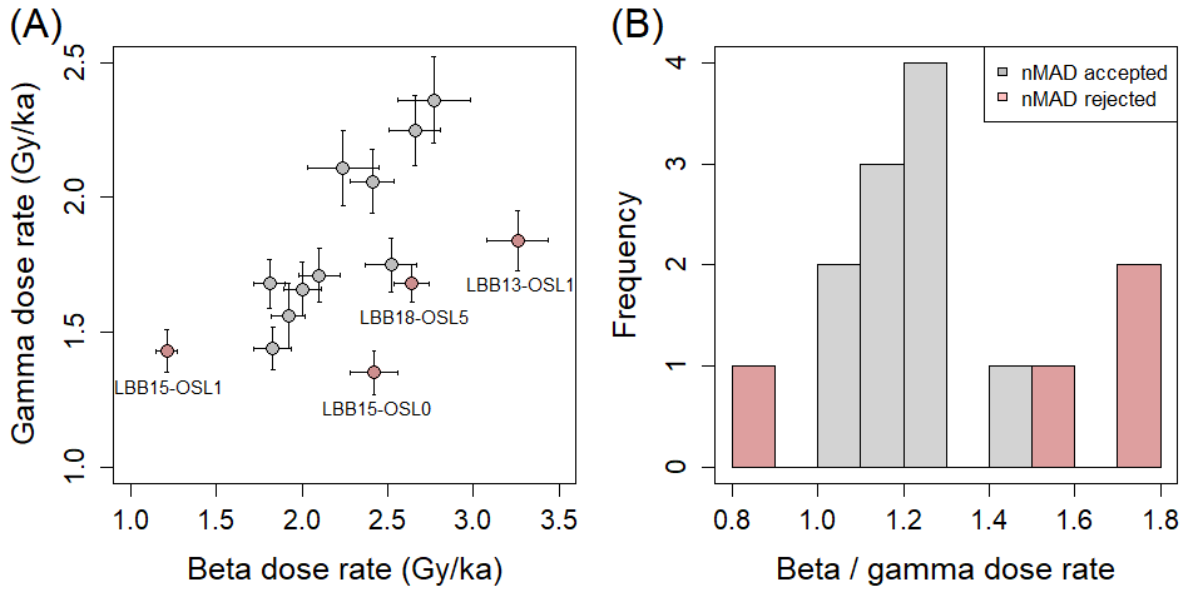
Figure 10: *(A) External beta and gamma dose rates of the 14 LBB samples. (B) Histogram of the ratio of the dose rates shown in panel (A). nMAD outliers (cutoff = 2.0) are shown as light red symbols (A, B) and labelled by sample code (A).*

5.2   Internal dose rate

Single grains of 180–212 μm from two samples (LBB15-OSL5 and -OSL6) were analysed to determine the internal K-concentrations to calculate internal dose rates. After $pIR_{100}IR_{275}$ measurements (Approach C), grains that passed the rejection criteria were hand-picked and mounted in resin, resulting in 30 grains from sample LBB15-OSL5 (out of 600 measured grains) and 55 grains from LBB15-OSL6 (out of 1500 measured grains). K-concentrations of feldspar phases were determined using the QEM-EDS calibration of O'Gorman et al. (2021). The uncertainty associated with the QEM-EDS calibration is ~0.2 wt% at 2σ.

Analysis of the QEM-EDS maps of 84 of the 85 grains identified 98.5% of grain areas as feldspar, primarily sanidine, confirming the XRD results obtained by Li et al. (2016b). About 0.1% of grain areas were quartz inclusions and 1.4% remained unclassified but are probably at least partially clay minerals. One grain had ~87.7% quartz, ~12.2% unclassified and a small (~0.1%) feldspar inclusion, with a K-concentration of ~0.5 wt%. The feldspar-dominated grains had K-concentrations in the range 8.3–13.6 wt% (at 2σ). Additionally, the grains' K-concentration does not appear to contribute to the variability of signal brightness (Figure 11). Taking the arithmetic mean K-concentration of grains (n = 85) and their standard deviation results in a mean K-concentration of 11.5 ± 1.7 wt%. A total of 99% of measured grains (all except for the quartz-rich grain) are consistent with this value at 2σ. We have shown that, after accounting for grain-size dependent dose rates, the D_e distributions of the larger

grains of these two samples coincide with those of the 90–125 µm populations (see section S3), so we used the QEM-EDS-derived K-concentration to calculate internal beta dose rates for micro-aliquots of all samples used in this study. We also accounted for an assumed rubidium (Rb) concentration of 400 $\pm$ 100 ppm (Huntley and Hancock, 2001), resulting in internal beta dose rates of 0.45 $\pm$ 0.06 Gy/ka (grains 90–125 µm in diameter), 0.55 $\pm$ 0.07 Gy/ka (90–180 µm) or 0.78 $\pm$ 0.10 Gy/ka (180–212 µm). As grains areas are 97.2% feldspar, we assume the internal alpha dose rate to be zero.
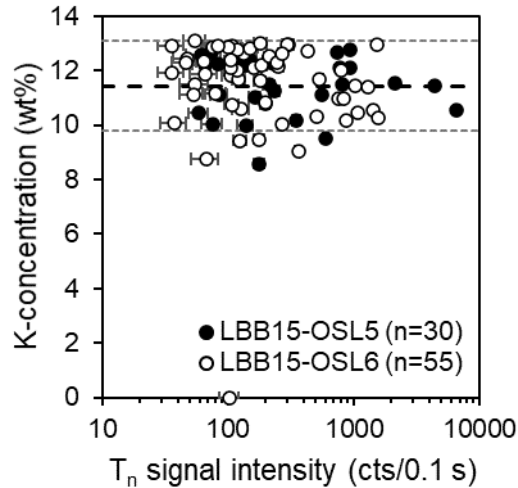

Figure 11: *QEM-EDS-derived K-concentrations of single luminescent grains from the <2.58 g/cm^3 density fractions of two samples plotted against their T_n signal intensities. The dashed lines represent the arithmetic mean K-concentration (large dashed line) and the standard deviation (at 1σ) around it (small dashed lines).*

Table 2: *Sampling and D$_e$ estimation details. Burial depths (i.e., depths below current surface) and stratigraphic layers, grain sizes, proportion of water per dry sample mass used for age calculation and field water contents in parentheses as well as dosimetry components are provided for each sample. Bulk radionuclide concentrations were determined through thick-source alpha counting coupled with beta-counting. The total dose rate ($\dot{D}_{total}$) is the sum of gamma ($\dot{D}_\gamma$), external beta ($\dot{D}_{\beta\ external}$), internal beta ($\dot{D}_{\beta\ internal}$) and cosmic ($\dot{D}_{cosmic}$) dose rates.*

Sample code	Layer	Burial depth (cm)	Grain size (µm)	Water (%)	Dose rate ($\dot{D}$) (Gy/ka)				
					$\dot{D}_\gamma$	$\dot{D}_{\beta\ external}$	$\dot{D}_{\beta\ internal}$	$\dot{D}_{cosmic}$	$\dot{D}_{total}$
LBB18-OSL5	2–3	30	90–125	16 (16)	1.68 ± 0.07 [a]	2.64 ± 0.10	0.45 ± 0.06	0.16 ± 0.02	4.93 ± 0.14
LBB15-OSL8	4a	52	90–125	23 (17)	1.75 ± 0.10 [a]	2.52 ± 0.15	0.45 ± 0.06	0.16 ± 0.02	4.87 ± 0.19
LBB-I	4a	160	90–180	23 (29)	2.36 ± 0.16 [b]	2.77 ± 0.21	0.55 ± 0.07	0.14 ± 0.02	5.81 ± 0.27
LBB15-OSL4	4b	180	90–125	25 (27)	2.25 ± 0.13 [a]	2.66 ± 0.15	0.45 ± 0.06	0.14 ± 0.02	5.50 ± 0.20
LBB15-OSL7	4b	103	90–125	25 (22)	1.71 ± 0.10 [a]	2.10 ± 0.12	0.45 ± 0.06	0.15 ± 0.02	4.40 ± 0.17
LBB15-OSL6	4c	134	90–125	20 (20)	1.44 ± 0.08 [a]	1.83 ± 0.11	0.45 ± 0.06	0.15 ± 0.02	3.87 ± 0.15
LBB15-OSL5	4c/5	182	90–125	24 (23)	1.66 ± 0.10 [a]	2.00 ± 0.11	0.45 ± 0.06	0.14 ± 0.02	4.25 ± 0.16
LBB-II	5	197	90–180	28 (30)	2.11 ± 0.14 [c]	2.24 ± 0.21	0.55 ± 0.07	0.13 ± 0.01	5.04 ± 0.26
LBB15-OSL3	5	210	90–125	28 (25)	2.06 ± 0.12 [a]	2.41 ± 0.13	0.45 ± 0.06	0.13 ± 0.01	5.04 ± 0.19
LBB15-OSL2	9b	460	90–125	39 (39)	1.68 ± 0.09 [a]	1.81 ± 0.09	0.45 ± 0.06	0.10 ± 0.01	4.03 ± 0.14
LBB15-OSL1	10a	500	90–125	42 (42)	1.43 ± 0.08 [a]	1.21 ± 0.06	0.45 ± 0.06	0.09 ± 0.01	3.18 ± 0.11
LBB15-OSL0	10c	540	90–125	25 (25)	1.35 ± 0.08 [a]	2.42 ± 0.14	0.45 ± 0.06	0.10 ± 0.01	4.31 ± 0.17
LBB13-OSL2	10e	594	180–212	34 (34)	1.56 ± 0.12 [d]	1.92 ± 0.10	0.78 ± 0.10	0.09 ± 0.01	4.35 ± 0.19
LBB13-OSL1	11	641	90–125	26 (26)	1.84 ± 0.11 [e]	3.26 ± 0.18	0.45 ± 0.06	0.09 ± 0.01	5.60 ± 0.22

[a] Gamma dose rate determined by *in situ* gamma spectrometry

[b] Gamma dose rate determined from bulk radionuclide concentrations (2.2 ± 0.2% K; 12.3 ± 0.4 ppm U; 25.2 ± 2.6 ppm Th).

[c] Gamma dose rate determined from bulk radionuclide concentrations (1.4 ± 0.2% K; 12.7 ± 0.4 ppm U; 21.9 ± 2.4 ppm Th).

[d] Gamma dose rate determined from bulk radionuclide concentrations (2.3 ± 0.2% K; 9.2 ± 0.3 ppm U; 11.6 ± 1.7 ppm Th).

[e] Gamma dose rate determined from bulk radionuclide concentrations (4.3 ± 0.1% K; 6.3 ± 0.2 ppm U; 12.5 ± 1.6 ppm Th).

6   pIRIR D_e

We used the SGC developed for LBB to obtain re-normalised L_n/T_n distributions for 14 samples, as shown in Figure S6 in stratigraphic order (left-hand column). For comparison, the D_e distributions resulting from projecting the individual micro-aliquot re-normalised L_n/T_n values onto the SGC are shown in the right-hand column for each sample. Note that for all samples, it was not possible to calculate micro-aliquot D_e estimates for all L_n/T_n values: 2–24% of these samples' re-normalised L_n/T_n values were outside the defined range of our SGC. The SGC is not defined below 0 Gy (equivalent to an L_n/T_n of 0.013), which caused 4 micro-aliquots to be rejected (two micro-aliquots of LBB-I and one each of LBB18-OSL5 and LBB15-OSL8); they were consistent with 0 Gy at 1σ. Additionally, the SGC's high-dose limit is 2500 Gy (equivalent to an L_n/T_n of 2.363), as no regenerative doses were measured above this value (see Figure S1), which caused 162 micro-aliquots (9%) to be rejected (because their L_n/T_n is consistent with or higher than that of the highest dose used to build the SGC).

We found that the re-normalised L_n/T_n distributions of most samples had relatively high overdispersion values (27–73%). The overdispersion values remained relatively high for six of these samples (36–44%) even after outlier rejection with a nMAD cutoff of 2.0. Of these, five samples pertain to layer 4 and one sample to layer 5. A similar pattern was observed for the D_e distributions, with overdispersion values before and after outlier rejection ranging 68–131% and 34–75%, respectively (note that for the D_e distributions we used a cutoff value of 1.5, see section 6.1). For comparison, the D_e overdispersion value of the only tightly-distributed sample (LBB15-OSL8; Figure S6D) from this layer was 34 ± 4% after outlier rejection. Among other possibilities, such as beta dose rate heterogeneity, overdispersion values in D_e higher than the 20%–30% commonly observed for well-bleached samples (Arnold and Roberts, 2009) can be indicative of either incomplete bleaching prior to deposition or considerable post-depositional mixture. Indeed, there is evidence that layer 4 was subjected to reworking events (see section S1). For this reason, we also consider the minimum age model (MAM) analysis for D_e estimation of several samples. However, first, we must consider which distributions should be modelled, the L_n/T_n or the D_e distributions.

6.1   Use of the L_nT_n method for D_e determination

The establishment of the SGC also allows for the recent L_nT_n method to be applied (Li et al., 2017; Jacobs et al., 2019; Li et al., 2020), which circumvents the issue of truncation of D_e values caused by the non-linearity of the DRC in the higher dose range by modelling the central tendency of the re-normalised L_n/T_n distribution rather than the D_e distribution. This advantage is exemplified for the CAM before and after outlier rejection in Figure S7A and B, respectively, for the 14 samples from LBB, where the D_e distributions were obtained by projection of the individual re-normalised L_n/T_n values onto the SGC. The number of accepted micro-aliquots for each sample before and after outlier removal

is given in Table S6. CAM D_e values obtained using the L_nT_n method are 89−154% of those obtained when modelling the D_e distribution; the higher deviation is observed in the higher-dose range, where the SGC's non-linearity is more pronounced (Figure S7A). After outlier rejection, the nMAD CAM D_e values are on average slightly smaller than those derived from the L_nT_n method (Figure S7B), but the choice of cutoff value of the nMAD SGC D_e distributions (1.5, 2.0 or 2.5) has no systematic effect on the resulting nMAD CAM D_e, as with increasing data points identified as outliers, the D_e can be higher or lower depending on the distribution. In general, the SGC D_e distributions are more spread than the corresponding L_n/T_n distributions, so a lower cutoff value is needed for the former to remove the same proportion of outliers.

Similar calculations are shown in Figure 12 using the MAM. Rejection of outliers is also important for this age model, particularly low-dose outliers, as these have a large effect on the modelled value. For this reason, only the data points that pass an nMAD outlier rejection were modelled ('nMAD MAM') for the 14 samples from LBB. Cutoff values of 2.0 and 1.5 were used to identify outliers in the re-normalised L_n/T_n and SGC D_e distributions, respectively, to account for their differing natural spread. In the case of the nMAD MAM, an additional parameter complicates the comparison between D_e estimation methods. The sigma-b (σ_b) parameter, which represents the scatter of a well-bleached grain population, appears to show a dose-dependency for L_n/T_n distributions, as evidenced by comparing overdispersion values from signal recovery tests with given doses ranging 59–813 Gy (section 4.3). The overdispersion of the re-normalised $L_{n'}/T_{n'}$ ratios obtained in the signal recovery tests ranged $14 \pm 2\%$ to $19 \pm 2\%$ after outlier rejection, with lower overdispersion observed at higher given doses (Figure 13). In contrast, modelling the minimum age of D_e values is usually achieved with a constant σ_b value. Figure 12 displays the resulting D_e values using three values for σ_b (0.15, 0.25 and 0.35) when modelling the re-normalised L_n/T_n distributions. A constant value of 0.35 was used for the SGC D_e distributions, according to the overdispersion of sample LBB15-OSL8 (Figure S6D), assumed to be well-bleached because of its tight distribution. Depending on the choice of σ_b, matching MAM D_e values can be obtained with the two methods. At the lower dose range (<200 Gy), modelling the re-normalised L_n/T_n distributions with a σ_b of 0.25 yields D_e values in agreement with those obtained from the MAM SGC D_e; at higher doses, a lower σ_b of 0.15 is needed to obtain matching D_e values. This trend follows that observed for the signal recovery tests of lower overdispersion of re-normalised L_n/T_n distributions at the higher dose range. In contrast to the CAM, the two methods yield matching D_e values with the MAM even at relatively high dose ranges (300−1000 Gy) because only the lower dose data points are targeted, for which the SGC truncation is less pronounced.

MAM results are given for each sample in Table S7. For comparison, analyses of the datasets before outlier rejection are also given. Statistical parameters describing the fit of the MAM analyses are given in Figure S8. For comparison, analyses using σ_b values spanning 0.1−0.4 were included. Overall, the maximum log likelihoods resulting from application of the MAM to the SGC D_e distributions after

outlier rejection are less dependent on σ_b than those resulting from the re-normalised L_n/T_n distributions (Figure S8A–B). The distribution of the proportion of micro-aliquots considered to be fully bleached (p-value) as a function of σ_b has an offset of ~0.15 between the two methods (Figure S8C–D). This finding is in agreement with the expectation that higher σ_b values are needed to account for the higher spread of the SGC D_e distributions compared with the re-normalised L_n/T_n distributions.
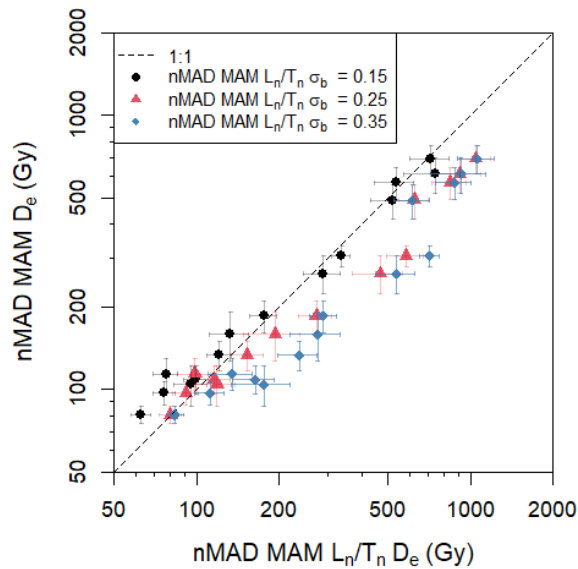

Figure 12: *Comparison of MAM D_e values after outlier removal obtained from each sample using either the L_nT_n method (x-axis), where the re-normalised L_n/T_n distribution is modelled, or the more conventional D_e method (y-axis), where the distribution of SGC D_e values is modelled; this distribution is obtained by projecting the individual re-normalised L_n/T_n value of each micro-aliquot onto the SGC. Results are shown using three values for σ_b, the expected overdispersion of a well-bleached population, for the nMAD MAM of the re-normalised L_n/T_n distributions (a constant value of 0.35 was used for the SGC D_e distributions). nMAD cutoff values of 2.0 and 1.5 were used for the re-normalised L_n/T_n and SGC D_e distributions, respectively.*
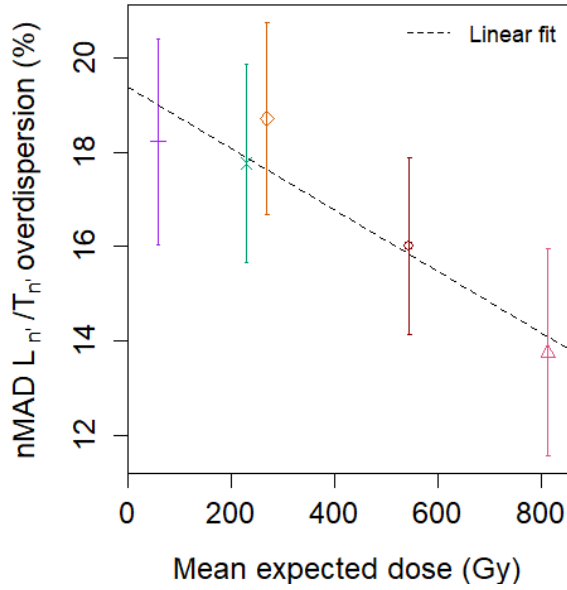
Figure 13: *Overdispersion of the re-normalised $L_{n'}/T_{n'}$ ratios from signal recovery tests on sample LBB15-OSL6 given on average 59, 230, 270, 545 or 813 Gy, using the same groups as in Figure 6. Error bars represent standard errors at 1σ.*

6.2 Obtaining D_e values for LBB

Figure 14 shows example datasets used to obtain the final D_e estimates using either the nMAD CAM or the nMAD MAM of four samples. The final distributions used for dating of all samples are shown in Figure S9. We dated the nine upper samples by modelling the SGC D_e populations (Figure S9A–I; two examples shown in Figure 14A–B), as these samples are in the lower dose range of the SGC and do not suffer significantly from the issues associated with truncation. Two of these samples, (LBB15-OSL8 and LBB15-OSL5; Figure 14B and Figure S9G, respectively) had D_e distributions with a dominant central component, so we expect the nMAD CAM (nMAD cutoff = 1.5) to yield reliable final D_e estimates for these samples. The other seven samples (LBB18-OSL5, LBB-I, LBB15-OSL4, -OSL7, OSL6, LBB-II and LBB15-OSL3; Figure 14A, Figure S9C–F, H, I, respectively) had broad D_e distributions with a more pronounced lower-dose component. So, we assume these samples were not well-bleached prior to burial or are composed of partially mixed samples and used the nMAD MAM (nMAD cutoff = 1.5) to obtain D_e estimates for the lower-dose component, which is assumed to have been well-bleached prior to burial. In the case of the MAM, we used a σ_b value of 0.35, according to the overdispersion of the tightly-distributed sample LBB15-OSL8 (Figure 14B).

For the lower five samples (Figure S9J–N; two examples shown in Figure 14C–D), we modelled the re-normalised L_n/T_n ratios (L_nT_n method) and projected only the one modelled value onto the SGC to obtain the D_e used for dating. After outlier rejection (nMAD cutoff = 2.0, accounting for the lower spread of L_n/T_n distributions), the re-normalised L_n/T_n distributions of these samples were relatively tightly distributed and, so, were dated using the CAM.
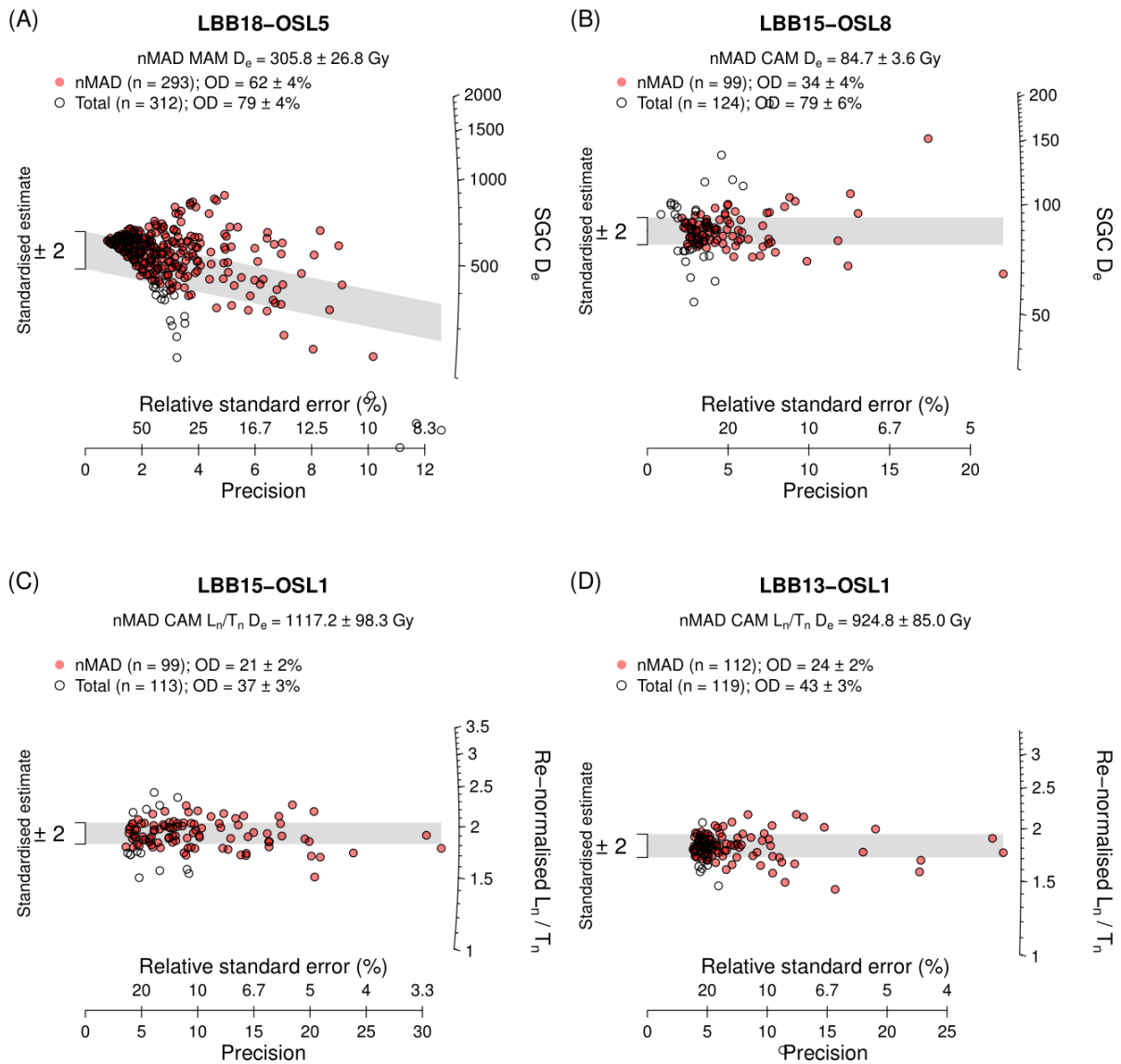
Figure 14: *Examples of distributions of micro-aliquot (A–B) SGC D_e or (C–D) re-normalised L_n/T_n for four samples in stratigraphic order with details of the age models used for dating. Two age models were used: (C–D) a central age model (CAM), and (A) a minimum age model (MAM) using $\sigma_b = 0.35$. Outliers were removed prior to either age models using nMAD cutoff values of (A–B) 1.5 or (C–D) 2.0. The radial plots are centred on the nMAD CAM and the grey bands are centred on the modelled values (nMAD CAM or nMAD MAM). OD refers to the overdispersion value.*

6.3 pIRIR age determination

We corrected the final D_e estimates for a residual dose of 10.4 ± 0.7 Gy (see section 4.2) and divided the result by the corresponding total dose rate for all 14 samples. We also corrected the resulting ages for fading according to Huntley and Lamothe (2001) using a *g*-value of $1.46 \pm 0.61\%$ per decade

obtained from a micro-aliquot fading test of two samples (LBB15-OSL4 and -OSL6; see section 4.4) and the code of Kreutzer (2020) to correct ages accordingly. Since this model is only appropriate for the linear part of the dose-response curve, we consider that the fading-corrected ages are only reliable for the ten samples whose D_e values are smaller than the SGC's D_0 value of 778 Gy. For the other samples (LBB15-OSL1, LBB13-OSL2 and LBB13-OSL1) with D_e above the D_0 value, their fading-corrected ages should be considered as minimum ages only, due to insufficient fading correction. Resulting ages are shown in Table 3; uncertainties are given at 1σ and are derived by combining in quadrature all estimated sources of error. Figure 15 summarises the existing age estimates together with the new pIRIR ages.

In the case of sample LBB13-OSL2, we obtained more accepted data-points using a true single-grain method than using a micro-aliquot method, possibly due to different proportions of contamination, though both grain-sizes yield consistent D_e values (at 1σ). We used the single-grain data (180–212 μm in diameter grains) for age calculation of this sample to make use of the increased statistical reliability of the larger dataset.

Table 3: D_e estimation details for age determination. Equivalent dose (D_e) estimation model, cutoff value used for outlier rejection, number of micro-aliquots accepted during data analysis (after outlier rejection) out of the total measured, overdispersion values of the L_n/T_n or D_e distribution (depending on age model used) before (OD_{total}) and after outlier rejection (OD_{nMAD}), D_e and ages are provided for each sample. All minimum age model (MAM) estimates used a σ_b of 0.35. Age estimates considered to be reliable are shown in bold type.

Sample code	Layer	Age model	Accepted micro-aliquots	OD_{total} (%)	OD_{nMAD} (%)	D_e (Gy)	Age[a] (ka) Fading uncorrected	Age[a] (ka) Fading corrected
LBB18-OSL5	2–3	nMAD MAM D_e [b]	293 / 4100	79 ± 4	62 ± 4	305.8 ± 26.8	60.8 ± 5.8	69.7 ± 8.0
LBB15-OSL8	4a	nMAD CAM D_e [b]	99 / 4400	79 ± 6	34 ± 4	84.7 ± 3.6	15.5 ± 1.0	**17.6 ± 1.6**
LBB-I	4a	nMAD MAM D_e [b]	64 / 3800	100 ± 9	75 ± 8	104.3 ± 17.4	16.5 ± 3.2	**18.8 ± 3.6**
LBB15-OSL4	4b	nMAD MAM D_e [b]	106 / 2900	79 ± 6	65 ± 6	133.2 ± 16.5	22.6 ± 3.1	**25.7 ± 3.8**
LBB15-OSL7	4b	nMAD MAM D_e [b]	88 / 3000	89 ± 7	54 ± 5	108.7 ± 12.9	22.6 ± 3.1	**25.8 ± 3.9**
LBB15-OSL6	4c	nMAD MAM D_e [b]	171 / 1500	90 ± 5	49 ± 3	97.0 ± 9.1	22.7 ± 2.6	**25.9 ± 3.2**
LBB15-OSL5	4c/5	nMAD CAM D_e [b]	90 / 3200	117 ± 8	53 ± 5	162.8 ± 10.3	36.4 ± 2.8	**41.6 ± 3.4**
LBB-II	5	nMAD MAM D_e [b]	34 / 2600	120 ± 13	54 ± 9	159.1 ± 32.6	29.4 ± 6.6	**33.5 ± 9.1**
LBB15-OSL3	5	nMAD MAM D_e [b]	92 / 3800	90 ± 7	56 ± 6	185.3 ± 24.1	35.0 ± 5.0	**40.1 ± 6.2**
LBB15-OSL2	9b	nMAD CAM L_n/T_n [c]	77 / 1800	27 ± 3	20 ± 2	661.2 ± 54.7	163.1 ± 14.9	**188.5 ± 19.9**
LBB15-OSL1	10a	nMAD CAM L_n/T_n [c]	99 / 1000	37 ± 3	21 ± 2	1117.2 ± 98.3	352.5 ± 33.7	409.6 ± 48.5 [d]
LBB15-OSL0	10c	nMAD CAM L_n/T_n [c]	79 / 500	73 ± 6	30 ± 3	585.6 ± 63.3	134.4 ± 15.7	**155.1 ± 22.8**
LBB13-OSL2	10e	nMAD CAM L_n/T_n [c]	43 / 4100	48 ± 5	21 ± 3	989.2 ± 134.3	226.6 ± 32.7	262.5 ± 47.8 [d]
LBB13-OSL1	11	nMAD CAM L_n/T_n [c]	112 / 7300	43 ± 3	24 ± 2	924.8 ± 85.0	163.3 ± 16.5	188.7 ± 26.0 [d]

[a] Ages are obtained by subtracting a residual dose (10.4 ± 0.7 Gy) from the D_e and dividing by the corresponding dose rate.

[b] nMAD cutoff = 1.5

[c] nMAD cutoff = 2.0

[d] Possibility of insufficient fading correction, so these estimates should be considered as minimum ages.
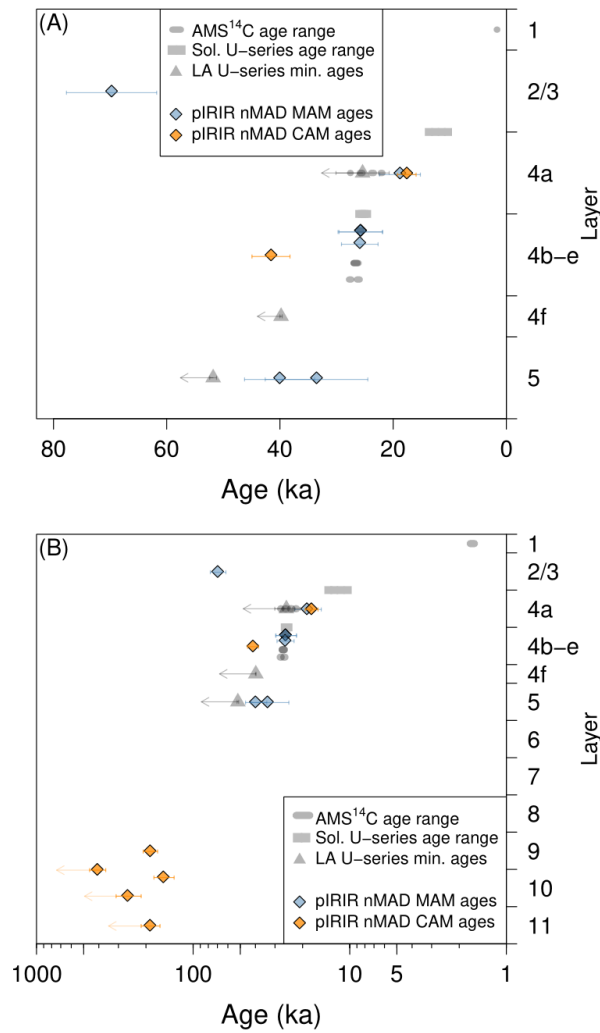
Figure 15: *Summary of previously obtained age estimates (grey symbols), including dating via accelerator mass spectrometry (AMS) radiocarbon (^{14}C), solution (sol.) U-series of speleothems and laser ablation (LA) U-series of teeth (Li et al., 2016b; Brumm et al., 2017), and new micro-aliquot pIRIR ages (blue and orange diamonds) for (A) samples younger than 80 ka, and (B) all samples. pIRIR ages were calculated with the minimum age model (MAM) or central age model (CAM). Minimum age estimates are shown with an arrow pointed towards infinity.*

7   Discussion

7.1 D_e estimation procedure

Higher temperature $pIR_{100}IR_{275}$ signals are known to be more difficult to bleach, so are not ideal to date samples with evidence for partial bleaching, such as those from LBB. If the proportion of unbleached grains is small and the scatter caused by beta dose rate heterogeneity of the underlying populations is large, it is challenging to separate components using common statistical models. Future research might benefit from investigating the potential of other techniques that target a low-fading signal which is more

readily bleached than the $pIR_{100}IR_{275}$ signal. In this way, the large imprecision associated with the age models used for partially bleached samples could potentially be reduced.

7.2 Source of contaminant grains (outliers)

As shown in previous sections, samples from this site contain micro-aliquots that pass acceptance criteria but display anomalously high and low re-normalised L_n/T_n and D_e estimates, when compared to the weighted mean, and are classified as outliers. Due to the natural variability of grains, some scatter is expected in the distributions (Galbraith et al., 2005; Galbraith and Roberts, 2012), but the spread can also be affected by other causes. In addition to bioturbation (which may cause low-dose or high-dose outliers) and incomplete bleaching (causing high-dose outliers only), there is also the possibility that the signal is emitted from contaminant luminescent minerals. We observed the presence of a non-feldspar mineral after density separation of many samples from this site. The contaminant mineral formed sheet-like structures in the dried samples, as expected from mica minerals, such as muscovite. The contaminant was removed during HF etching, according to visual observation of the sample, but it is possible that minute amounts remained. Muscovite is a possible contaminant mineral in our samples, which has been shown to exhibit IRSL (Antohi-Trandafir et al., 2018), though that study did not investigate whether muscovite also presents a pIRIR signal. QEM-EDS analyses of luminescent grains (section 5.2) did not show a significant proportion of mica-type minerals, but 1.4% of grain areas remained unclassified. This small proportion is unlikely to greatly affect an average IRSL signal, especially given the low brightness of muscovite, but a relatively high localised presence of such a contaminant in a hole with no luminescent K-rich feldspar grains could potentially pass rejection criteria and affect the re-normalised L_n/T_n distribution. Identifying the cause for the outliers is beyond the scope of this work, but we suggest the possibility of contaminant minerals to support our rejection of outliers.

7.3 Age estimates

The $pIR_{100}IR_{275}$ signal of the LBB samples contains an unbleachable component, which must be taken into account by subtracting a weighted mean residual dose of 10.4 ± 0.7 Gy from each of the sample D_e estimates prior to age calculation. This residual dose is indistinguishable at 1σ from those obtained previously for two LBB samples measured using single aliquots composed of hundreds of grains (11.5 ± 1.5 Gy and 12.6 ± 1.8 Gy; Li et al., 2016b). It is small (<2%) relative to the weighted mean D_e of the oldest sample in the dataset (LBB15-OSL1), but corresponds to ~12% of the weighted mean D_e for the youngest sample (LBB15-OSL8). Given the broad distribution of residual L_n/T_n ratios obtained for 191 individual micro-aliquots of six samples after an 8 h bleach (Figure 5), and the corresponding overdispersion value of 65 ± 5 % for these data combined, variation in the residual dose is expected to contribute to the scatter in L_n/T_n ratios and D_e values for low-dose samples, in particular. Other factors, however, will also contribute to the spread in D_e values at LBB, especially micro-dosimetry effects

associated with beta dose variations in the typically heterogeneous sediments (e.g., presence of gravel and calcite).

It was not possible to obtain a reliable age for the top-most sample (LBB18-OSL5). Application of a nMAD MAM to the micro-aliquot D_e distribution (Figure 14A) resulted in a D_e estimate of 305.8 ± 26.8 Gy, corresponding to a fading-corrected age of 69.7 ± 8.0 ka. This age estimate clearly does not correspond to the event of interest, which is the deposition of layers 2–3 (culturally sterile, geogenic sediments) with an expected maximum age of 10.3 ka based on U-series dating of an underlying stalagmite. We tested whether the overestimation was caused by erroneous identification of outliers by determining MAM D_e values without any outlier rejection. The MAM D_e estimate of 190.5 ± 15.2 Gy also yields an unexpectedly old age of 41.8 ± 4.0 ka (corrected for fading and residual dose). We conclude that this sample, taken from inside the cave chamber, resulted from a deposition of sediments without substantial bleaching, so that it cannot be used to date the time of layer deposition.

Unlike the other samples from the site, which were all relatively silty or clayey, sample LBB18-OSL5 had very little fine-grained material (<90 µm); instead, the largest size fraction was of grains 125–180 µm (after wet-sieving). This sample also had magnetic minerals and carbonates, the latter being expected, as layers 2 and 3 are known to be calcite-rich. The presence of black magnetic grains has previously only been reported for layer 10. Detailed sedimentological studies should be conducted for this layer to investigate its mode of deposition and inform on the large age disparity in relation to the subsequent layers. Such studies would also inform on the reliability of our interpretations of the samples considered to contain reworked material (layers 4 and 5). We consider the resulting age of LBB18-OSL5 (with rejection of outliers in the same manner as for the other samples) as a maximum deposition age, but expect that the true age would be an order of magnitude younger.

The other eight samples from the top of the stratigraphy were either fully bleached prior to deposition and dated using a nMAD CAM or had a sufficiently bleached component which was dated using the nMAD MAM. We interpret the broad D_e distributions of the latter as being a result of intermittent reworking events that eroded the upper part of the stratigraphy. We hypothesise that, during these erosion events, well-bleached grains were mixed with eroded poorly-bleached material and for this reason use the nMAD MAM to date the well-bleached grain component of these samples.

It was not possible to visually identify discrete components for sample LBB15-OSL5 (Figure S9G), which originates from a transitional/mixed layer (layers 4c/5), possibly due to the large scatter observed for the re-normalised L_n/T_n and D_e distributions. The age obtained by the nMAD CAM D_e analysis of 41.6 ± 3.4 ka more closely matches those of samples from layer 5 (33– >52 ka) than from layer 4 (18–26 ka). We also tested whether a FMM was able to discern D_e values for the two expected layers. Application of a FMM to the SGC D_e distribution did not converge on the expected two-component system (Figure S10); we allowed up to 4 components and used a range of σ_b values (0.1–0.35), choosing the iteration that leads to the highest Bayesian Information Criterion (Table S8). Assuming the FMM component with the highest proportion of micro-aliquots corresponds to the main

depositional layer (which could be either layer 4c or 5), we would expect one of the other components to correspond to the remaining layer. The component with the highest micro-aliquot proportion yields an age which in agreement with those of layer 5, but none of the ages obtained from the other FMM components match ages expected for the overlying layer 4, so we do not consider that an FMM analysis accurately represents the expected sample context of a mixture of two layers.

In the deeper stratigraphic layers (9–11), the overdispersion values are relatively low, suggesting the absence of re-working events or partial bleaching. Low overdispersion values in the presence of partial bleaching would not be unexpected, however, given the relatively large dose accrued since deposition, which would overshadow any residual dose already present at burial.

Sample LBB13-OSL1 (Figure 14D) is known to have cross-cut two sedimentary layers (section 3.1). We chose to use a nMAD CAM for D_e estimation because no two discrete components are apparent in the L_n/T_n distribution. For comparison, we also tested the performance of an FMM analysis equivalent to that used for LBB15-OSL5, but applied to the re-normalised L_n/T_n distribution because of the expected truncation of the SGC at the high D_e values of this sample. Due to the presumed dose-dependency of σ_b of L_n/T_n distributions, we tested two alternative values for σ_b: 0.20 and 0.29. As shown in Figure S11 and Table S9, the model using the lower σ_b value identifies two components (FMM-component 1 represents a single outlier), whereas that using the higher σ_b value does not, but only removes the outlier. However, the resulting residual- and fading-corrected ages of the former model are incongruous with the known depositional environment of this layer: the age of 50.8 ± 19.0 ka of FMM-component 2 is too young to be reasonably encountered at this considerable depth in the stratigraphic sequence (layer 11). Thus, we surmise that the FMM analysis does not identify true distinct components and assume that the two sediment components observed during sampling were deposited penecontemporaneously. We also note that the fading-corrected ages of the main FMM components of both models match at 1σ that obtained from a nMAD CAM analysis, which we consider to be the most reliable age model for dating of this sample.

7.4   Site chronology

MC-ICP-MS U-series dates of intact speleothems (stalagmites) overlying both layers 4a and 4b provide important chronometric information against which to compare our new ages. We obtained two new ages for layer 4a (17.6 ± 1.6 ka; 18.8 ± 3.6 ka), which fall between the U-series dates that confine this layer: 10.3–13.7 ka (top) and 24.6–26.0 ka (bottom). Our ages are also in accordance with existing AMS ^{14}C ages and LA U-series minimum age estimates for this layer (5 ages ranging 21.9 to >27.6 ka) at 2σ. Similarly, our ages for layer 4b (25.7 ± 3.8 and 25.8 ± 3.9 ka) match an AMS ^{14}C age (25.7–26.0 ka) at 1σ. We obtained the first age for layer 4c (25.9 ± 3.2 ka), which matches at 1σ the age bracket of 26.0–26.1 ka expected for this layer from dates of overlying and underlying deposits. We also determined two new ages for layer 5 (33.5 ± 9.1 and 40.1 ± 6.2 ka), which are slightly younger but within 2σ of a

minimum age of 51.8 ± 0.6 ka provided by LA U-series of a bovid tooth excavated from this layer (Burhan et al., in preparation).. In addition, ages for the multiple samples taken from layers 4a, 4b and 5, which originated from opposite ends of the main excavation trench or from different trenches, are indistinguishable at 1σ, confirming the continuity of the stratigraphy.

A measurement approach with resolution at the single grain level, such as our micro-aliquot approach, allows for outliers to be identified and removed from the final analysis as well as for the possibility of accounting for mixing and partial bleaching, leading to more reliable age estimates. For these reasons and due to the smaller correction needed to account for anomalous fading, we consider our new ages for samples LBB-I and LBB-II (18.8 ± 3.6 and 33.5 ± 9.1 ka, respectively) more reliable than the single-aliquot age estimates of $25.3 \, {}^{+\,7.0}_{-\,5.6}$ ka and $44.5 \, {}^{+\,9.9}_{-\,8.4}$ ka presented for these samples in Li et al. (2016b) using a single-aliquot isochron method, though the age estimates are indistinguishable at 1σ.

The updated luminescence chronology for the culturally-rich layer 4 supports the expected range of ~20–40 ka, during which time the site is expected to have been occupied by AMH (Brumm et al., 2017; Burhan et al., in preparation). More broadly, this time range is also in agreement with known AMH occupation at other sites on the island, for example in Goa Topogaro in Central Sulawesi, where radiocarbon ages point to a human presence starting at least from 42 ka (Ono et al., 2020; Fuentes et al., 2021; Ono et al., 2023). However, AMH appear to have been present at least episodically in the Maros karst area by at least 51.2 ka, as suggested by the minimum age for the oldest known figurative cave art in this region (Leang Karampuang; Oktaviana et al., 2024).

The archaeological signature of the deep layers at LBB will be described in detail elsewhere (Burhan and al, in preparation.), but it seems likely that layer 9b is associated with occupation by an unknown, possibly pre-AMH hominin. This layer was dated to 188.5 ± 19.9 ka (LBB15-OSL2). The deepest stone artefact recovered from LBB came from the top of the fluviatile sequence (layer 10a) below this stratum, and animal bones with cut-marks occur in the deepest sedimentary layer uncovered thus far (layer 13, ~8 m depth) (Burhan et al., in preparation). The age obtained for layer 10c of 155.1 ± 22.8 ka is slightly younger than the age for the overlying layer 9b, but indistinguishable at 2σ. The other three ages obtained from layers 10 and 11 should be considered as minimum age estimates due to possibly insufficient fading correction. Sample LBB15-OSL1 stands out with a relatively old age of 409.6 ± 48.5 ka. As mentioned in section 5.1, this sample's beta dose rate is relatively low compared to both its gamma dose rate and the beta dose rates of the other samples from this site. We expect that this sample's total dose rate is underestimated, possibly due to crushing of calcite inclusions during sample preparation for beta-counting. If, instead of the sample's total dose rate of 3.18 ± 0.11 Gy/ka, we use the average total dose rate of the three nearest samples (4.23 ± 0.29 Gy/ka) for age calculation, we obtain a fading-corrected age of 303.4 ± 41.7 ka, which is still overestimated in comparison to the adjacent samples. Until this dose rate issue is resolved, we consider the age obtained for sample LBB15-OSL1 unreliable.

The obtained age range of 130–210 ka (layer 9b) for occupation of the site by an unknown hominin is congruent with the known presence of early hominins in South Sulawesi, e.g., at 118–194 ka at Talepu (van den Bergh et al., 2016), a site ~80 km away from LBB. Since no fossils have been found at either site in Sulawesi, however, more detailed interpretations are currently not possible.

8   Conclusions

Here, we use a 'micro-aliquot' pIRIR procedure on K-rich feldspar to isolate low-fading grains and use a SGC procedure to obtain re-normalised L_n/T_n and D_e distributions for 14 samples from LBB, South Sulawesi. Our results show that aliquots composed of dim or bright grains have similar pIRIR decay curve shapes and thermal stability properties, but fade at different rates. Aliquots composed of dim grains do not pass the micro-aliquot rejection criteria and have a much higher weighted mean fading rate (~9% per decade) than do aliquots composed of bright grains (<3% per decade) (section 4.5 and Figure 9C). A negative correlation between brightness and fading rate has been reported previously for other samples (e.g., Trauerstein et al., 2012; Brown et al., 2015; Guo et al., 2020). By selecting only grains with lower fading rates, samples that have previously proven challenging for optical dating (Li et al., 2016b) may now be dated with the same resolution as true single grains but with a much lower demand on instrument time.

We presented ten new reliable ages using a time-efficient micro-aliquot SGC pIRIR procedure, effectively providing single-grain resolution with minimal fading corrections. The eight ages from the upper layers agree with the previous radiocarbon and U-series chronology, which together span ~10–40 ka. Additionally, we presented the first age estimates of 130–210 ka for a layer with evidence of occupation by an unknown hominin (see also Burhan et al., in preparation). Whereas the SGC we built is specific to LBB, this approach might be usefully applied to date other sites in the volcanic region of South Sulawesi.

References

Antohi-Trandafir, O., Timar-Gabor, A., Vulpoi, A., Bălc, R., Longman, J., Veres, D., and Simon, S.: Luminescence properties of natural muscovite relevant to optical dating of

contaminated quartz samples, Radiat. Meas., 109, 1–7, https://doi.org/10.1016/j.radmeas.2017.12.004, 2018.

Arnold, L. J. and Roberts, R. G.: Stochastic modelling of multi-grain equivalent dose (De) distributions: Implications for OSL dating of sediment mixtures, Quat. Geochronol., 4, 204–230, https://doi.org/10.1016/j.quageo.2008.12.001, 2009.

Arnold, L. J., Roberts, R. G., Galbraith, R. F., and DeLong, S. B.: A revised burial dose estimation procedure for optical dating of young and modern-age sediments, Quat. Geochronol., 4, 306–325, https://doi.org/10.1016/j.quageo.2009.02.017, 2009.

Aubert, M., Brumm, A., Ramli, M., Sutikna, T., Saptomo, E. W., Hakim, B., Morwood, M. J., van den Bergh, G. D., Kinsley, L., and Dosseto, A.: Pleistocene cave art from Sulawesi, Indonesia, Nature, 514, 223–227, https://doi.org/10.1038/nature13422, 2014.

Aubert, M., Lebe, R., Oktaviana, A. A., Tang, M., Burhan, B., Hamrullah, Jusdi, A., Abdullah, Hakim, B., Zhao, J., Geria, I. M., Sulistyarto, P. H., Sardi, R., and Brumm, A.: Earliest hunting scene in prehistoric art, Nature, 576, 442–445, https://doi.org/10.1038/s41586-019-1806-y, 2019.

Auclair, M., Lamothe, M., and Huot, S.: Measurement of anomalous fading for feldspar IRSL using SAR, Radiat. Meas., 37, 487–492, https://doi.org/10.1016/S1350-4487(03)00018-0, 2003.

Barré, P., Velde, B., and Abbadie, L.: Dynamic role of "illite-like" clay minerals in temperate soils: facts and hypotheses, Biogeochemistry, 82, 77–88, https://doi.org/10.1007/s10533-006-9054-2, 2007.

van den Bergh, G. D., Li, B., Brumm, A., Grün, R., Yurnaldi, D., Moore, M. W., Kurniawan, I., Setiawan, R., Aziz, F., Roberts, R. G., Suyono, Storey, M., Setiabudi, E., and Morwood, M. J.: Earliest hominin occupation of Sulawesi, Indonesia, Nature, 529, 208–211, https://doi.org/10.1038/nature16448, 2016.

Blegen, N., Tryon, C. A., Faith, J. T., Peppe, D. J., Beverly, E. J., Li, B., and Jacobs, Z.: Distal tephras of the eastern Lake Victoria basin, equatorial East Africa: correlations, chronology and a context for early modern humans, Quat. Sci. Rev., 122, 89–111, https://doi.org/10.1016/j.quascirev.2015.04.024, 2015.

Bonde, A., Murray, A., and Friedrich, W. L.: Santorini: Luminescence dating of a volcanic province using quartz?, Quat. Sci. Rev., 20, 789–793, 2001.

Brown, N. D., Rhodes, E. J., Antinao, J. L., and McDonald, E. V.: Single-grain post-IR IRSL signals of K-feldspars from alluvial fan deposits in Baja California Sur, Mexico, Quat. Int., 362, 132–138, https://doi.org/10.1016/j.quaint.2014.10.024, 2015.

Brumm, A., Langley, M. C., Moore, M. W., Hakim, B., Ramli, M., Sumantri, I., Burhan, B., Saiful, A. M., Siagian, L., Suryatman, Sardi, R., Jusdi, A., Abdullah, Mubarak, A. P., Hasliana, Hasrianti, Oktaviana, A. A., Adhityatama, S., van den Bergh, G. D., Aubert, M., Zhao, J., Huntley, J., Li, B., Roberts, R. G., Wahyu Saptomo, E., Perston, Y., and Grün, R.: Early human symbolic behavior in the Late Pleistocene of Wallacea, Proc. Natl. Acad. Sci., 114, 4105–4110, https://doi.org/10.1073/pnas.1619013114, 2017.

Brumm, A., Oktaviana, A. A., Burhan, B., Hakim, B., Lebe, R., Zhao, J., Sulistyarto, P. H., Ririmasse, M., Adhityatama, S., Sumantri, I., and Aubert, M.: Oldest cave art found in Sulawesi, Sci. Adv., 7, eabd4648, https://doi.org/10.1126/sciadv.abd4648, 2021.

Bulbeck, D., Sumantri, I., and Hiscock, P.: Leang Sakapao 1, a second dated Pleistocene site from South Sulawesi, Indonesia, Mod. Quat. Res. Southeast Asia, 18, 118–128, 2004.

Burhan, B., Hakim, B., Saiful, A. M., Suryatman, Sumantri, I., Sontag-González, M., Li, B., van den Bergh, G. D., Moore, M. W., Perston, Y., Aubert, M., Grün, R., and Brumm, A.: The Late Pleistocene human occupation sequence at Leang Bulu Bettue in South Sulawesi, Indonesia, in preparation.

Buylaert, J. P., Murray, A. S., Thomsen, K. J., and Jain, M.: Testing the potential of an elevated temperature IRSL signal from K-feldspar, Radiat. Meas., 44, 560–565, https://doi.org/10.1016/j.radmeas.2009.02.007, 2009.

Fuentes, R., Ono, R., Aziz, N., Sriwigati, Alamsyah, N., Sofian, H. O., Miranda, T., Faiz, and Pawlik, A.: Inferring human activities from the Late Pleistocene to Holocene in Topogaro 2, Central Sulawesi through use-wear analysis, J. Archaeol. Sci. Rep., 37, 102905, https://doi.org/10.1016/j.jasrep.2021.102905, 2021.

Galbraith, R. F. and Roberts, R. G.: Statistical aspects of equivalent dose and error calculation and display in OSL dating: An overview and some recommendations, Quat. Geochronol., 11, 1–27, https://doi.org/10.1016/j.quageo.2012.04.020, 2012.

Galbraith, R. F., Roberts, R. G., Laslett, G. M., Yoshida, H., and Olley, J. M.: Optical dating of single and multiple grains of quartz from Jinmium rock shelter, northern Australia: Part I, experimental design and statistical models, Archaeometry, 41, 339–364, https://doi.org/10.1111/j.1475-4754.1999.tb00987.x, 1999.

Galbraith, R. F., Roberts, R. G., and Yoshida, H.: Error variation in OSL palaeodose estimates from single aliquots of quartz: a factorial experiment, Radiat. Meas., 39, 289–307, https://doi.org/10.1016/j.radmeas.2004.03.023, 2005.

Guo, Y.-J., Li, B., and Zhao, H.: Comparison of single-aliquot and single-grain MET-pIRIR De results for potassium feldspar samples from the Nihewan Basin, northen China, Quat. Geochronol., 56, 101040, https://doi.org/10.1016/j.quageo.2019.101040, 2020.

Huntley, D. J. and Lamothe, M.: Ubiquity of anomalous fading in K-feldspars and the measurement and correction for it in optical dating, Can. J. Earth Sci., 38, 1093–1106, https://doi.org/10.1139/e01-013, 2001.

Jacobs, Z., Li, B., Shunkov, M. V., Kozlikin, M. B., Bolikhovskaya, N. S., Agadjanian, A. K., Uliyanov, V. A., Vasiliev, S. K., O'Gorman, K., Derevianko, A. P., and Roberts, R. G.: Timing of archaic hominin occupation of Denisova Cave in southern Siberia, Nature, 565, 594–599, https://doi.org/10.1038/s41586-018-0843-2, 2019.

Kreutzer, S.: calc_FadingCorr(): Apply a fading correction according to Huntley & Lamothe (2001) for a given g-value and a given tc. Function version 0.4.2. In: Kreutzer, S., Burow, C., Dietze, M., Fuchs, M.C., Schmidt, C., Fischer, M., Friedrich, J., 2020. Luminescence: Comprehensive Luminescence Dating Data Analysis. R package version 0.9.7. https://CRAN.R-project.org/package=Luminescence, 2020.

Kreutzer, S. and Burow, C.: analyse_FadingMeasurement(): Analyse fading measurements and returns the fading rate per decade (g-value). Function version 0.1.11. In: Kreutzer, S., Burow, C., Dietze, M., Fuchs, M.C., Schmidt, C., Fischer, M., Friedrich, J., 2020. Luminescence: Comprehensive Luminescence Dating Data Analysis. R package version 0.9.7. https://CRAN.R-project.org/package=Luminescence, 2020.

Kreutzer, S., Burow, C., Dietze, M., Fuchs, M. C., Schmidt, C., Fischer, M., Friedrich, J., Mercier, N., Riedesel, S., Autzen, M., Mittelstraß, D., and Gray, H. J.: Luminescence: Comprehensive Luminescence Dating Data Analysis. R package version 0.9.11., https://CRAN.R-project.org/package=Luminescence, 2021.

Li, B. and Li, S.-H.: Luminescence dating of K-feldspar from sediments: A protocol without anomalous fading correction, Quat. Geochronol., 6, 468–479, https://doi.org/10.1016/j.quageo.2011.05.001, 2011.

Li, B. and Li, S.-H.: A reply to the comments by Thomsen et al. on "Luminescence dating of K-feldspar from sediments: A protocol without anomalous fading correction," Quat. Geochronol., 8, 49–51, https://doi.org/10.1016/j.quageo.2011.10.001, 2012.

Li, B., Roberts, R. G., Jacobs, Z., Li, S.-H., and Guo, Y.-J.: Construction of a 'global standardised growth curve' (gSGC) for infrared stimulated luminescence dating of K-feldspar, Quat. Geochronol., 27, 119–130, https://doi.org/10.1016/j.quageo.2015.02.010, 2015.

Li, B., Jacobs, Z., and Roberts, R. G.: Investigation of the applicability of standardised growth curves for OSL dating of quartz from Haua Fteah cave, Libya, Quat. Geochronol., 35, 1–15, https://doi.org/10.1016/j.quageo.2016.05.001, 2016a.

Li, B., Roberts, R. G., Brumm, A., Guo, Y.-J., Hakim, B., Ramli, M., Aubert, M., Grün, R., Zhao, J., and Wahyu Saptomo, E.: IRSL dating of fast-fading sanidine feldspars from Sulawesi, Indonesia, Anc. TL, 34, 14, 2016b.

Li, B., Jacobs, Z., Roberts, R. G., Galbraith, R., and Peng, J.: Variability in quartz OSL signals caused by measurement uncertainties: Problems and solutions, Quat. Geochronol., 41, 11–25, https://doi.org/10.1016/j.quageo.2017.05.006, 2017.

Li, B., Jacobs, Z., Roberts, R. G., and Li, S.-H.: Single-grain dating of potassium-rich feldspar grains: Towards a global standardised growth curve for the post-IR IRSL signal, Quat. Geochronol., 45, 23–36, https://doi.org/10.1016/j.quageo.2018.02.001, 2018.

Li, B., Jacobs, Z., and Roberts, R. G.: Validation of the LnTn method for De determination in optical dating of K-feldspar and quartz, Quat. Geochronol., 58, 101066, https://doi.org/10.1016/j.quageo.2020.101066, 2020.

More, J. J.: The Levenberg-Marquardt algorithm: implementation and theory, in: Lecture Notes in Mathematics: Numerical Analysis, Springer, Berlin, 105–116, 1978.

Murray, A. S. and Wintle, A. G.: Luminescence dating of quartz using an improved single-aliquot regenerative-dose protocol, Radiat. Meas., 32, 57–73, https://doi.org/10.1016/S1350-4487(99)00253-X, 2000.

O'Gorman, K., Brink, F., Tanner, D., Li, B., and Jacobs, Z.: Calibration of a QEM-EDS system for rapid determination of potassium concentrations of feldspar grains used in optical dating, Quat. Geochronol., 61, 101123, https://doi.org/10.1016/j.quageo.2020.101123, 2021.

Oktaviana, A. A., Joannes-Boyau, R., Hakim, B., Burhan, B., Sardi, R., Adhityatama, S., Hamrullah, Sumantri, I., Tang, M., Lebe, R., Ilyas, I., Abbas, A., Jusdi, A., Mahardian, D. E., Noerwidi, S., Ririmasse, M. N. R., Mahmud, I., Duli, A., Aksa, L. M., McGahan, D., Setiawan, P., Brumm, A., and Aubert, M.: Narrative cave art in Indonesia by 51,200 years ago, Nature, 1–5, https://doi.org/10.1038/s41586-024-07541-7, 2024.

Ono, R., Fuentes, R., Pawlik, A., Sofian, H. O., Sriwigati, Aziz, N., Alamsyah, N., and Yoneda, M.: Island migration and foraging behaviour by anatomically modern humans during the late Pleistocene to Holocene in Wallacea: New evidence from Central Sulawesi, Indonesia, Quat. Int., 554, 90–106, https://doi.org/10.1016/j.quaint.2020.03.054, 2020.

Ono, R., Sofian, H. O., Fuentes, R., Aziz, N., Ririmasse, M., Geria, I. M., Katagiri, C., and Pawlik, A.: Early modern human migration into Sulawesi and Island adaptation in Wallacea, World Archaeol., 54, 229–243, https://doi.org/10.1080/00438243.2023.2172074, 2023.

Peng, J. and Li, B.: Single-aliquot regenerative-dose (SAR) and standardised growth curve (SGC) equivalent dose determination in a batch model using the R Package 'numOSL,' Anc. TL, 35, 32–53, 2017.

Peng, J., Dong, Z., Han, F., Long, H., and Xiangjun, L.: R package numOSL: numeric routines for optically stimulated luminescence dating, Anc. TL, 31, 41–48, 2013.

Porat, N., Faerstein, G., Medialdea, A., and Murray, A. S.: Re-examination of common extraction and purification methods of quartz and feldspar for luminescence dating, Anc. TL, 33, 22–30, 2015.

Powell, R., Hergt, J., and Woodhead, J.: Improving isochron calculations with robust statistics and the bootstrap, Chem. Geol., 185, 191–204, https://doi.org/10.1016/S0009-2541(01)00403-X, 2002.

Prescott, J. R. and Hutton, J. T.: Cosmic ray contributions to dose rates for luminescence and ESR dating: large depths and long-term time variations, Radiat. Meas., 23, 497–500, 1994.

Preusser, F., Degering, D., Fuchs, M., Hilgers, A., Kadereit, A., Klasen, N., Krbetschek, M., Richter, D., and Spencer, J. Q. G.: Luminescence dating: basics, methods and applications, EampG Quat. Sci. J., 57, 95–149, https://doi.org/10.3285/eg.57.1-2.5, 2008.

R Core Team: R: a language and environment for statistical computing. Version 1.2.1335., Vienna, Austria, 2016.

Raheb, A. and Heidari, A.: Effects of clay mineralogy and physico-chemical properties on potassium availability under soil aquic conditions, J. Soil Sci. Plant Nutr., 12, 747–761, https://doi.org/10.4067/S0718-95162012005000029, 2012.

Roberts, R. G., Galbraith, R. F., Yoshida, H., Laslett, G. M., and Olley, J. M.: Distinguishing dose populations in sediment mixtures: a test of single-grain optical dating procedures using mixtures of laboratory-dosed quartz, Radiat. Meas., 32, 459–465, https://doi.org/10.1016/S1350-4487(00)00104-9, 2000.

Rousseeuw, P. J., Debruyne, M., Engelen, S., and Hubert, M.: Robustness and outlier detection in chemometrics, Crit. Rev. Anal. Chem., 36, 221–242, https://doi.org/10.1080/10408340600969403, 2006.

Sontag-González, M., Li, B., O'Gorman, K., Sutikna, T., Jatmiko, Jacobs, Z., and Roberts, R. G.: Establishing a pIRIR procedure for De determination of composite mineral grains from volcanic terranes: A case study of sediments from Liang Bua, Indonesia, Quat. Geochronol., 65, 101181, https://doi.org/10.1016/j.quageo.2021.101181, 2021.

Thiel, C., Buylaert, J.-P., Murray, A., Terhorst, B., Hofer, I., Tsukamoto, S., and Frechen, M.: Luminescence dating of the Stratzing loess profile (Austria) – Testing the potential of an elevated temperature post-IR IRSL protocol, Quat. Int., 234, 23–31, https://doi.org/10.1016/j.quaint.2010.05.018, 2011.

Thomsen, K. J., Murray, A. S., Jain, M., and Bøtter-Jensen, L.: Laboratory fading rates of various luminescence signals from feldspar-rich sediment extracts, Radiat. Meas., 43, 1474–1486, https://doi.org/10.1016/j.radmeas.2008.06.002, 2008.

Trauerstein, M., Lowick, S., Preusser, F., Rufer, D., and Schlunegger, F.: Exploring fading in single grain feldspar IRSL measurements, Quat. Geochronol., 10, 327–333, https://doi.org/10.1016/j.quageo.2012.02.004, 2012.

Tsukamoto, S. and Duller, G. A. T.: Anomalous fading of various luminescence signals from terrestrial basaltic samples as Martian analogues, Radiat. Meas., 43, 721–725, https://doi.org/10.1016/j.radmeas.2007.10.025, 2008.

Westaway, K. E. and Roberts, R. G.: A dual-aliquot regenerative-dose protocol (DAP) for thermoluminescence (TL) dating of quartz sediments using the light-sensitive and isothermally stimulated red emissions, Quat. Sci. Rev., 25, 2513–2528, https://doi.org/10.1016/j.quascirev.2005.06.010, 2006.

Wintle, A. G.: Luminescence dating: laboratory procedures and protocols, Radiat. Meas., 27, 769–817, https://doi.org/10.1016/S1350-4487(97)00220-5, 1997.

Supplementary Information

S1 Stratigraphy and previous chronology

The top-most layer (layer 1) is Neolithic and charcoal from this layer has been dated to 1.6–1.7 ka cal BP. Layers 2 and 3 are calcite-rich silts intercalated with cemented layers of flowstone that cap the Pleistocene deposits below it. Most archaeological finds are located in layer 4, composed of silty clays (4a–e) and sandy clay (4f). Layer 4a spans 22–26 ka, dated by solution MC-ICP-MS U-series of two *in situ* stalagmites and by isochron pIRIR. Layers 4b–e span ~26–30 ka according to dates obtained from solution MC-ICP-MS U-series of stalagmites and AMS ^{14}C dating of shells. Minimum ages have been obtained for the lower layers by LA U-series of faunal teeth: an anoa tooth from layer 4f, which is apparent only in the southeast trench walls, was dated to 39.8 ± 0.2 ka and a bovid molar from the base of layer 5 was dated to 51.8 ± 0.6 ka. Layer 5 was dated by isochron pIRIR of K-rich feldspar to $44.5^{+9.9}_{-8.4}$ (Li et al., 2016).

Excavation details of the deeper deposits are described in Burhan et al. (in preparation). No chronological information has been published yet. Layer 9b consists of a yellow-grey clay matrix and contains the oldest stone artefact found at the site. Layer 10a is a yellow-brown clayey and silty layer with calcite and black magnetic inclusions; layer 10b is composed of a dark clay with magnetic inclusions; layer 10c is composed of a yellow sandy material; and layer 10d is similar to layer 10b. Layer 11 consists of fine-banded grey silts.

In recent field seasons, the excavation has been expanded towards the west wall, revealing a more complex stratigraphy than initially believed. There is evidence of a series of erosional events of layers 4 and 5, during which the upper part of the layers was washed away (Burhan et al, in preparation). In certain sections, the lower part of section 4 (sublayer 4c) appears to be mixed with layer 5, possibly as a result of these erosion events (note that sublayers 4d–f are not apparent in this area). The timing of the erosional events and the possible presence of hiatuses between layers 2/3 and 4 as well as 4 and 5, due to material being washed away, are still open questions.

Table S4: *Summary of previous age estimates for LBB. Dating techniques include accelerator mass spectrometry (AMS) radiocarbon dating of charcoal and freshwater gastropod (Tylomelania perfecta) shells, solution multi-collector inductively coupled plasma mass spectrometry U-series (Sol. U-series) dating of in situ stalagmites, laser ablation (LA) U-series dating of faunal remains and isochron single-aliquot (SA) pIRIR dating of sediments. AMS radiocarbon estimates from Brumm et al. (2017) were re-calibrated using the calibration curves IntCal20 (Reimer et al., 2020) and its equivalent for the southern hemisphere SHCal20 (Hogg et al., 2020). The two curves were mixed to account for the tropical location of LBB, using a ratio of 40:60 between the Northern and Southern curves, based on the site's latitude and allowing for 10% variation.*

Layer	Sample code	Sample type	Depth (cm), (Square)	Method	Previous age (ka or cal ka BP)	Recalibrated age (cal ka BP)
1	Wk-37740	Charcoal	30–40 (A2)	AMS ^{14}C	1.6–1.7	1.6–1.7
4a (top)	485	Stalagmite	95–110 (A1)	Sol. U-series	10.3–13.7	-
4a	Wk-37742	Shell	131 (A1)	AMS ^{14}C	21.8–22.2	21.9–22.2
4a	Wk-42070	Shell	210 (-H2)	AMS ^{14}C	23.5–24.1	23.4–23.9
4a	LBB-I	Sediment	160 (A2, S)	SA pIRIR	$25.3^{+7.0}_{-5.6}$	-
4a	LBB-3	Pig molar	156 (A1)	LA U-series	25.4 ± 4.7	-
4a	Wk-37743	Shell	168 (A1)	AMS ^{14}C	27.2–27.6	27.3–27.6
4a	Wk-42069	Shell	226 (-H2)	AMS ^{14}C	25.5–26.0	25.4–25.9
4b (top)	605	Stalagmite	151–169 (A1)	Sol. U-series	24.6–26.0	-
4b	Wk-42065	Shell	233 (-H2)	AMS ^{14}C	25.6–26.0	25.7–26.0
4d	Wk-42067	Shell	255 (-H2)	AMS ^{14}C	26.2–27.0	26.1–27.0
4d	Wk-42068	Shell	281 (-H2)	AMS ^{14}C	26.1–27.0	26.1–27.0
4e	Wk-42071	Shell	279 (-G2)	AMS ^{14}C	27.4–27.9	27.4–27.8
4e	Wk-42066	Shell	306 (-H2)	AMS ^{14}C	25.8–26.4	25.9–26.4
4f	3612	Anoa tooth	191 (-A1)	LA U-series	39.8 ± 0.2	-
5	LBB-II	Sediment	205 (A1, S)	SA pIRIR	$44.5^{+9.9}_{-8.4}$	-
5	3609	Bovid molar	232 (-A1)	LA U-series	51.8 ± 0.6	-

S2 pIRIR standardised growth curve

Table S5: *Number of micro-aliquots measured, rejected and accepted for use in SGC construction using Approach A or B. The seven criteria are those described in the man text.*

Sample code	Approach	Grain size (μm)	Number measured	Number rejected by each criterion							Number accepted
				1	2	3	4	5	6	7	
LBB18-OSL5	A	90–125	300	251	0	1	27	0	0	-	21 (7.0%)
LBB15-OSL8	A	90–125	200	193	0	0	1	0	0	-	6 (3.0%)
	B	90–125	700	680	-	-	2	0	0	-	18 (2.6%)
LBB-I	A	90–180	500	477	0	0	8	0	0	-	15 (3.0%)
	B	90–180	800	790	-	-	1	0	0	-	9 (1.1%)
LBB15-OSL7	A	90–125	100	96	0	0	2	0	0	-	2 (2.0%)
	B	90–125	100	98	-	-	0	0	0	-	2 (2.0%)
LBB15-OSL6	A	90–125	1100	923	1	2	73	0	0	-	101 (9.2%)
	B	90–125	2100	1841	-	-	28	0	0	-	231 (11.0%)
LBB15-OSL5	B	90–125	300	287	-	-	0	0	0	-	13 (4.3%)
LBB-II	A	90–180	200	190	1	0	4	0	0	-	5 (2.5%)
	B	90–180	800	789	-	-	0	0	1	-	11 (1.4%)
LBB15-OSL3	A	90–125	300	293	0	0	1	0	0	-	6 (2.0%)
	B	90–125	1200	1169	-	-	2	0	1	-	28 (2.4%)
LBB15-OSL2	B	90–125	700	669	-	-	1	0	0	-	30 (4.3%)
LBB15-OSL1	A	90–125	1300	1201	2	0	40	0	1	-	56 (4.4%)
	B	90–125	900	827	-	-	6	0	0	-	67 (7.4%)
LBB15-OSL0	A	90–125	100	94	0	0	3	0	0	-	3 (3.0%)
	B	90–125	500	413	-	-	10	0	0	-	77 (15.4%)
LBB13-OSL2	B	90–180	1000	980	-	-	6	0	3	-	11 (1.4%)
LBB13-OSL1	A	90–125	100	92	0	0	2	0	0	-	6 (6.0%)
	B	90–125	100	93	-	-	0	0	0	-	7 (7.0%)
Total	A	90–125 or 90–180	4200	3810	4	3	161	0	1	-	221 (5.3%)
	B	90–125 or 90–180	9200	8636	-	-	56	0	5	-	504 (5.5%)

Table S6: *Number of micro-aliquots measured, rejected (for each criterion applied) and accepted using Approach C. Measurements were made for signal recovery (SR) and residual-dose (RD) tests, or for De determination. The seven criteria are those described in the text. Individual grains (180–212 µm in diameter) were measured for three samples (LBB15-OSL6, LBB15-OSL5 and LBB13-OSL2) for comparison of D_e values; data are shown in italics.*

| Sample code | Type | Grain size (µm) | Number measured | Number rejected by each criterion | | | | | | | Number accepted |
				1	2	3	4	5	6	7	
LBB18-OSL5	D_e	90–125	4100	3671	-	-	-	0	53	1	375 (9.2%)
	RD test	90–125	1300	1218	-	-	-	0	6	-	76 (5.8%)
LBB15-OSL8	D_e	90–125	4400	4271	-	-	-	0	3	0	126 (2.9%)
	RD test	90–125	300	288	-	-	-	0	0	-	12 (4.0%)
LBB-I	D_e	90–180	3800	3710	-	-	-	0	6	0	84 (2.2%)
LBB15-OSL4	D_e	90–125	2900	2773	-	-	-	0	2	1	124 (4.3%)
LBB15-OSL7	D_e	90–125	3000	2877	-	-	-	2	4	1	116 (3.9%)
LBB15-OSL6	D_e	90–125	1500	1270	-	-	-	5	1	0	224 (14.9%)
	RD test	90–125	1300	1167	-	-	-	0	4	0	129 (9.9%)
	SR test	90–125	4100	3678	-	-	-	1	5	0	416 (10.1%)
	D_e	*180–212*	*1600*	*1519*	*-*	*-*	*-*	*5*	*1*	*1*	*74 (4.7%)*
LBB15-OSL5	D_e	90–125	3200	3072	-	-	-	0	3	0	125 (3.9%)
	D_e	*180–212*	*600*	*564*	*-*	*-*	*-*	*0*	*0*	*0*	*36 (6.0%)*
LBB-II	D_e	90–180	2600	2549	-	-	-	0	2	0	49 (1.9%)
LBB15-OSL3	D_e	90–125	3800	3687	-	-	-	0	4	1	108 (2.8%)
	RD test	90–125	800	781	-	-	-	0	0	-	19 (4.2%)
LBB15-OSL2	D_e	90–125	1800	1711	-	-	-	3	3	1	82 (4.6%)
LBB15-OSL1	D_e	90–125	1000	886	-	-	-	0	1	0	113 (11.3%)
	RD test	90–125	900	859	-	-	-	0	1	-	40 (10.2%)
LBB15-OSL0	D_e	90–125	500	405	-	-	-	0	3	0	92 (18.4%)
	RD test	90–125	300	275	-	-	-	0	2	-	23 (7.7%)
LBB13-OSL2	D_e	90–180	1800	1773	-	-	-	5	6	1	15 (0.8%)
	D_e	*180–212*	*4100*	*4048*	*-*	*-*	*-*	*0*	*2*	*0*	*50 (1.2%)*
LBB13-OSL1	D_e	90–125	7300	7165	-	-	-	2	11	3	119 (1.6%)

S2.1 SGC construction for D_e estimation

A total of 725 micro-aliquots out of the 13,400 measured using Approaches A (n = 221) or B (n = 504) passed the rejection criteria and their L_x/T_x ratios were used for SGC construction. All of the L_x/T_x ratios, before and after LS-normalisation, are displayed in Figure S16A and B, respectively. The latter shows that the dose response of K-rich feldspar grains from LBB can be satisfactorily described by a single SGC. Figure S16C shows the goodness-of-fit of the SGC to the L_x/T_x ratios for individual micro-aliquots of three different samples.

Re-normalised L_n/T_n distributions were obtained from the L_n/T_n and L_{R1}/T_{R1} ratios (Approach C), scaled so that projection of L_{R1}/T_{R1} onto the SGC would fall on the given regenerative dose (Eq. 10 in Li et al., 2015a). These distributions were then used for SGC D_e estimations.

(A)   (B)

(C)
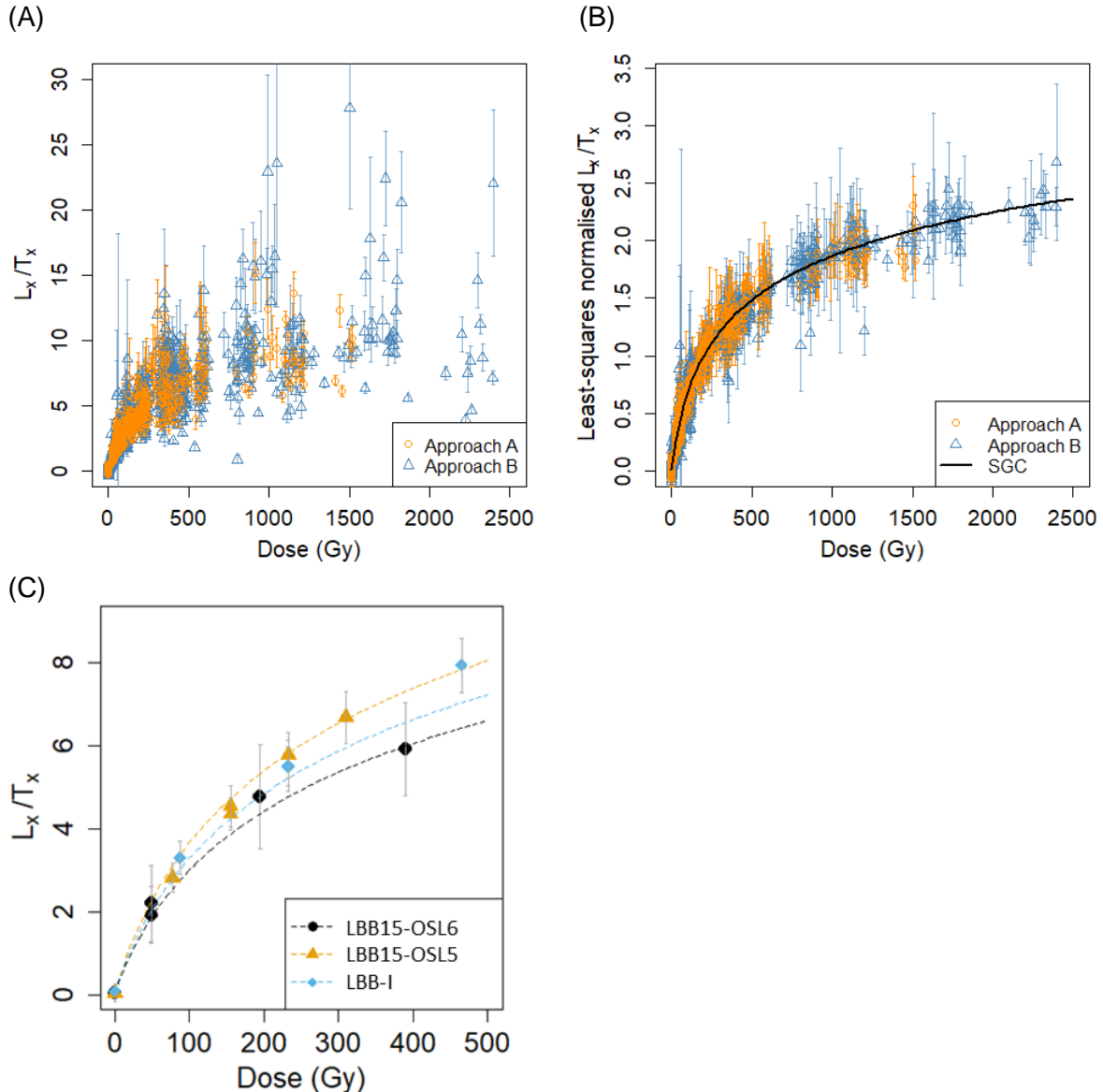
Figure S16: *Dose-response curves (DRCs) and standardised growth curve (SGC). (A) Micro-aliquot L_x/T_x ratios (before LS-normalisation) used to build the SGC. (B) SGC constructed from the L_x/T_x ratios in panel (A) after LS-normalisation. (C) L_x/T_x ratios for individual micro-aliquots of three samples, with the SGC divided by the LS-normalisation scaling factor for each micro-aliquot indicated by the dashed lines.*

S2.2 SGC D_e reliability tests

The SGC approach allows for fewer measurements per micro-aliquot, but assumes that all micro-aliquots share a common DRC (i.e., the SGC). In this section, the results of reliability tests are reported that confirm that the SGC method yields reliable estimates of D_e.

The 725 micro-aliquots included in the SGC yielded 2079 L_x/T_x ratios, of which 1903 (92%) match the SGC estimates at 2σ (Figure S17A). The deviation of individual L_x/T_x ratios from the SGC is not correlated with dose (Figure S17B) and can be explained by measurement uncertainties and inherent grain variability.

We also directly compared the SAR and SGC D_e values obtained for the micro-aliquots measured using Approach A. Of the 221 measured micro-aliquots, only 120 yielded D_e values for comparison; the remainder were rejected primarily due to insufficient measured dose points (no interpolation possible) (23%); an rse of $D_e > 50\%$ (17%); and oversaturation (i.e., L_n/T_n value above the saturation of the fitted DRC, so no interpolation possible; 6%). SGC D_e values were calculated by projecting the re-normalised L_n/T_n ratios for individual micro-aliquots onto the SGC, rather than projecting the L_n/T_n ratios onto aliquot-specific DRCs, as is done using the standard SAR procedure. Figure S17C compares the SAR and SGC D_e values for all 120 micro-aliquots: 100% are indistinguishable at 2σ, which supports the reliability of the SGC for D_e determination, at least to doses of up to ~1000 Gy.
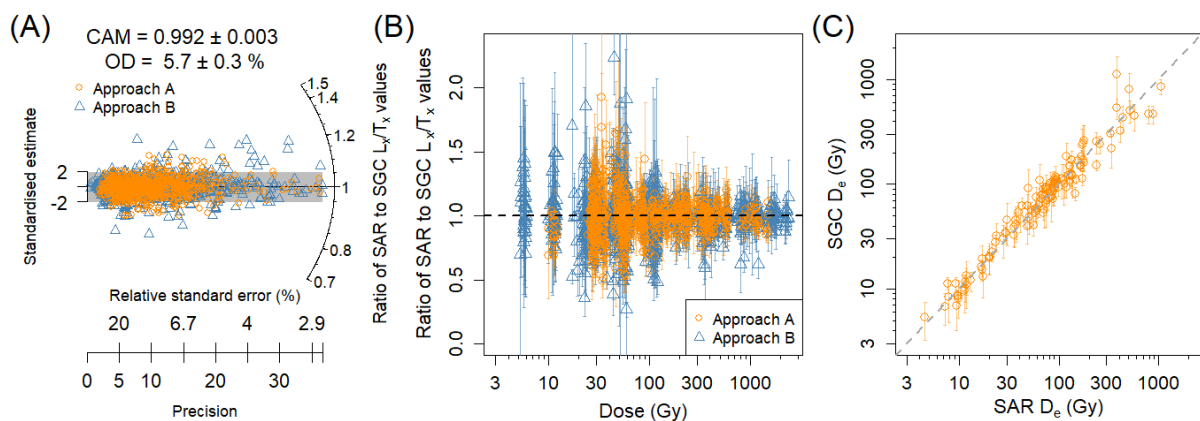

Figure S17: *Comparison of SAR and SGC procedures. (A) Variability in measured micro-aliquot L_x/T_x ratios compared to the fitted SGC values; the weighted mean (CAM) and overdispersion (OD) values are indicated. (B) Same data as in panel (A) plotted as a function of given dose. (C) Comparison of D_e values obtained for 120 micro-aliquots using the standard SAR procedure and SGC method.*
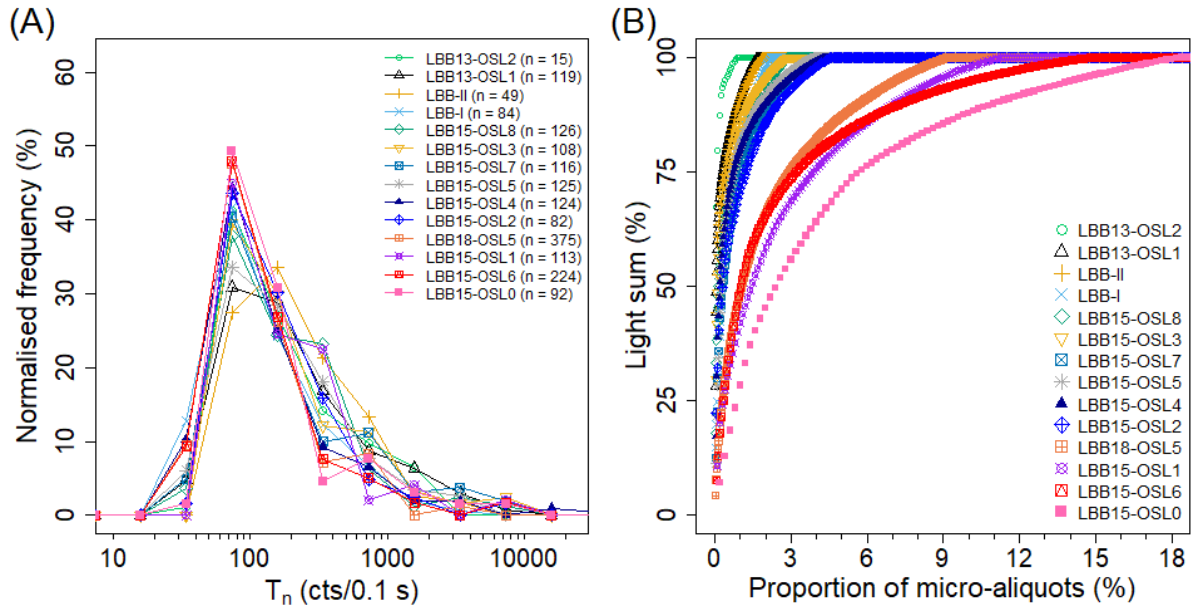
Figure S18: *pIR$_{100}$IR$_{275}$ T_n signal intensities. (A) Frequency polygons of T_n intensity of micro-aliquots used for D_e estimation for all samples, normalised to a cohort size of 1 (n, number of accepted micro-aliquots for each sample). (B) Cumulative light-sum plot for each sample. Micro-aliquots are sorted by decreasing brightness of T_n and their relative contributions to the total signal are summed sequentially, from brightest to dimmest.*

Table S7: *Results of residual-dose tests, summarising the number of micro-aliquots (n), weighted mean (unlogged CAM) residual doses and overdispersion (OD) values of the re-normalised residual L_n/T_n and resulting D_e distributions obtained for each bleach duration, for each sample and for all samples combined (bold type). The weighted mean (CAM) D_e values are also listed for each sample.*

Sample code	Bleach length (h)	n	Residual dose (Gy)	Residual dose / sample D_e (%)	Re-normalised residual L_n/T_n OD (%)	Residual dose OD (%)	Sample CAM D_e (Gy)
LBB15-OSL0	8	23	13.1 ± 1.6	4.4	38 ± 9	50 ± 12	291.9 ± 51.6
LBB15-OSL1	4	21	17.7 ± 2.1	1.8	36 ± 9	42 ± 11	1007.2 ± 128.4
	8	19	10.0 ± 1.7	1.0	48 ± 14	65 ± 19	1007.2 ± 128.4
LBB15-OSL3	4	16	13.8 ± 1.9	6.0	37 ± 10	52 ± 14	235.9 ± 24.6
	8	3	5.0 ± 1.7	2.2	zero	zero	235.9 ± 24.6
LBB15-OSL6	4	71	6.7 ± 0.7	3.9	61 ± 9	84 ± 13	169.8 ± 11.8
	8	58	7.9 ± 0.9	4.6	64 ± 10	83 ± 14	169.8 ± 11.8
LBB15-OSL8	8	12	10.6 ± 2.5	12.2	55 ± 19	85 ± 31	84.6 ± 6.7
LBB18-OSL5	8	76	11.9 ± 1.3	1.8	71 ± 9	84 ± 12	668.5 ± 41.3
All samples	**8**	**191**	**10.4 ± 0.7**	**-**	**65 ± 5**	**79 ± 7**	**-**

Table S8: Results of signal recovery tests, summarising the number of accepted micro-aliquots, weighted mean (CAM) signal recovery ratios and overdispersion values of the $L_n/T_{n'}$ and D_e distributions for each given dose and for all micro-aliquots combined (bold type). The overdispersion value of the $L_{n'}/T_{n'}$ distribution of the 545 Gy dataset is atypically large due to one outlier (ratio <0.1); the overdispersion value without this one outlier is given in parentheses.

Mean given dose (Gy)	Number of micro-aliquots	Weighted mean signal recovery ratio	$L_{n'}/T_{n'}$ overdispersion (%)	nMAD $L_{n'}/T_{n'}$ overdispersion (%)	Signal recovery ratio overdispersion (%)
59	87	0.92 ± 0.03	23 ± 2	18 ± 2	20 ± 2
230	85	1.01 ± 0.03	22 ± 2	18 ± 2	20 ± 2
270	101	0.97 ± 0.03	24 ± 2	19 ± 2	18 ± 2
545	85	0.99 ± 0.07	59 ± 5 (18 ± 2)	16 ± 2	17 ± 2
813	58	0.92 ± 0.03	18 ± 2	14 ± 2	15 ± 2
All doses	**416**	**0.97 ± 0.02**	**-**	**-**	**19 ± 1**

S3 Dependence of D_e estimates on grain size

Although dim grains (Cohort B) can be rejected from micro-aliquot measurements using criterion 1, they could potentially contribute to the pIRIR signal if smaller grain sizes are used, because each hole would be occupied by several grains—up to 10 grains of 90–125 µm diameter, as with many of the LBB micro-aliquots measured in this study. This may result in micro-aliquots passing the brightness criterion, leading to age underestimation if the dim grains are associated with higher fading rates. The bright grains (Cohort A) have a mean L_x intensity ~50 times that of dim grains (Cohort B), however, so if several dim grains occupy the same hole as even just one bright grain, then the latter will dominate the signal. This suggests that micro-aliquots should yield reliable estimates of D_e, but further confidence would be gained if it could be shown that as many as 10 dim grains would not produce a sufficiently bright signal to pass criterion 1.

To test if this were so, we compared the results for 'small' (90–125 µm) and 'large' (180–212 µm) grains of samples LBB15-OSL5 and -OSL6, and 'small' (90–180 µm) and 'large' (180–212 µm) grains of LBB13-OSL2. True single-grain measurements of the 'large' grains resulted in just 6.0% (LBB15-OSL5), 4.7% (LBB15-OSL6) and 1.2% (LBB13-OSL2) of the measured grains being sufficiently bright to pass criterion 1 (Table S6). Probability calculations suggest that if 6% of the measured grains pass criterion 1, then the likelihood of having at least one bright grain in a hole containing 10 grains is 46% [1]. For a hole containing 5 grains, the probability of at least one bright grain

---

[1] There are two possibilities for each grain: emit (6%) or not-emit (94%). The probability of ten grains not emitting is 0.94^{10} (i.e., 54%), so all other scenarios include at least one grain emitting. The sum of probabilities for all

being present is 27% (i.e., $1-0.94^5$). If every hole is loaded with 5–10 grains, we would therefore expect 27–46% of measured micro-aliquots to pass criterion 1. For LBB15-OSL6 and LBB13-OSL2, the expected proportions of bright grains in micro-aliquots composed of 5–10 grains are 21–38% and 6–11%, respectively. If the proportion of micro-aliquots passing criterion 1 is higher than these expected values, then it would indicate that the combined signal from 5–10 dim (Cohort B) grains is sufficient to pass criterion 1 and may include contributions from dim grains with high fading rates. Our experimental data for all three samples yielded much lower proportions of micro-aliquots passing criterion 1—3.9% (LBB15-OSL5), 14.9% (LBB15-OSL6) and 0.8% (LBB13-OSL2) (Table S6)—which indicates that Cohort B grains are not bright enough collectively to pass criterion 1. Our micro-aliquot results, therefore, predominantly reflect the contributions of Cohort A grains, effectively making them equivalent to true single grains.

The lower acceptance rate of micro-aliquots compared to single grains for LBB15-OSL5 (3.9% and 6.0%, respectively) and LBB13-OSL2 (0.8% and 1.2%, respectively) may be due to a higher proportion of non-luminescent contaminants (e.g., clay conglomerates) in the smaller grain-size fractions. Elemental mapping of 180–212 µm grains identified a small percentage of clay minerals, even in grains that passed criterion 1 (see section 5.2 in the main text). Clay minerals will likely be more common as contaminants of micro-aliquots than of true single grains, because the smaller grains were not hand-picked and placed into each hole, unlike single grains. Thus, in the absence of visual quality control during disc loading, the micro-aliquot approach may not be appropriate for all types of sample.

We also compared T_n intensity for 'small' and 'large' grains, because if the micro-aliquot signals consisted of emissions from multiple grains, then their response to a given dose could be higher than the single-grain T_n signals, depending on the total volume of multiple individual grains. The distributions of T_n intensities for micro-aliquots of LBB15-OSL5, LBB15-OSL6 and LBB13-OSL2 are similar to their single-grain counterparts (Figure S19), supporting the equivalence of results obtained for small (90–125 µm and 90–180 µm) and large (180–212 µm) grains.

---

scenarios has to be 100%, so that the remaining probability ($100\% - 0.94^{10} = 46\%$) corresponds to at least one grain emitting.
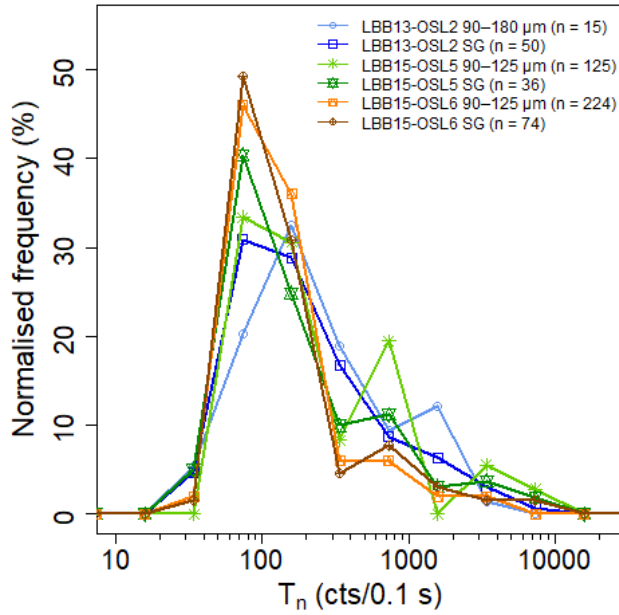
Figure S19: *Frequency polygons of T_n intensity measured for micro-aliquots and single grains (SG; 180–212 μm) of LBB15-OSL5 (light and dark green, respectively), LBB15-OSL6 (orange and brown, respectively) and LBB13-OSL2 (light and dark blue, respectively). Each dataset is normalised to a cohort size of 1 (n: number of accepted micro-aliquots or single grains).*

Ultimately, the best measure of equivalence between the micro-aliquots and true single grains is a direct comparison of their D_e distributions. Ideally, the D_e estimates should differ only due to the size-dependent components of the total dose rate (i.e., internal dose rate and external beta dose rate). Based on the differences in dose rate for micro-aliquots and single grains, we would expect the weighted mean D_e values of micro-aliquots to be smaller than those of single grains by ~5% (LBB15-OSL5), ~6% (LBB15-OSL6) and ~4% (LBB13-OSL2). The micro-aliquots and single grains accepted for each sample have similar re-normalised L_n/T_n distributions (Figure S20), with overdispersion values consistent at 2σ (after outlier rejection): 43 ± 3% and 38 ± 5% (LBB15-OSL5), 43 ± 2% and 50 ± 5% (LBB15-OSL6), and 28 ± 7% and 21 ± 3% (LBB13-OSL2) for the micro-aliquot and single-grain distributions, respectively. The corresponding weighted mean D_e values, calculated after rejecting outliers using the nMAD, are displayed in Figure S20. The ratios of the micro-aliquot to single-grain weighted mean D_e values—0.96 ± 0.16 (LBB15-OSL5), 0.92 ± 0.13 (LBB15-OSL6) and 0.66 ± 0.19 (LBB13-OSL2)—are consistent at either 1σ or 2σ with their expected ratios (0.94–0.96). The large uncertainties associated with LBB13-OSL2 stem both from the small number of micro-aliquots (n = 13) and single grains (n = 44) remaining after outlier rejection, and from the imprecision inherent in D_e estimation at high doses. Ratios of the ages obtained by dividing the weighted mean D_e values by the corresponding dose rates are consistent with unity at 1σ or 2σ: 0.95 ± 0.15 (LBB15-OSL5), 1.00 ± 0.13 (LBB15-OSL6) and 0.73 ± 0.22 (LBB13-OSL2). For the LBB samples, therefore, we consider micro-

aliquots that pass the rejection criteria to be equivalent to single grains, with both size fractions dominated by emissions from bright grains with low rates of fading.
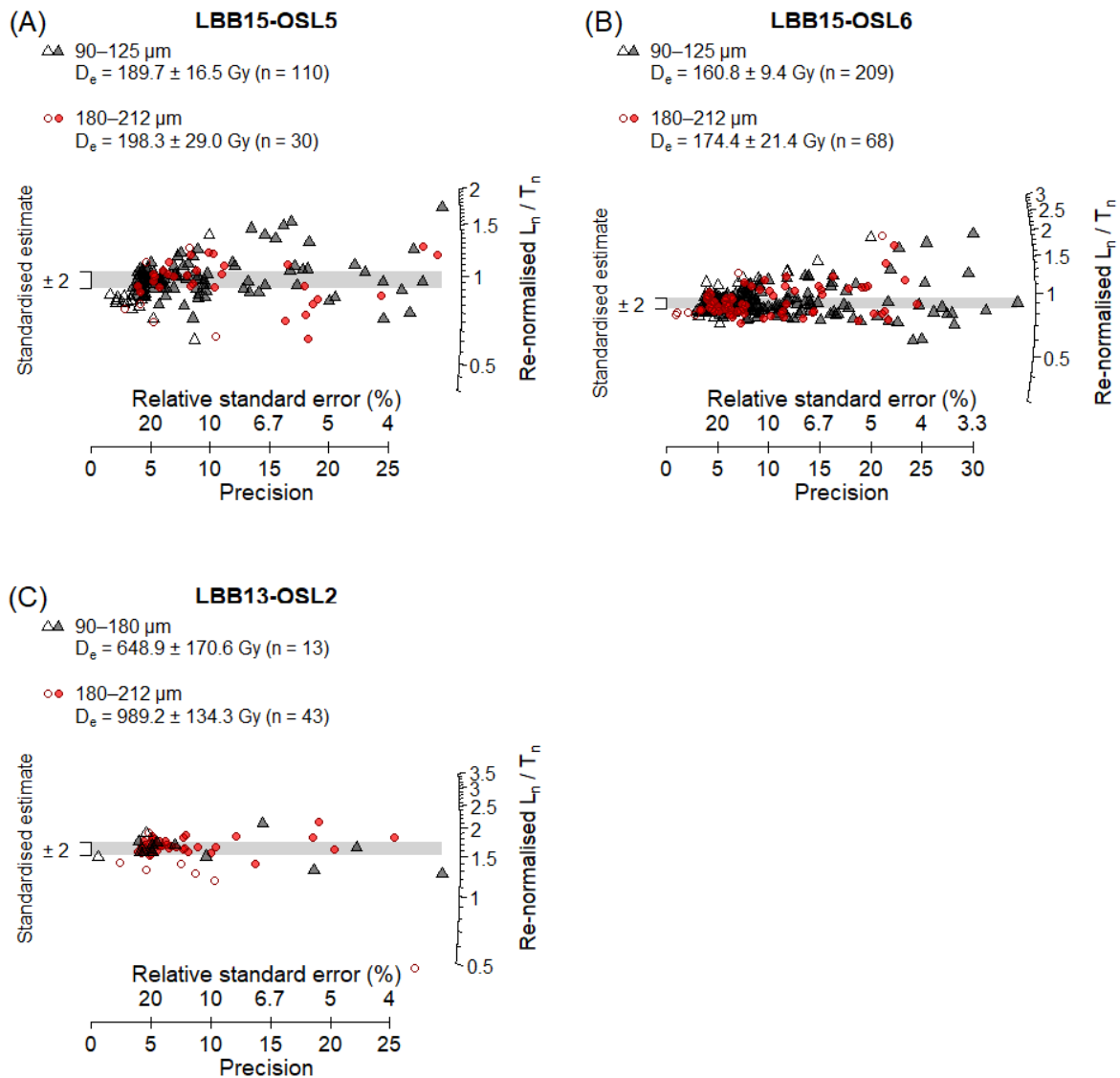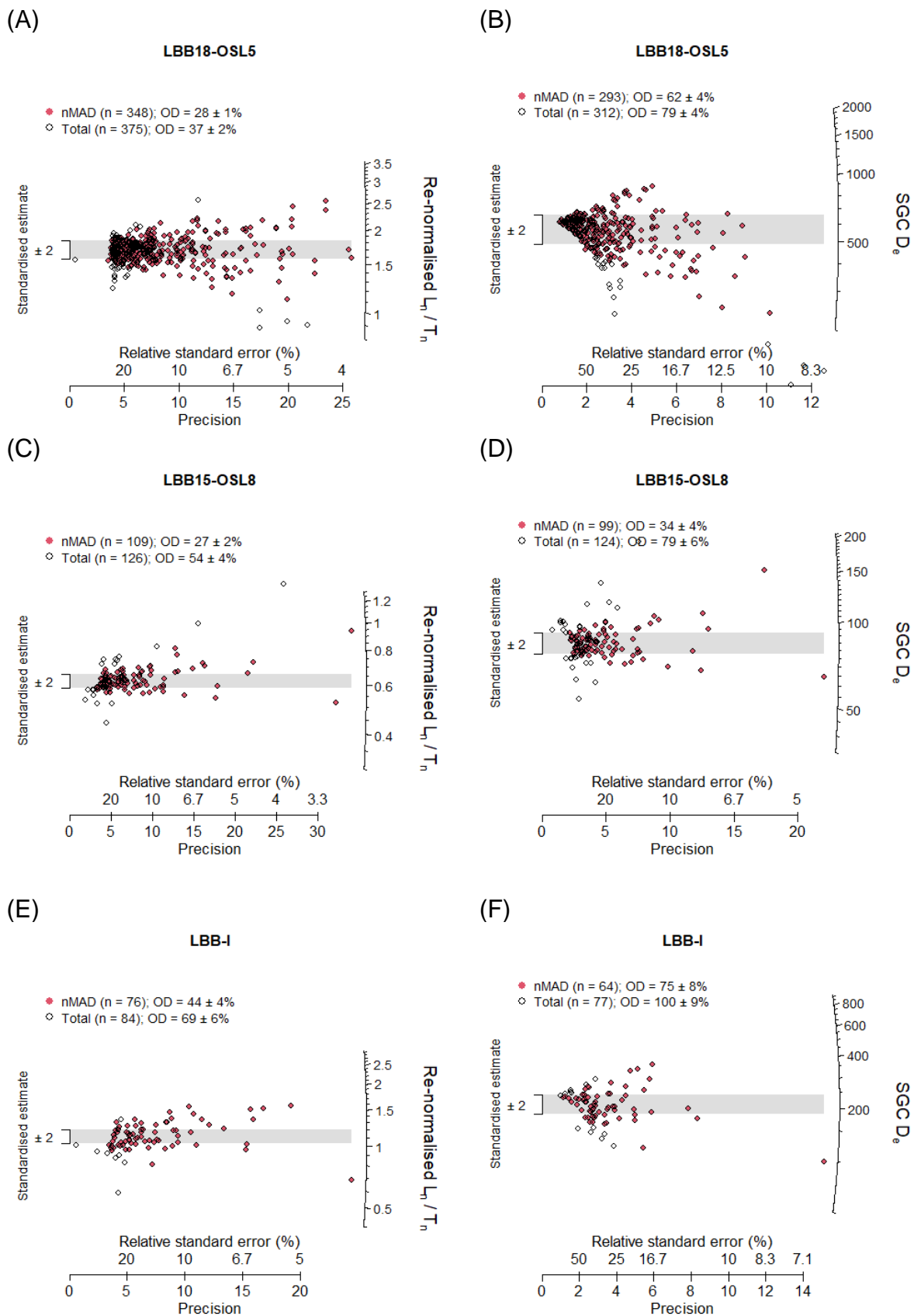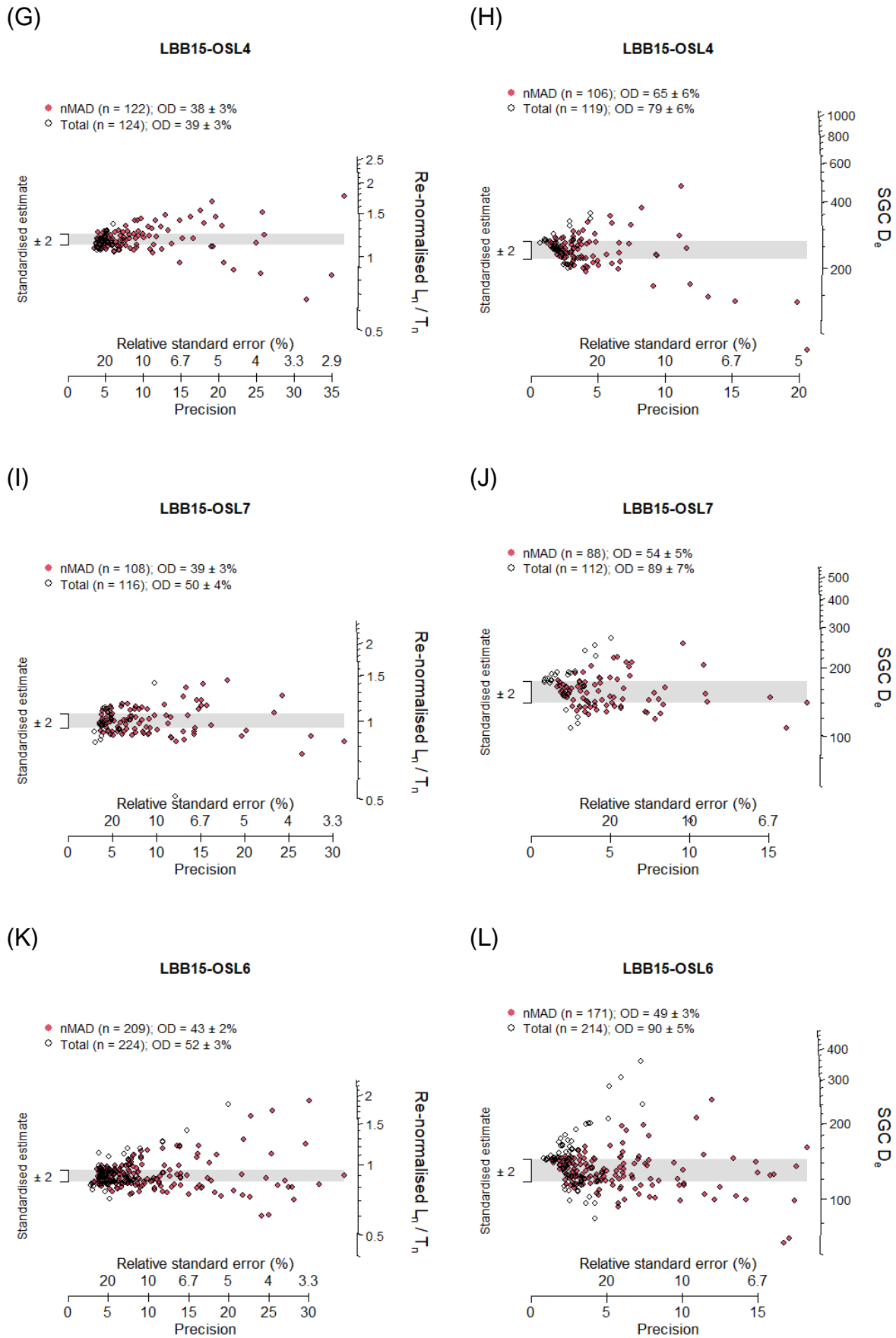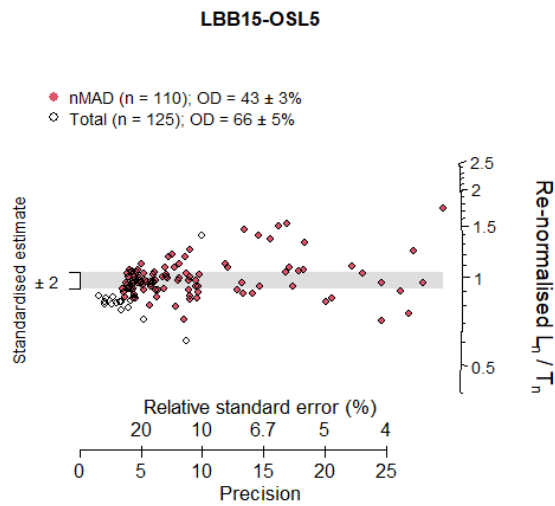

Figure S20: *Re-normalised L_n/T_n distributions for micro-aliquots (90–125 or 90–180 µm; black triangles) or single-grains (180–212 µm; red circles) of (A) LBB15-OSL5 (B) LBB15-OSL6 and (C) LBB13-OSL2. Weighted mean (CAM) D_e values are given in the legends (n: number of accepted micro-aliquots or single grains after outlier rejection with a nMAD cutoff of 2.0; outliers are shown as open symbols). Grey bands are centred on the weighted mean re-normalised L_n/T_n ratio for the micro-aliquot population.*
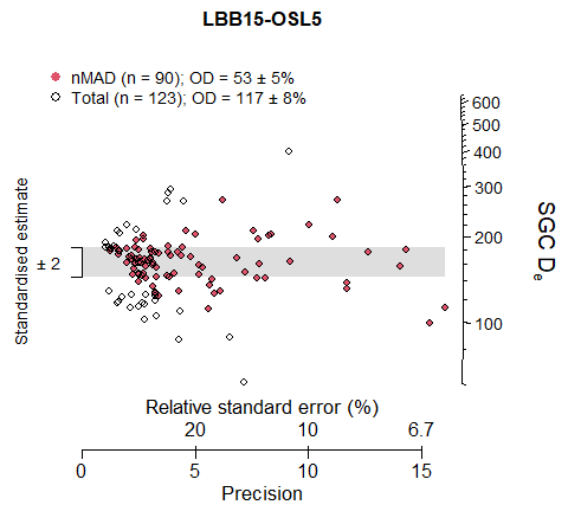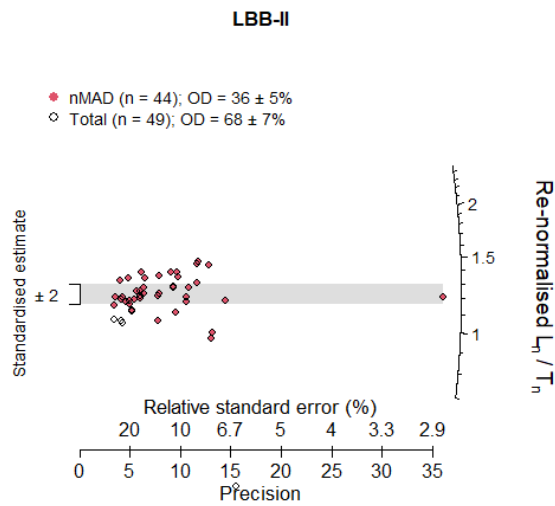
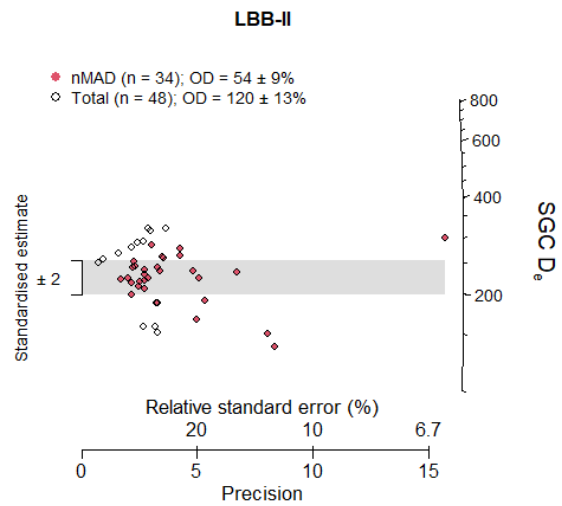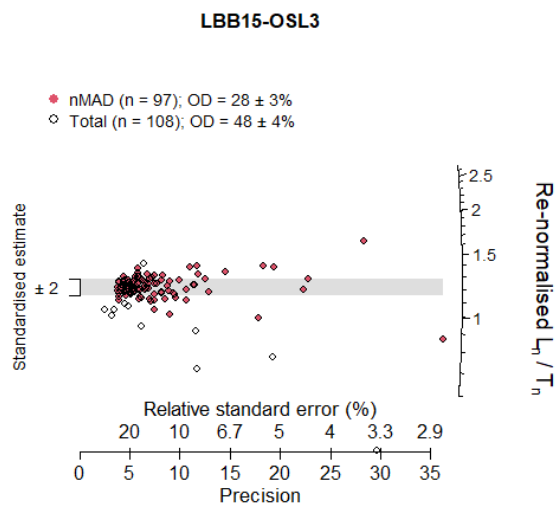## S4 Renormalised signal and dose distributions

(A)

(B)

(C)

(D)

(E)

(F)

(G)

(H)

(I)

(J)

(K)

(L)

(S)

LBB15-OSL2

- nMAD (n = 77); OD = 20 ± 2%
- Total (n = 82); OD = 27 ± 3%

(T)

LBB15-OSL2

- nMAD (n = 66); OD = 45 ± 6%
- Total (n = 76); OD = 68 ± 7%

(U)

LBB15-OSL1

- nMAD (n = 99); OD = 21 ± 2%
- Total (n = 113); OD = 37 ± 3%

(V)

LBB15-OSL1

- nMAD (n = 71); OD = 41 ± 6%
- Total (n = 86); OD = 77 ± 7%

(W)

LBB15-OSL0

- nMAD (n = 79); OD = 30 ± 3%
- Total (n = 92); OD = 73 ± 6%

(X)

LBB15-OSL0

- nMAD (n = 69); OD = 65 ± 8%
- Total (n = 84); OD = 131 ± 11%
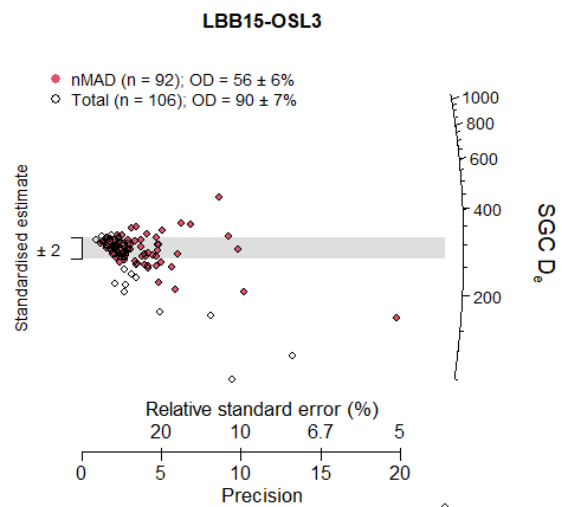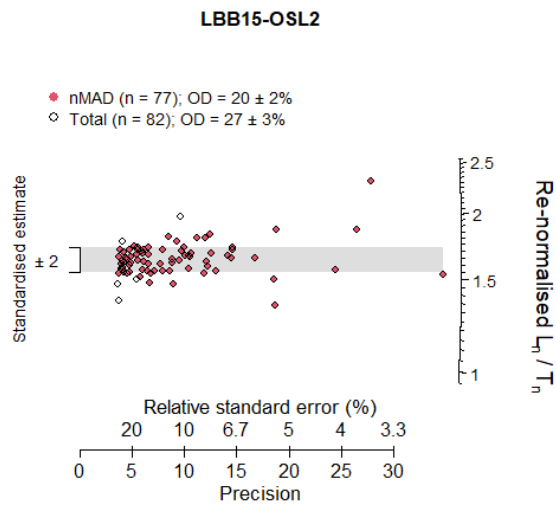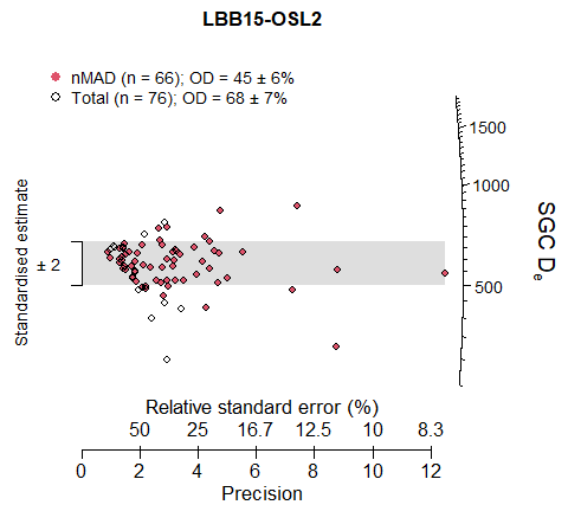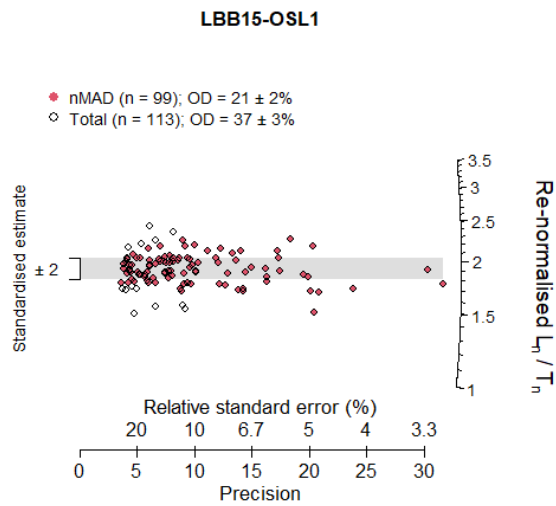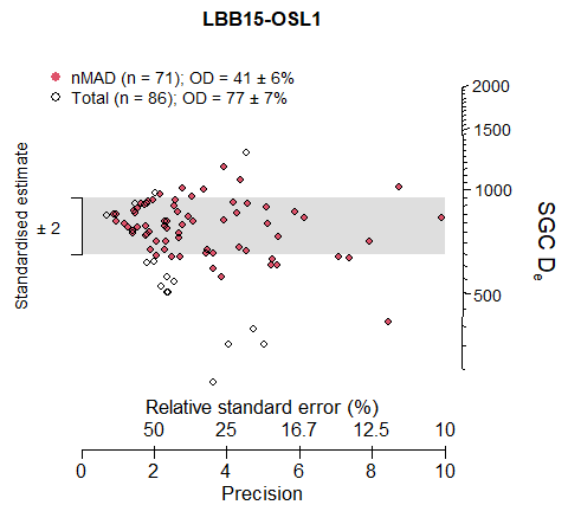
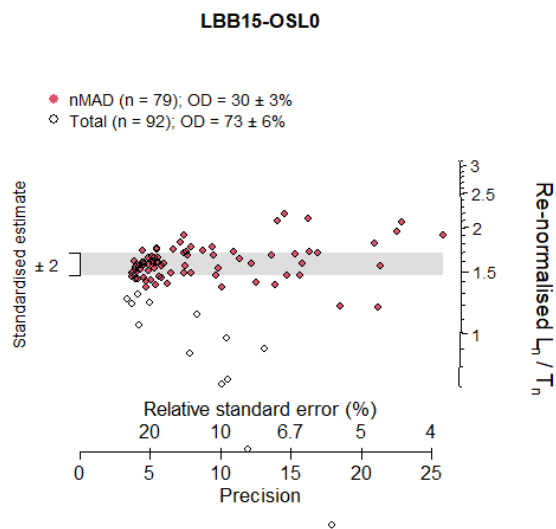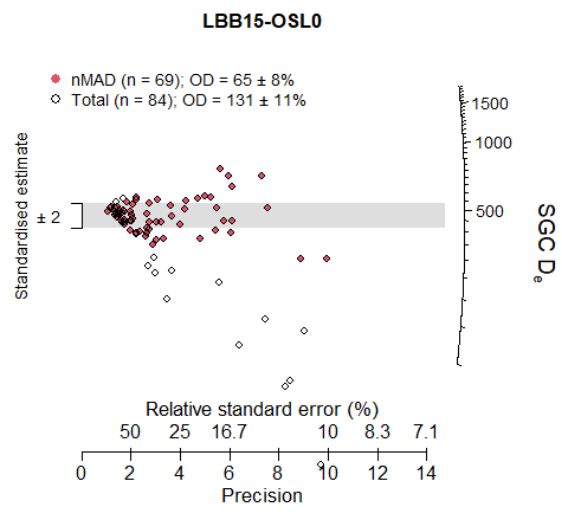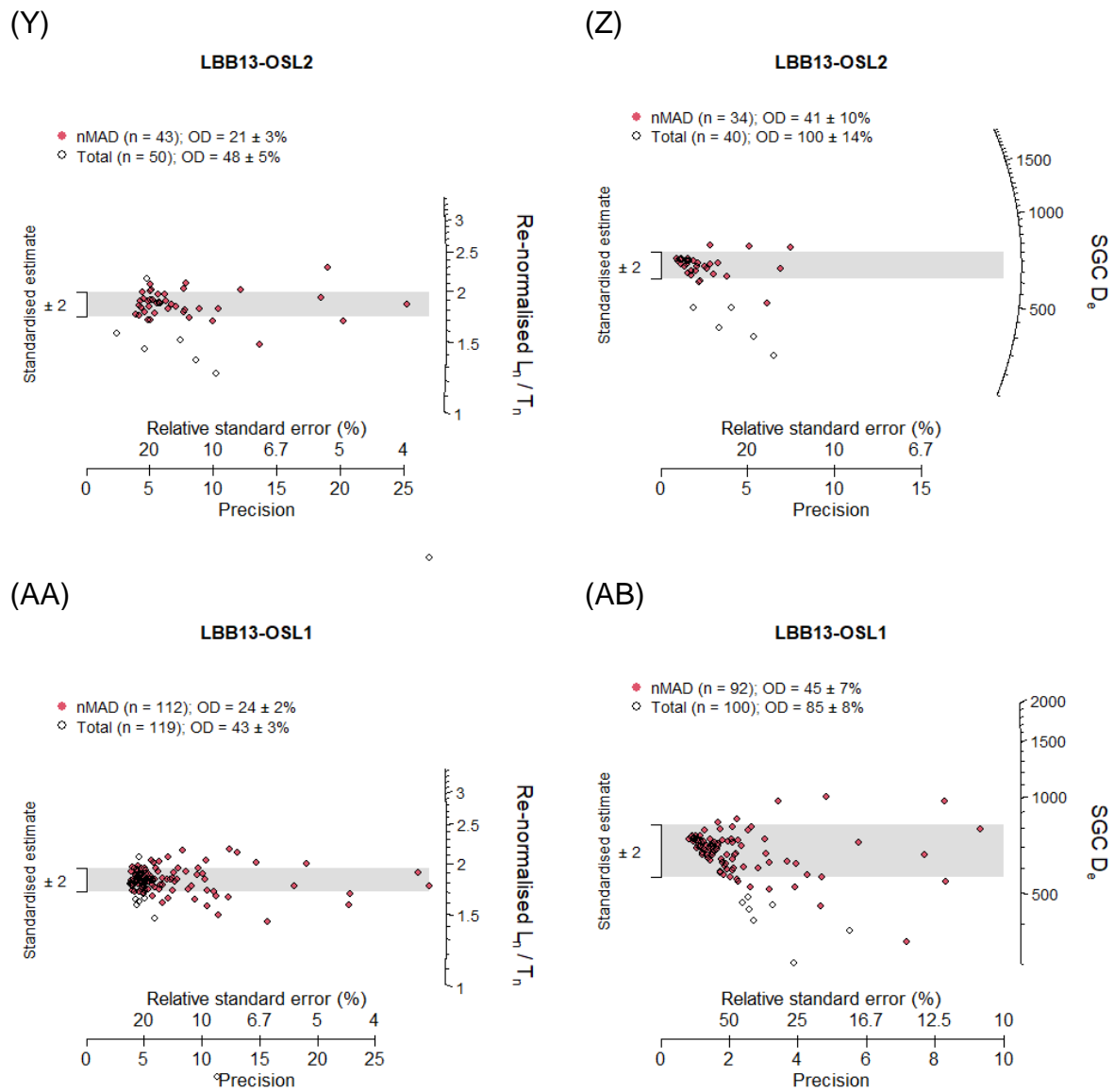***Figure S21:*** *Comparison of re-normalised L_n/T_n distributions and the resulting SGC D_e distributions. Each row represents one sample, given in stratigraphic order. Grey bands are centred on the nMAD CAM values of each distribution (cutoff re-normalised L_n/T_n: 2.0; cutoff D_e: 1.5). OD refers to the overdispersion value.*

(A)

(B)
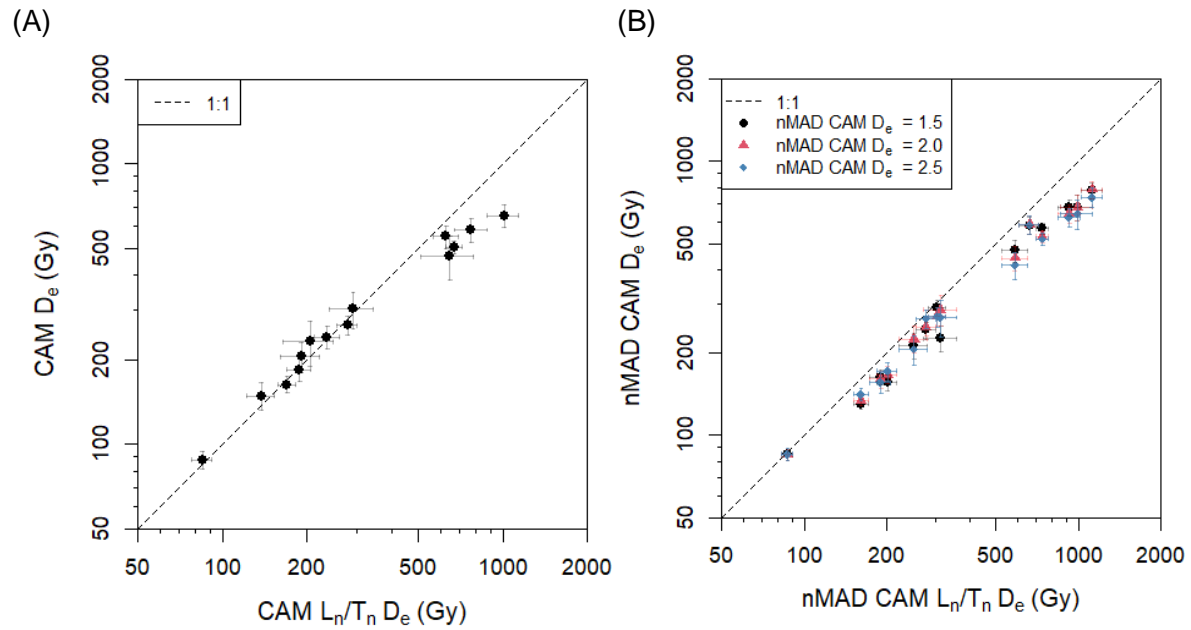
Figure S22: *Comparison of CAM D_e values (A) before and (B) after outlier removal obtained from each sample using either the L_nT_n method (x-axes), where the re-normalised L_n/T_n distribution is modelled, or the more conventional D_e method (y-axes), where the distribution of SGC D_e values is modelled; this distribution is obtained by projecting the individual L_n/T_n value of each micro-aliquot onto the SGC. In panel (B), three nMAD cutoff values for the SGC D_e distributions are displayed (a constant cutoff value of 2.0 was used for the re-normalised L_n/T_n distributions).*

Table S9: *Comparison of central age model (CAM) D_e estimation methods for all LBB samples. Number of micro-aliquots accepted during data analysis (#), overdispersion (OD) values and CAM D_e values are given for the distributions of re-normalised L_n/T_n values (SGC L_nT_n method) or those of D_e values from individual micro-aliquots (SGC D_e) before and after outlier rejection by the nMAD.*

Sample code	Measured micro-aliquots	SGC L_nT_n method						SGC D_e					
		Total			nMAD (cutoff = 2.0)			Total			nMAD (cutoff = 1.5)		
		#	OD (%)	CAM D_e (Gy)	#	OD (%)	CAM D_e (Gy)	#	OD (%)	CAM D_e (Gy)	#	OD (%)	CAM D_e (Gy)
LBB18-OSL5	4100	375	37 ± 2	668.5 ± 41.3	348	28 ± 1	738.0 ± 38.8	312	79 ± 4	504.3 ± 26.0	293	62 ± 4	566.8 ± 25.2
LBB15-OSL8	4400	126	54 ± 4	84.6 ± 6.7	109	27 ± 2	86.8 ± 4.1	124	79 ± 6	88.0 ± 6.7	99	34 ± 4	84.7 ± 3.6
LBB-I	3800	84	69 ± 6	190.9 ± 29.6	76	44 ± 4	251.3 ± 29.4	77	100 ± 9	205.2 ± 25.0	64	75 ± 8	212.1 ± 21.9
LBB15-OSL4	2900	124	39 ± 3	278.7 ± 23.6	122	38 ± 3	278.2 ± 23.1	119	79 ± 6	265.7 ± 21.2	106	65 ± 6	241.5 ± 17.3
LBB15-OSL7	3000	116	50 ± 4	187.8 ± 18.1	108	39 ± 3	200.9 ± 16.4	112	89 ± 7	184.0 ± 16.6	88	54 ± 5	155.8 ± 10.1
LBB15-OSL6	1500	224	52 ± 3	169.8 ± 11.8	209	43 ± 2	160.8 ± 9.4	214	90 ± 5	163.2 ± 10.7	171	49 ± 3	129.8 ± 5.6
LBB15-OSL5	3200	125	66 ± 5	137.2 ± 15.2	110	43 ± 3	189.7 ± 16.5	123	117 ± 8	148.8 ± 16.4	90	53 ± 5	162.8 ± 10.3
LBB-II	2600	49	68 ± 7	205.6 ± 42.0	44	36 ± 5	313.9 ± 43.3	48	120 ± 13	232.0 ± 42.3	34	54 ± 9	225.0 ± 24.3
LBB15-OSL3	3800	108	48 ± 4	235.9 ± 24.6	97	28 ± 3	305.0 ± 22.7	106	90 ± 7	241.3 ± 23.0	92	56 ± 6	291.0 ± 20.3
LBB15-OSL2	1800	82	27 ± 3	627.1 ± 62.5	77	20 ± 2	661.2 ± 54.7	76	68 ± 7	549.1 ± 50.6	66	45 ± 6	581.7 ± 42.8
LBB15-OSL1	1000	113	37 ± 3	1007.2 ± 128.4	99	21 ± 2	1117.2 ± 98.3	86	77 ± 7	653.4 ± 61.8	71	41 ± 6	781.7 ± 50.9
LBB15-OSL0	500	92	73 ± 6	291.9 ± 51.6	79	30 ± 3	585.6 ± 63.3	84	131 ± 11	303.4 ± 45.8	69	65 ± 8	471.8 ± 43.8
LBB13-OSL2	4100	50	48 ± 5	645.9 ± 138.7	43	21 ± 3	989.2 ± 134.3	40	100 ± 14	467.5 ± 83.2	34	41 ± 10	678.4 ± 73.1
LBB13-OSL1	7300	119	43 ± 3	770.4 ± 102.7	112	24 ± 2	924.8 ± 85.1	100	85 ± 8	580.8 ± 59.1	92	45 ± 7	676.1 ± 48.2

Table S10: Comparison of minimum age model (MAM) D_e estimation methods using the same datasets before and after outlier rejection as in Table S9. D_e values are given for the distributions of re-normalised L_n/T_n values (SGC L_nT_n method) or those of D_e values from individual micro-aliquots (SGC D_e). σ_b refers to the expected overdispersion of a well-bleached population. The maximum log likelihood score (llik) is an estimate of the model's goodness-of-fit.

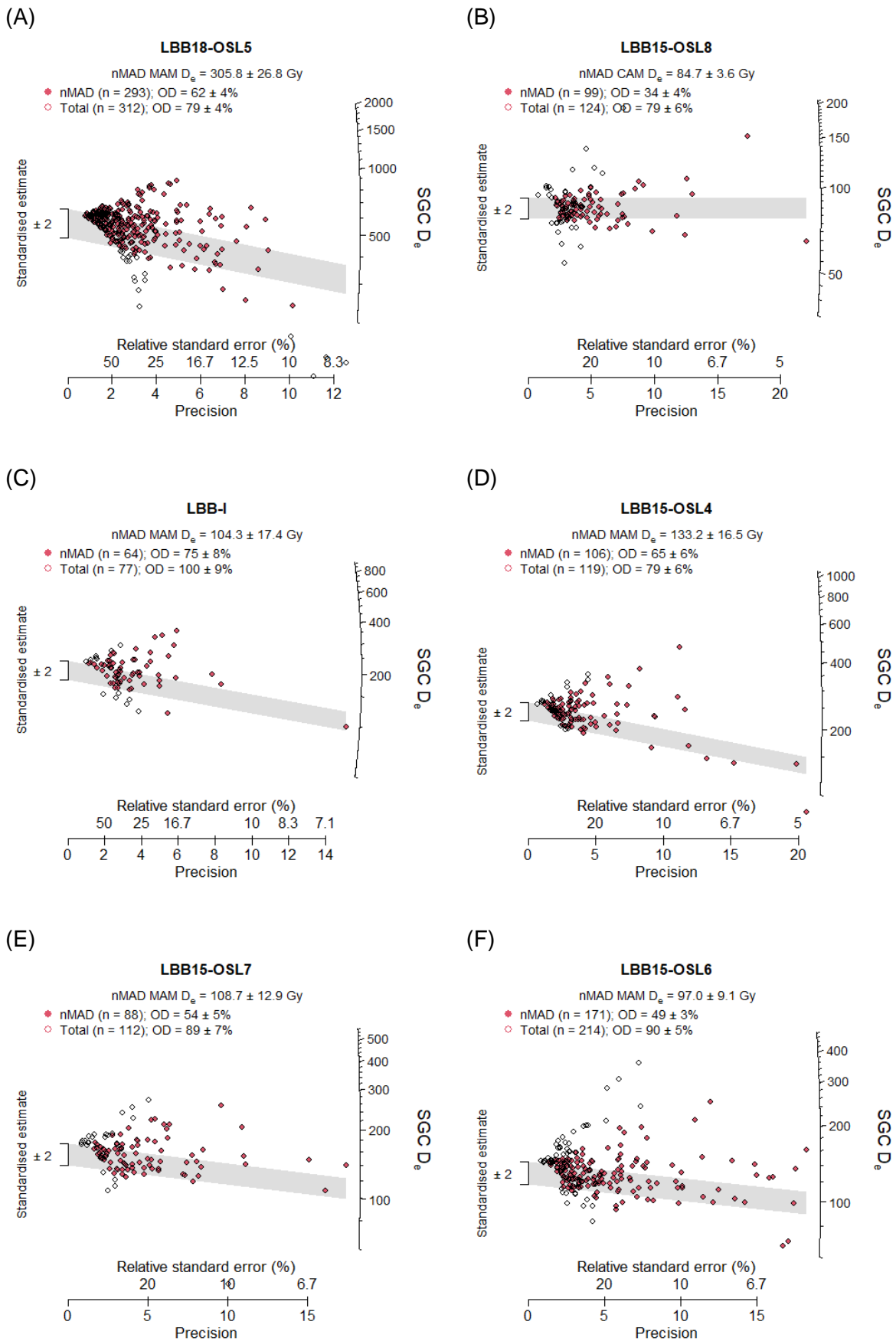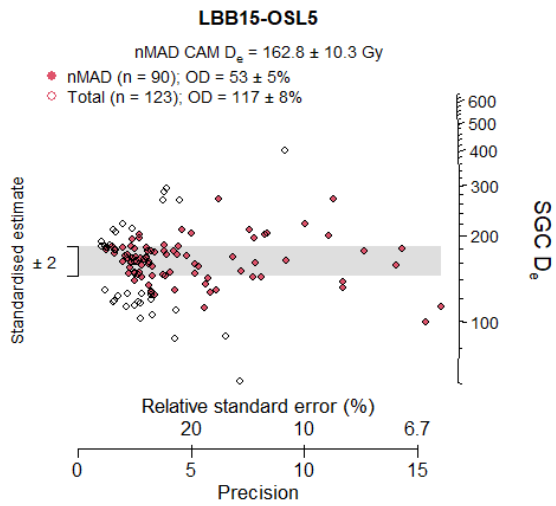| Sample code	SGC L_nT_n method								SGC D_e			
	Total				nMAD (cutoff = 2.0)				Total		nMAD (cutoff = 1.5)	
	$\sigma_b = 0.15$		$\sigma_b = 0.25$		$\sigma_b = 0.15$		$\sigma_b = 0.25$		$\sigma_b = 0.35$		$\sigma_b = 0.35$	
	llik	MAM D_e (Gy)	llik	MAM D_e (Gy)	llik	MAM D_e (Gy)	llik	MAM D_e (Gy)	llik	MAM D_e (Gy)	llik	MAM D_e (Gy)
LBB18-OSL5	-244	225.0 ± 15.5	-216	321.1±32.3	-109	337.1±25.9	-101	582.4±88.2	-441	190.5±15.2	-339	305.8±26.8
LBB15-OSL8	-146	37.3 ± 4.2	-130	43.5±5.4	-30	62.5±5.3	-37	80.2±7.3	-170	44.3±8.2	-60	80.8±5.6
LBB-I	-144	27.4 ± 5.9	-128	44.7±9.1	-57	95.4±13.1	-55	118.4±19.3	-122	56.3±10.0	-79	104.3±17.4
LBB15-OSL4	-71	118.2 ± 11.8	-70	148.8±20.1	-66	121.1±12.0	-65	153.4±20.7	-151	122.0±16.0	-116	133.2±16.5
LBB15-OSL7	-118	61.0 ± 6.6	-103	80.4±10.6	-59	99.6±10.4	-60	116.3±15.2	-166	66.7±9.8	-79	108.7±12.9
LBB15-OSL6	-186	64.2 ± 5.6	-181	79.0±10.2	-129	76.2±6.9	-128	91.2±9.9	-289	79.7±11.3	-146	97.0±9.1
LBB15-OSL5	-169	26.4 ± 3.5	-161	36.5±5.4	-80	77.3±8.1	-75	98.6±13.9	-219	27.4±4.3	-85	114.0±15.1
LBB-II	-79	10.9 ± 1.6	-75	20.4±5.2	-24	132.4±21.4	-23	194.2±45.9	-96	18.4±5.0	-33	159.1±32.6
LBB15-OSL3	-120	54.4 ± 6.9	-102	96.4±13.7	-30	175.4±19.8	-36	272.5±37.2	-169	65.7±9.7	-94	185.3±24.1
LBB15-OSL2	-30	384.1 ± 65.5	-36	564.5±89.4	-7	521.5±89.6	-17	618.8±76.3	-98	302.3±50.7	-62	490.1±70.1
LBB15-OSL1	-71	336.9 ± 49.3	-64	542.9±143.0	-7	717.8±118.6	-22	1046.1±138.8	-122	268.4±42.9	-62	692.5±81.9
LBB15-OSL0	-149	14.4 ± 1.9	-142	23.2±3.9	-29	289.3±44.0	-32	464.2±99.5	-170	19.4±3.6	-80	264.5±41.2
LBB13-OSL2	-55	88.8 ± 17.0	-48	193.3±54.1	-8	740.5±174.3	-12	910.1±179.5	-69	87.9±21.6	-34	608.8±92.6
LBB13-OSL1	-165	188.0 ± 31.3	-102	385.7±77.0	-22	533.0±84.6	-33	845.5±122.1	-176	188.9±32.1	-96	567.8±77.0
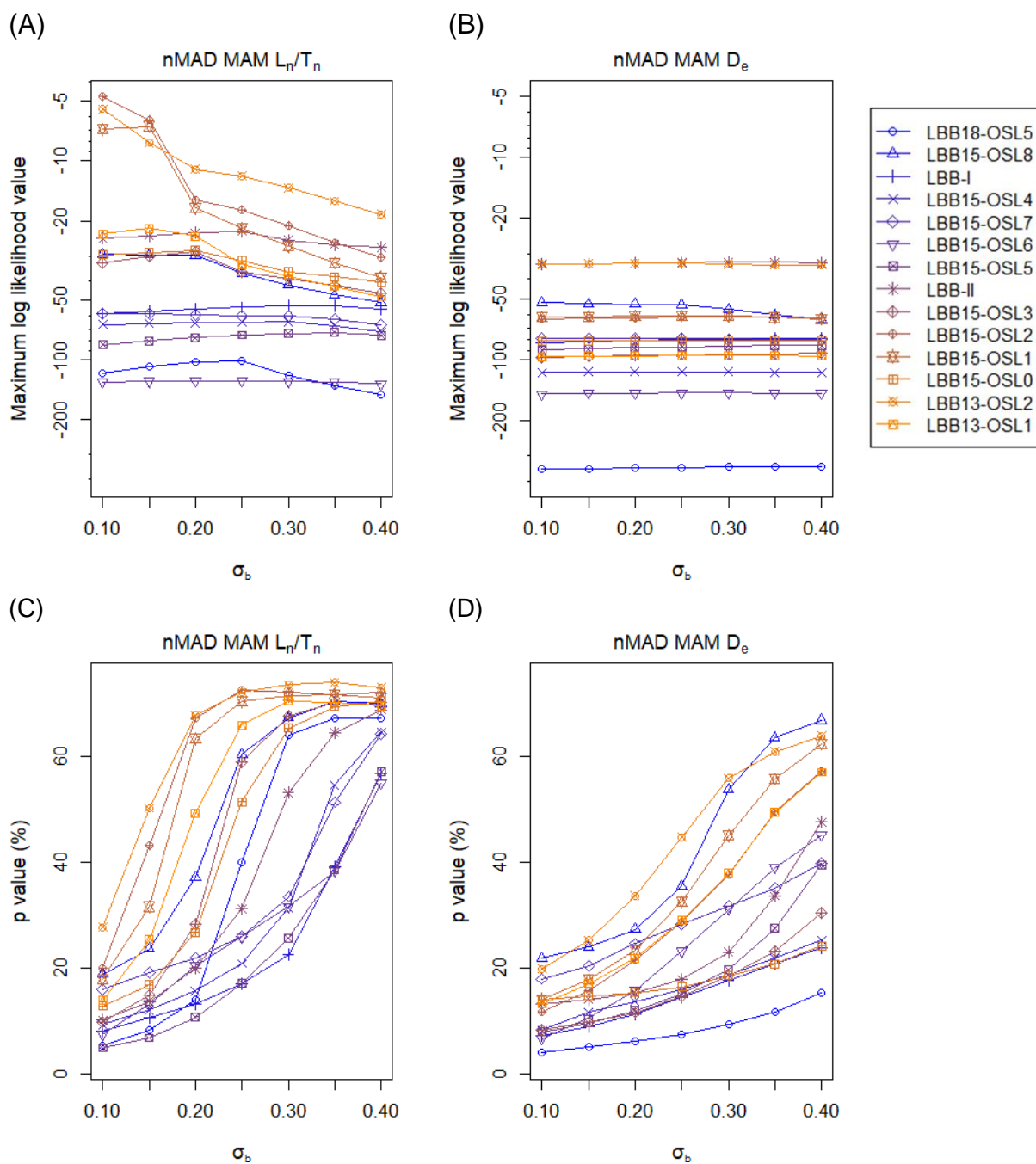
Figure S23: *Statistical output parameters of the minimum age model after outlier rejection (nMAD MAM) using (A, C) the L_n/T_n distributions with a cutoff value of 2.0 and (B, D) the D_e distributions with a cutoff value of 1.5 of all samples (shown in the legend in stratigraphic order). (A, B) show the maximum log likelihood value, which is a measure of goodness-of-fit, and (C, D) show the proportion of fully bleached micro-aliquots (p).*
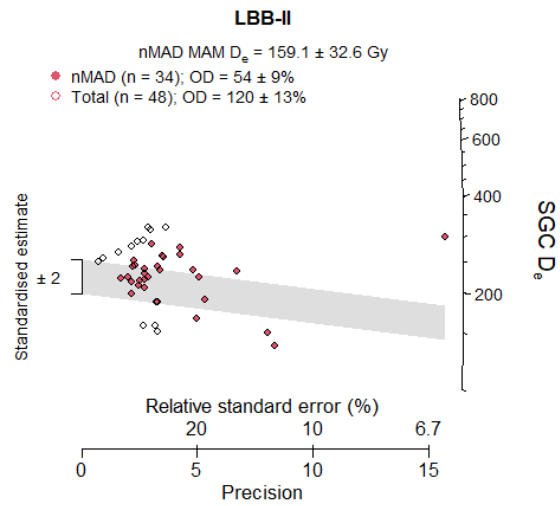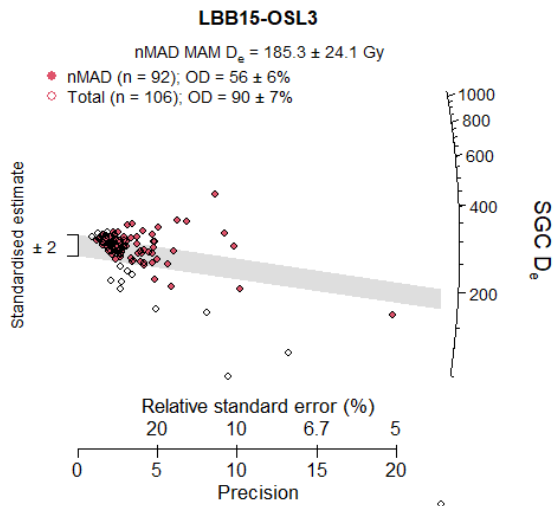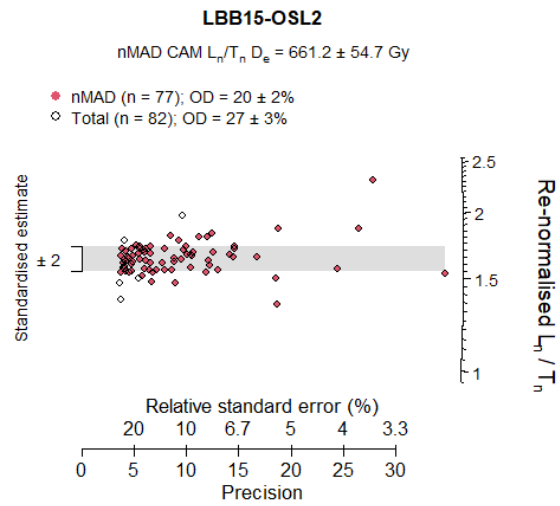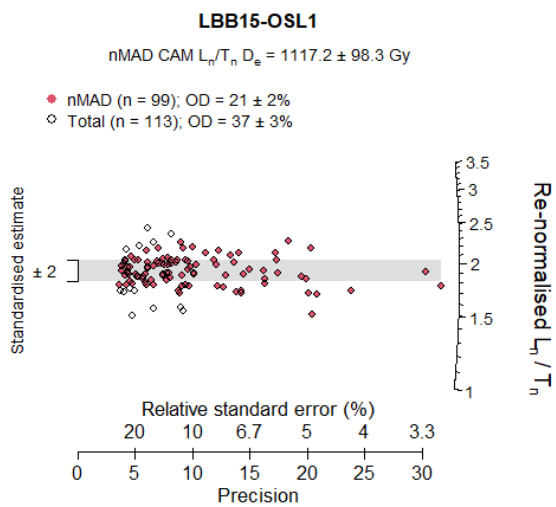
S4.1   Distributions of selected age models

(A)

(B)

(C)

(D)

(E)

(F)

(G)

LBB15-OSL5

nMAD CAM D_e = 162.8 ± 10.3 Gy

nMAD (n = 90); OD = 53 ± 5%
Total (n = 123); OD = 117 ± 8%

(H)

LBB-II

nMAD MAM D_e = 159.1 ± 32.6 Gy

nMAD (n = 34); OD = 54 ± 9%
Total (n = 48); OD = 120 ± 13%

(I)

LBB15-OSL3

nMAD MAM D_e = 185.3 ± 24.1 Gy

nMAD (n = 92); OD = 56 ± 6%
Total (n = 106); OD = 90 ± 7%

(J)

LBB15-OSL2

nMAD CAM L_n/T_n D_e = 661.2 ± 54.7 Gy

nMAD (n = 77); OD = 20 ± 2%
Total (n = 82); OD = 27 ± 3%

(K)

LBB15-OSL1

nMAD CAM L_n/T_n D_e = 1117.2 ± 98.3 Gy

nMAD (n = 99); OD = 21 ± 2%
Total (n = 113); OD = 37 ± 3%

(L)

LBB15-OSL0

nMAD CAM L_n/T_n D_e = 585.6 ± 63.3 Gy

nMAD (n = 79); OD = 30 ± 3%
Total (n = 92); OD = 73 ± 6%

61

(M)

LBB13-OSL2

nMAD CAM L_n/T_n D_e = 989.2 ± 134.3 Gy

• nMAD (n = 43); OD = 21 ± 3%
○ Total (n = 50); OD = 48 ± 5%

(N)

LBB13-OSL1

nMAD CAM L_n/T_n D_e = 924.8 ± 85.0 Gy
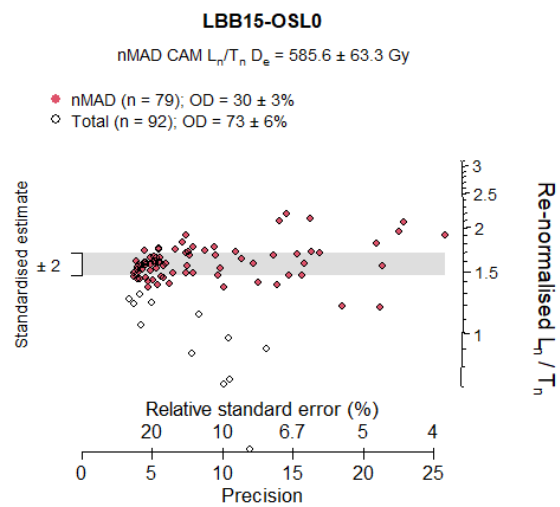
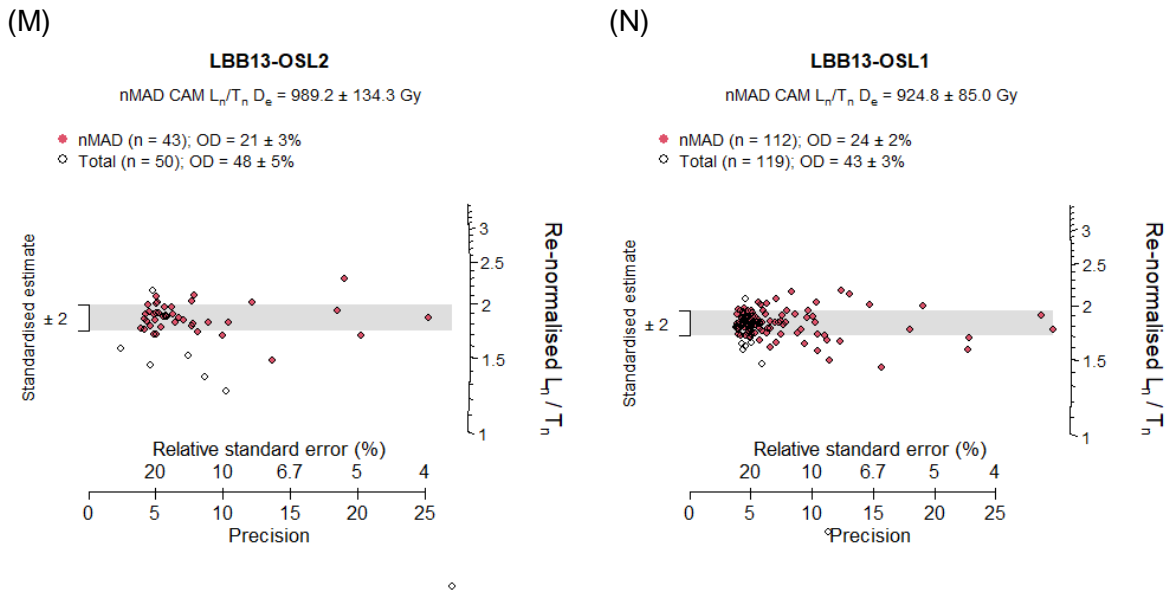• nMAD (n = 112); OD = 24 ± 2%
○ Total (n = 119); OD = 43 ± 3%

Figure S24: Distributions of micro-aliquot (A−I) SGC D_e or (J−N) re-normalised L_n/T_n for all samples in stratigraphic order with details of the age models used for dating. Two age models were used: (B, G, J–N) a central age model (CAM), and (A,C–F, H, I) a minimum age model (MAM) using σ_b = 0.35. Outliers were removed prior to either age models using nMAD cutoff values of (A−I) 1.5 or (J−N) 2.0. The radial plots are centred on the nMAD CAM and the grey bands are centred on the modelled values (nMAD CAM or nMAD MAM). OD refers to the overdispersion value.
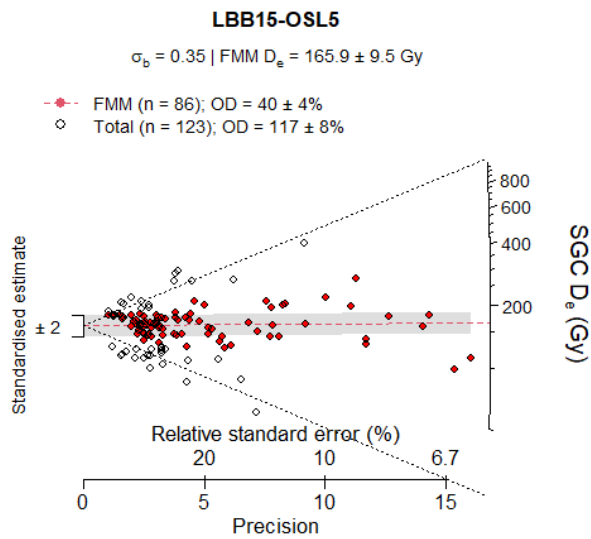
S4.2 Alternative age models

Figure S25: *Radial plot of an alternative age model for sample LBB15-OSL5, centred on the weighted mean (nMAD CAM) of the entire population. A finite mixture model (FMM) was applied to the SGC D_e. Lines indicate the FMM components; the population corresponding to the FMM component with the highest micro-aliquot proportion is shown in red and was used to determine the FMM D_e. The grey band is centred on the latter value. OD refers to the overdispersion value and σ_b to the optimal overdispersion value determined for the FMM*

Table S11: *Alternative age model for sample LBB15-OSL5. The maximum log likelihood score (llik) is an estimate of the model's goodness-of-fit. The FMM component with the highest proportion of micro-aliquots is shown in bold type.*

Model	σ_b	llik	Component #	Nr. Of micro-aliquots	D_e (Gy)	Fading corrected age[a] (ka)
			1	22 / 123	23.7 ±3.0	3.5 ±0.7
FMM SGC D_e	0.35	-196.3	2	86 / 123	165.9 ±9.5	**41.8 ± 3.5**
			3	15 / 123	1053.7 ±167.0	284.5 ±54.5

[a] Ages are obtained by subtracting a residual dose (10.4 ± 0.7 Gy) from the D_e, dividing by the corresponding dose rate and correcting for anomalous fading.
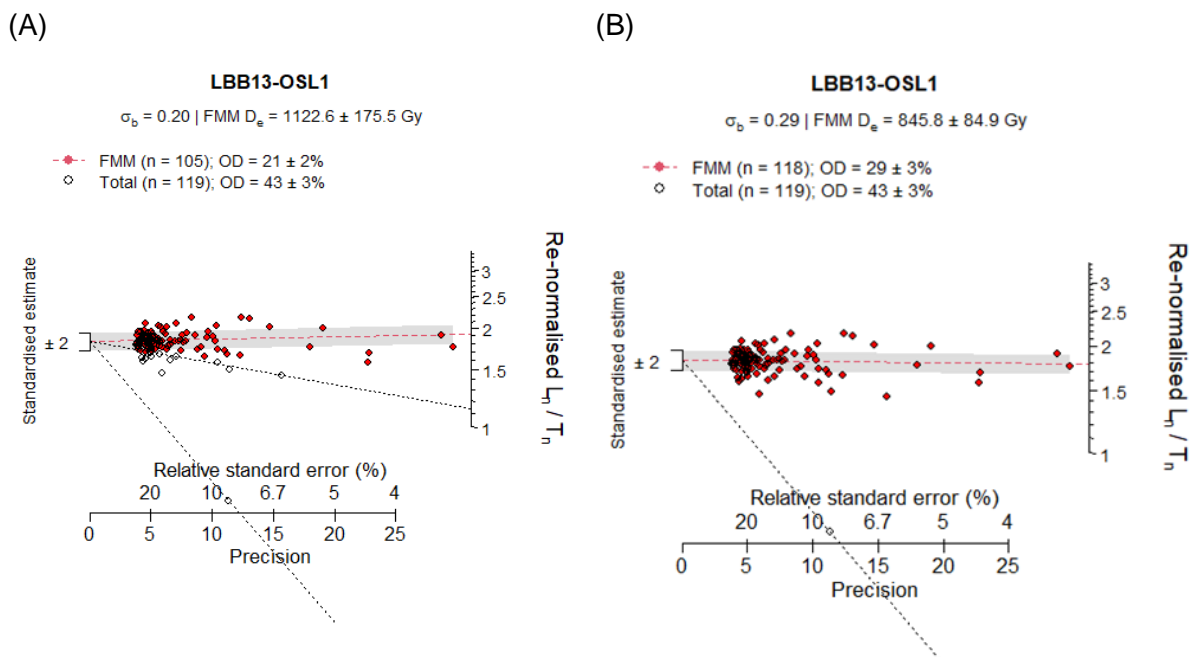
(A)

(B)

Figure S26: *Radial plots of alternative age models for sample LBB13-OSL1, centred on the weighted mean (nMAD CAM) of the entire populations. Finite mixture models (FMM) were applied to the re-normalised L_n/T_n ratios. Lines indicate the FMM components; the populations corresponding to the FMM components with the highest micro-aliquot proportions are shown in red and were used to determine the FMM D_e. The grey bands are centred on the latter value. OD refers to the overdispersion value and σ_b to the optimal overdispersion value determined for the FMM.*

Table S12: *Alternative age models for sample LBB13-OSL1. The maximum log likelihood score (llik) is an estimate of the model's goodness-of-fit. The FMM component with the highest proportion of micro-aliquots is shown in bold type.*

Model	σ_b	llik	Component #	Nr. Of micro-aliquots	D_e (Gy)	Fading corrected age[a] (ka)
FMM re-normalised L_n/T_n	0.20	-46.9	1	1 / 119	6.3 ±1.7	Modern
			2	13 / 119	259.1 ±92.5	50.8 ±19.0
			3	105 / 119	1122.6 ±175.5	**229.8 ±39.7**
	0.29	-47.3	1	1 / 119	6.26 ±3.2	Modern
			2	118 / 119	845.8 ±84.9	**172.3 ± 24.5**

[a] Ages are obtained by subtracting a residual dose (10.4 ± 0.7 Gy) from the D_e, dividing by the corresponding dose rate and correcting for anomalous fading.